Root for rain

Towards understanding land-use change impacts on the water cycle

Wang-Erlandsson, Lan

DOI
10.4233/uuid:748b66b7-0f95-4978-8ce8-2ebf4bd5ee0b

Publication date
2017

Document Version
Final published version

Citation (APA)
Wang-Erlandsson, L. (2017). *Root for rain: Towards understanding land-use change impacts on the water cycle*. [Dissertation (TU Delft), Delft University of Technology]. https://doi.org/10.4233/uuid:748b66b7-0f95-4978-8ce8-2ebf4bd5ee0b

ROOT FOR RAIN

TOWARDS UNDERSTANDING LAND-USE CHANGE IMPACTS ON THE WATER CYCLE

ROOT FOR RAIN

TOWARDS UNDERSTANDING LAND-USE CHANGE IMPACTS ON THE WATER CYCLE

Proefschrift

ter verkrijging van de graad van doctor
aan de Technische Universiteit Delft,
op gezag van de Rector Magnificus prof. ir. K.C.A.M. Luyben,
voorzitter van het College voor Promoties,
in het openbaar te verdedigen op donderdag 28 september 2017 om 12:30 uur

door

Lan WANG-ERLANDSSON

Master of Science in Engineering,
KTH Royal Institute of Technology, Stockholm, Zweden;
geboren te Guiyang, China.

This dissertation has been approved by the

promotor: Prof. dr. ir. H. H. G. Savenije
promotor: Prof. dr. J. Rockström
copromotor: Dr. L. J. Gordon

Composition of the doctoral committee:

Rector Magnificus,	chairman
Prof. dr. ir. H. H. G Savenije,	Technische Universiteit Delft, promotor
Dr. L. J. Gordon,	Stockholms Universitet, Zweden, copromotor
Prof. dr. J. Rockström,	Stockholms Universitet, Zweden, promotor
Independent members:	
Prof. dr. W. G. M. Bastiaanssen,	Technische Universiteit Delft
Prof. dr. N. C. van de Giesen,	Technische Universiteit Delft
Prof. dr. M. Bierkens,	Universiteit Utrecht
Dr. A. M. J. Coenders-Gerrits,	Technische Universiteit Delft

This research was co-funded by the Swedish Research Council (Vetenskapsrådet) and the Swedish Research Council Formas (Forskningsrådet Formas).

Keywords: water resources, moisture recycling, land-use change, land-atmosphere interactions

Printed by: Ipskamp Drukkers, Enschede, Netherlands

Front & Back: Aquarelle by L. Wang-Erlandsson

An electronic version of this dissertation is available at
http://repository.tudelft.nl/.

A small square pond an uncovered mirror
where sunlight and clouds linger and leave
I asked how it stays so clear
it said spring water keeps flowing in

Zhu Xi (1130-1200)
'Reflections While Reading'

ACKNOWLEDGMENT

First and foremost, I would like to thank my three brilliant supervisors. Hubert, you are the most empowering supervisor imaginable. Your enthusiasm and passion for science is contagious. You taught me to not be afraid of thinking differently, to dare to question everything: high-profile publications, my own analysis, your ideas. Not to mention how rare it is for a professor of your rank to always keep your office door open for your students, and to always make every effort to introduce us youngsters to established researchers in the field. Line, you are a singularly wonderful advisor, mentor, and friend. No matter how complex or messy a problem is, you have taught me to structure it, turn it around, and find the most intriguing angle. Thank you for challenging me to polish a text until it blinds and dazzles, for generously sharing your experience in academia, and for the nerve to reach for the stars. Johan, you are my superhero scientist, science communicator, and world saver. Needless to say, your influence extends well beyond supervision. Thank you for instilling much needed hope about the possibility of a good future, and showing how bold, transformative, and world changing science looks.

Ruud and Pat, this PhD journey would never have been this enriching without you. Ruud, I am in awe of your Sherlock's eye for detail and your unapologetic scientific integrity. Pat, I deeply admire your extraordinary ability to think out of the box and your courage to break disciplinary barriers. We are each different, but have been bundled by our friendship and common research attitude in a way that most PhD students can only covet. I hope we will also accompany each other on our continued academic voyage.

I would like to express my gratitude to all colleagues and friends at TU Delft and SU. A special thanks to Tanja, for your unfaltering friendship; Miriam, for being a role model; Jianzhi, Ingo, Steve, for all fun and stimulating talks that comes with sharing an office; Daniele, for letting a rookie like me supervise you; Thérése, for your patience dealing with my plentiful reimbursement application mistakes; Cecilia, Emina, Luz, Lydia, Betty, Tanja, Susan for all your "behind-the-scenes" support; the Planetary Boundaries group, for "adopting" me; Örjan, for the invaluable mentorship that will help me navigate the academic maze for years to come; co-authors and referees, for shaping the papers that make up this thesis; and doctoral committee members, for your precious commitment.

Joakim, you rock. Thank you for coming along with me to the Netherlands, for helping me solve seemingly intractable Java heap space problems, and for enduring all those early Saturday morning pyjamas ramblings about mundane and not-so-mundane research matters that I may or may not have dreamed up during the night. Ma and Ba, thank you for always supporting me. Last but not least, Eira, thank you for forcefully dragging me away from my computer screen to watch egrets fishing, splash in puddles, and have hilarious fun, blowing the seeds off dandelion globes.

"There is probably purpose and meaning in our journey, but it is the pathway there, which is worth our while." (From On the Move by Karin Boye, translation by Jenny Nunn)

So, thank you all for making this PhD journey so thoroughly worthwhile.

SUMMARY

We live today on a human-dominated planet under unprecedented pressure on both land and water. The water cycle is intrinsically linked to vegetation and land use, and anticipating the consequences of simultaneous changes in land and water systems requires a thorough understanding of their interactions. This thesis aims to advance our knowledge of *how land-use change influences the water cycle*, i.e., focussing on the role of land-use in mediating water's journey from land evaporation, to atmospheric moisture, and to precipitation on land.

This thesis first presents the development (Chapter 2) and evaluation (Chapter 3) of the process-based water balance model STEAM (Simple Terrestrial Evaporation to Atmosphere Model). STEAM simulates five different evaporation fluxes, based on land-use representation with only a limited number of parameters. Comparison with independent data shows that STEAM produces realistic evaporative partitioning and hydrological fluxes over different locations, seasons and land-use types.

Chapter 4 investigates the temporal characteristics of partitioned evaporation, and shows that terrestrial residence timescale of transpiration (days to months) is substantially longer than that of interception (hours). The vegetation's ability to transpire by retaining and accessing soil moisture at great depth is critical for dry season evaporation, and the substantial differences in temporal characteristics between evaporation fluxes can create contrasting moisture recycling patterns.

In response to the importance of root zone storage capacity for transpiration and moisture recycling simulation, Chapter 5 sets out to present an 'earth observation-based' method for estimating this critical parameter in land surface modelling. By assuming that vegetation does not root deeper than necessary to bridge critical dry periods, satellite-based evaporation were used to derive root zone storage capacity. The new estimate improved evaporation simulation overall, and in particular during the least evaporating months in sub-humid to humid regions with moderate to high seasonality. The results suggest that several forest types are able to create a large storage to buffer for severe droughts, in contrast to e.g., grasslands and croplands.

Based on the new insights, Chapter 6 analyses the effects of land-use change on river flows. In some of the world's largest basins, precipitation was found to be more influenced by extra-basin, than within-basin, land-use change. In fact, in several non-transboundary basins, river flows were considerably influenced by land-use changes in foreign countries, suggesting new transboundary water relationships in international politics.

This thesis addressed different domains in the water cycle to improve our understanding of land-water interactions. Every water flux and stock requires our examination, whether they flow visibly in rivers, travel invisibly in the air, or hide deep in soil and roots. Because of the terrestrial water cycle's interaction with land, and therefore human activities, we are in an extraordinary position to shape its path and pace.

SAMENVATTING

We leven op een planeet die wordt gedomineerd door mensen en waar zowel water als land onder ongekende druk staan. De watercyclus kan niet losgekoppeld worden van vegetatie en land gebruik; anticiperen op de consequenties van gelijktijdige verandering in land- en watersystemen vraagt om een diepgaand begrip van hun interacties. Het doel van deze thesis is het vergroten van onze kennis over hoe veranderingen in landgebruik invloed hebben op de watercyclus, bv. door te focussen op de rol van landgebruik in verdampings - en neerslagprocessen boven land.

Deze thesis presenteert eerst de ontwikkeling (Hoofdstuk 2) en beoordeling (Hoofdstuk 3) van het op processen gebaseerde water balans model STEAM (Simple Terrestrial Evaporation to Atmosphere Model). STEAM simuleert vijf verschillende verdampingsfluxen, waarbij landgebruik wordt gerepresenteerd met een beperkt aantal parameters. Een vergelijking met onafhankelijke data laat zien dat STEAM de verdampingsverdeling en hydrologische fluxen realistisch kan produceren op verschillende locaties, voor verschillende seizoenen en verschillende landgebruik types.

Hoofdstuk 4 onderzoekt de tijdsafhankelijke karakteristieken van verschillende verdampingscomponenten en laat zien dat de verblijftijdschaal van continentale verdamping (dagen tot maanden) substantieel langer is dan die van interceptie (uren). Het vermogen van de vegetatie om te transpireren door water eerst op te slaan in de bodem en het hier later weer uit te halen, is essentieel voor de verdamping in de droge periode; de substantiële verschillen in tijdsafhankelijke karakteristieken tussen verdampingsfluxen kunnen contrasterende vochtrecyclingspatronen veroorzaken.

Gezien het belang van de bergingscapaciteit van de wortelzone voor het simuleren van transpiratie en vochtrecycling, presenteert Hoofdstuk 5 een op 'aardobservatie gebaseerde' methode om deze cruciale parameter in landoppervlakte modellering te schatten. Door aan te nemen dat vegetatie niet dieper wortelt dan nodig om kritische droge periodes te overbruggen, kon satelliet gebaseerde verdamping worden gebruikt om de bergingscapaciteit van de wortelzone af te leiden. Deze nieuwe schatting verbeterde de gehele simulatie van verdamping, vooral tijdens de maanden met de minste verdamping in semi-vochtige en vochtige gebieden met gemiddelde en sterke seizoensgebondenheid. De resultaten suggereren dat verscheidene bostypes in staat zijn een grote berging te creëren als buffer voor ernstige droge periodes, dit in tegenstelling tot grasland en landbouwgewassen.

Gebaseerd op de nieuwe inzichten, analyseert Hoofdstuk 6 de effecten van veranderingen in landgebruik op rivierafvoeren. In een aantal van de wereld's grootste stroomgebieden bleek neerslag meer te worden beïnvloed door veranderingen in landgebruik buiten het stroomgebied dan veranderingen binnen het stroomgebied zelf. In verscheidene niet-grensoverschrijdende stroomgebieden worden de rivierafvoeren voor een groot deel beïnvloed door veranderingen in landgebruik in andere landen, wat

aanleiding kan zijn voor nieuwe grensoverschrijdende water gerelateerde afspraken in de internationale politiek.

Deze thesis bespreekt verschillende domeinen van de watercyclus om ons begrip van land-water interacties te verbeteren. Elke water flux en berging heeft ons onderzoek nodig, ongeacht of ze zichtbaar in rivieren stroomt, onzichtbaar door de lucht beweegt of diep in de bodem en in wortels is verborgen. Omdat de watercyclus interactie heeft met land, en dus met menselijke activiteiten, zijn we in de bijzondere positie om zijn pad en tred te bepalen.

NOTATIONS

α	–	Albedo
β	–	Evaporation efficiency, i.e. the portion of evaporation evaporated during certain conditions
γ	kPa K^{-1}	Psychrometric constant
Δn	h	Time step, 24 h
Δt	h	Time step, 3 h
δ	kPa K^{-1}	Slope of the saturated vapour pressure curve
η_{clay}	%	Clay content of the topsoil
Θ_{top}	–	Effective saturation of topsoil
θ_{top}	–	Volumetric soil moisture content of topsoil
$\theta_{\text{top,sat}}$	–	Volumetric soil moisture content of topsoil at saturation
$\theta_{\text{top,res}}$	–	Volumetric soil moisture content of topsoil at residual point
θ_{uz}	–	Volumetric soil moisture content of the unsaturated zone
$\theta_{\text{uz,fc}}$	–	Volumetric soil moisture content at field capacity in the unsaturated zone
$\theta_{\text{uz,paw}}$	–	Maximum plant available volumetric soil moisture content in the unsaturated zone
$\theta_{\text{uz,wp}}$	–	Volumetric soil moisture content at wilting point
κ	–	Von Kármán constant, 0.41
λ	MJ kg^{-1}	Latent heat of vaporisation of water
ξ_{mw}	–	Ratio of the molecular weight of water vapour to that for dry air, 0.622
ρ_{a}	kg m^{-3}	Density of air
ρ_{w}	kg m^{-3}	Density of water
σ	–	Standard deviation
τ_{ts}	day	Mean terrestrial timescale
ϕ_{lu}	–	Land-use fraction
ϕ_{ow}	–	Open-water fraction
ϕ_{vs}	–	Vegetation in soil fraction
ϕ_{vw}	–	Vegetation in water fraction
χ	h	Topsoil moisture dry-out time parameter
χ_{min}	h	Minimum topsoil moisture dry-out time parameter, 60 h
C_p	MJ kg^{-1} K^{-1}	Heat capacity of water at constant pressure, 1.01×10^{-3} MJ kg^{-1} K^{-1}
c_{AR}	–	Area reduction factor, 0.4
c_{D1}	–	Vapour pressure stress parameter, 3
c_{D2}	–	Vapour pressure stress parameter, 0.1

c_R	–	Radiation stress parameter, 100
c_{sc}	–	Storage capacity factor, 0.2
c_{uz}	–	Soil moisture stress parameter, 0.07
$D_{0.5}$	kPa	Vapour pressure deficit coefficient, 1.5 kPa
D_a	kPa	Vapour pressure deficit
d	m	Zero-plane displacement
E	$m\,d^{-1}$	Total evaporation
E_c	$m\,d^{-1}$	Continentally recycled evaporation
E_f	$m\,d^{-1}$	Floor interception evaporation
$E_{f,lu,vs}$	$m\,(\Delta t)^{-1}$	Land-use-specific floor interception evaporation in ϕ_{vs}
E_i	$m\,d^{-1}$	Direct evaporation, i.e., sum of E_v, E_f, E_{sm}, and E_w
E_o	$m\,d^{-1}$	Evaporation that precipitates on the ocean
E_p	$m\,(\Delta t)^{-1}$	Potential evaporation
$E_{p,day}$	$m\,d^{-1}$	Potential evaporation
E_{sm}	$m\,d^{-1}$	Soil moisture evaporation
$E_{sm,lu,vs}$	$m\,(\Delta t)^{-1}$	Land-use-specific soil moisture evaporation in ϕ_{vs}
E_t	$m\,d^{-1}$	Transpiration evaporation
$E_{t,lu,vs}$	$m\,(\Delta t)^{-1}$	Land-use-specific transpiration in ϕ_{vs}
$E_{t,lu,vw}$	$m\,(\Delta t)^{-1}$	Land-use-specific transpiration in ϕ_{vw}
E_v	$m\,d^{-1}$	Vegetation interception evaporation
$E_{v,lu,vs}$	$m\,(\Delta t)^{-1}$	Land-use-specific vegetation interception evaporation in ϕ_{vs}
$E_{v,lu,vw}$	$m\,(\Delta t)^{-1}$	Land-use-specific vegetation interception evaporation in ϕ_{vw}
E_w	$m\,d^{-1}$	Open-water evaporation
$E_{w,lu,ow}$	$m\,(\Delta t)^{-1}$	Land-use-specific water evaporation in ϕ_{ow}
$E_{w,lu,vw}$	$m\,(\Delta t)^{-1}$	Land-use-specific open-water evaporation in ϕ_{ow}
e_a	kPa	Actual vapour pressure
e_s	kPa	Saturated vapour pressure
F_k	$L^3\,T^{-1}$	Moisture flux over the boundary of a grid cell in the atmospheric layer k
F_v	$L^3\,T^{-1}$	Vertical moisture flux
G	$MJ\,m^{-2}\,d^{-1}$	Ground heat flux
h	m	Plant height
h_{max}	m	Minimum plant height
h_{min}	m	Maximum plant height
I_a	-	Aridity index
I_f	$m\,d^{-1}$	Irrigation applied to S_f
I_g	$m\,d^{-1}$	Gross irrigation
I_{isd}	-	Interstorm duration index
I_{req}	$m\,(\Delta t)^{-1}$	Irrigation requirement
I_s	-	Seasonality index
I_{uz}	$m\,d^{-1}$	Irrigation applied to S_{uz}
I_v	$m\,d^{-1}$	Irrigation applied to S_v
i_{GS}	–	Growing-season index
i_{LA}	$m^2\,m^{-2}$	Leaf area index

$i_{\mathrm{LA,eff}}$	$\mathrm{m^2\,m^{-2}}$	Effective leaf area index
$i_{\mathrm{LA,max}}$	$\mathrm{m^2\,m^{-2}}$	Maximum leaf area index
$i_{\mathrm{LA,min}}$	$\mathrm{m^2\,m^{-2}}$	Minimum leaf area index
J_{add}	$\mathrm{m\,(\Delta t)^{-1}}$	Water added in water stores to compensate for lack of horizontal flows
k	–	Function of r_{a} and r_{s}
L	years	Drought return period
N	s	Day length
N_{high}	s	Day length, higher sub-optimal threshold, assumed to be 39 600 s
N_{low}	s	Day length, lower sub-optimal threshold, assumed to be 36 000 s
P	$\mathrm{m\,d^{-1}}$	Total precipitation
P_{c}	$\mathrm{m\,d^{-1}}$	Continentally recycled precipitation
P_{eff}	$\mathrm{m\,d^{-1}}$	Effective precipitation (i.e. overflow from floor interception stock to unsaturated zone stock)
P_{melt}	$\mathrm{m\,d^{-1}}$	Snowmelt
P_{o}	$\mathrm{m\,d^{-1}}$	Precipitation of oceanic origin
P_{rf}	$\mathrm{m\,(\Delta t)^{-1}}$	Rainfall
P_{mathrm}	$\mathrm{m\,(\Delta t)^{-1}}$	Snowfall
P_{tf}	$\mathrm{m\,(\Delta t)^{-1}}$	Throughfall (i.e. overflow from vegetation interception stock to floor interception stock)
p	kPa	Atmospheric pressure
Q_{uz}	$\mathrm{m\,(\Delta t)^{-1}}$	Outlow from S_{uz}
Q_{w}	$\mathrm{m\,(\Delta t)^{-1}}$	Runoff from S_{w}
R^2	–	Coefficient of determination
R_{net}	$\mathrm{MJ\,m^{-2}\,d^{-1}}$	Net radiation
$R_{\mathrm{net,lw}}$	$\mathrm{MJ\,m^{-2}\,d^{-1}}$	Net longwave radiation
R_{sw}	$\mathrm{MJ\,m^{-2}\,d^{-1}}$	Shortwave radiation
r_{a}	$\mathrm{d\,m^{-1}}$	Aerodynamic resistance
$r_{\mathrm{a,f}}$	$\mathrm{d\,m^{-1}}$	Floor aerodynamic resistance
$r_{\mathrm{a,v}}$	$\mathrm{d\,m^{-1}}$	Vegetation aerodynamic resistance
$r_{\mathrm{a,w}}$	$\mathrm{d\,m^{-1}}$	Open-water aerodynamic resistance
r_{s}	$\mathrm{d\,m^{-1}}$	Surface resistance
$r_{\mathrm{s,sm}}$	$\mathrm{d\,m^{-1}}$	Surface soil moisture resistance
$r_{\mathrm{s,sm,min}}$	$\mathrm{d\,m^{-1}}$	Minimum surface soil moisture resistance
$r_{\mathrm{s,st}}$	$\mathrm{d\,m^{-1}}$	Surface stomatal resistance
$r_{\mathrm{s,st,min}}$	$\mathrm{d\,m^{-1}}$	Minimum surface stomatal resistance
S_{f}	m	Floor interception stock
$S_{\mathrm{f,lu}}$	m	Floor interception stock of a specific land-use type
$S_{\mathrm{f,max}}$	m	Floor interception storage capacity
S_{k}	$\mathrm{m^3}$	Atmospheric moisture storage in atmospheric layer k
S_{R}	m	Root zone storage capacity, also referred to as unsaturated storage capacity
S_{snow}	m	Snow stock
S_{uz}	m	Unsaturated stock

$S_{\mathrm{uz,lu}}$	m	Unsaturated stock of a specific land-use type
$S_{\mathrm{uz,sm}}$	m	Unsaturated stock available for soil moisture evaporation
$S_{\mathrm{uz,t}}$	m	Unsaturated stock available for transpiration
S_{v}	m	Vegetation interception stock
$S_{\mathrm{v,lu}}$	m	Vegetation interception stock of a specific land-use type
$S_{\mathrm{v,max}}$	m	Vegetation interception storage capacity
S_{w}	m	Water stock
$S_{\mathrm{w,lu}}$	m	Water stock of a specific land-use type
T_{dew}	K	Dew point temperature
T_{mean}	K	Daily mean temperature
T_{min}	K	Daily minimum temperature
$T_{\mathrm{min,high}}$	K	Daily minimum temperature, higher sub-optimal threshold, 278.15 K
$T_{\mathrm{min,low}}$	K	Daily minimum temperature, lower sub-optimal threshold, 271.15 K
T_{opt}	K	Optimum photosynthesis temperature
u_{10}	$\mathrm{m\,d^{-1}}$	Wind speed at 10 m height
u_{200}	$\mathrm{m\,d^{-1}}$	Wind speed at 200 m height
u_{ref}	$\mathrm{m\,d^{-1}}$	Wind speed at reference height
y_{L}	–	reduced variate of the Gumbel distribution
y_{top}	m	Depth of the topsoil
y_{uz}	m	Depth of the unsaturated zone, also referred to as rooting depth
Z	m	Elevation
z_0	m	Aerodynamic roughness length
$z_{0,\mathrm{f}}$	m	Roughness length of substrate floor
z_{10}	m	Height of wind speed u_{10}
z_{200}	m	Height of wind speed u_{200}
z_{ref}	m	Reference height

CONTENTS

1

INTRODUCTION

While the ancient oceans of Venus and Mars vaporised into space,
Earth kept its life-giving water.

Cynthia Barnett (born 1966)
'Rain - A Natural and Cultural History'

This chapter is partly based on:

Wang-Erlandsson, L., van der Ent, R. J., Gordon, L. J., and Savenije, H. H. G.: *Contrasting roles of interception and transpiration in the hydrological cycle — Part 1: Temporal characteristics over land*, Earth System Dynamics, 5, 441–469, 2014.

Wang-Erlandsson, L., Bastiaanssen, W. G. M., Gao, H., Jägermeyr, J., Senay, G. B., van Dijk, A. I. J. M. Guerschman, J. P., Keys, P. W., van der Ent, R. J., Gordon, L. J., and Savenije, H. H. G.: *Global root zone storage capacity from satellite-based evaporation*, Hydrology and Earth System Sciences, 4, 1459–1481, 2016.

Wang-Erlandsson, L., Fetzer, I., Keys, P., van der Ent, R. J., Savenije, H. H. G. and Gordon, L. J.: *Remote land-use impacts on river flows through atmospheric teleconnections*, Hydrology and Earth System Science Discussions, in review.

1

1.1. UNPRECEDENTED PRESSURE ON LAND AND WATER

Unprecedented is a word more used than ever to describe the state of the planet. Today, four billion people live under severe water scarcity conditions (Mekonnen and Hoekstra, 2016), while more than 40 % of forests and ice-free habitats have been converted to agricultural land or pasture (Foley, 2005; Goldewijk, 2001). The speed of change is just as striking as the state of affairs. Just within the last three hundred years, land-cover change impact on the biosphere in terms of carbon, water, and biodiversity have increased manifold (Hurtt et al., 2011; Newbold et al., 2015; Ostberg et al., 2015; Pimm et al., 2014). Yet, increased pressure is expected from future growth in population and affluence. Until 2030, another 2.85-7.95 Mkm^2 of land is under demand (Lambin and Meyfroidt, 2011) and fresh water withdrawal mostly is expected to increase by 2000 $km^3\ yr^{-1}$ by the end of the century (Wada and Bierkens, 2014). Anticipating the consequences of these simultaneous changes in land and water systems requires an understanding not only of how these systems function separately, but also importantly, of how they interact.

1.2. INTRINSIC LINKAGES BETWEEN LAND AND WATER

Water sustains life by its never ending movement. The Earth's surface receives about 115×10^3 $km^3\ yr^{-1}$ precipitation (rain, snow, sleet, or hail), of which approximately 75×10^3 $km^3\ yr^{-1}$ is evaporated back to the atmosphere, and most of the remaining 40×10^3 $km^3\ yr^{-1}$ flows into rivers to join the ocean (Trenberth et al., 2011). Vegetation and land surface properties directly interact with all of these three fluxes: precipitation, evaporation, and river flows.

While the causal effect of vegetation on river flows and evaporation are possible to study through direct observations, experiments to determine the vegetation's effect on precipitation have been and remain challenging. Already in the mid 1800s, observations demonstrated that precipitation was higher over forests, but the forest's role remained inconclusive as correlation could not be taken as causation (Zon, 1927). In the late 1860s and 1870s, a conspicuous coincidence of exceptionally rainy years and the westward expansion of the European-American settlement led to the wide-held belief that 'rain follows the plow' (Barnett, 2015). However, a return to dry years in North America and a series of influential research (Benton, 1949; Budyko, 1974; McDonald, 1962) concluded that local precipitation is largely unaffected by local evaporation and vegetation. The issue was, however, not settled. The importance of vegetation for local precipitation came to rise again with research in the rainforests, which proved to sustain local rainfall through intense local moisture recycling (Shukla and Mintz, 1982). In recent years, vegetation has been suggested to play an even greater role for rainfall by its ability to attract oceanic moisture through the highly controversial 'biotic pump' mechanism (Makarieva and Gorshkov, 2007; Makarieva et al., 2014; Meesters et al., 2009).

Science today offers a rich picture of how vegetation influences the the water cycle. Precipitation formation is directly dependent on the atmospheric stability, humidity, circulation, and presence of cloud condensation nuclei, each influenced by land surface through e.g., surface roughness, soil moisture state, evaporation rate, and biogenic aerosols (e.g., Shuttleworth, 2012). Based on scale dependency, Goessling and Reick (2011) suggests three categories of mechanisms through which land surface influences

precipitation: local coupling, moisture recycling, and atmospheric circulation. Local coupling is related to perturbation of the thermal layer through e.g., soil moisture feedback (e.g., Koster et al., 2004; Taylor et al., 2012; Guillod et al., 2015); regional scale moisture recycling influences precipitation through changes in upwind evaporation and atmospheric moisture content (van der Ent et al., 2010; Spracklen et al., 2012; Tuinenburg et al., 2012) partly depending on existing convective conditions (Swann et al., 2015); and atmospheric circulation can be perturbed by altered climate dynamics anywhere on Earth through teleconnections (e.g., Avissar and Werth, 2005; Badger and Dirmeyer, 2016; de Vrese et al., 2016). Nevertheless, understanding and representing all complexities in precipitation formation and land-atmosphere interaction has proven to be challenging, and simulations of precipitation and precipitation change from land-use change still vary widely between climate models due to major uncertainties in cloud, aerosol, and circulation model formulations (Pitman et al., 2012; Chen and Frauenfeld, 2014; Aloysius et al., 2016).

In this context, the study of the moisture recycling mechanism offers a simpler first order estimate for understanding regional scale land-use change effects and a starting point for interpreting climate model simulations. The knowledge about regional interactions between vegetation and moisture recycling is backed up by observations (e.g., D'Almeida et al., 2007; Spracklen et al., 2012), and simulations of moisture sources are fairly robust (Keys et al., 2014). About 40 % of terrestrial precipitation originates from terrestrial evaporation (van der Ent et al., 2010, 2014), but the degree of moisture recycling varies greatly with geography as a function of wind directions, distance to ocean, evaporation rates, precipitation rates, and topography. Precipitation recycling ratios are highest in north-east Euroasia, west-central Africa, and central South America, where more than 60 % of precipitation originate from evaporation with terrestrial origin (van der Ent et al., 2010, 2014).

Thus, a number of studies have focused on the moisture recycling mechanism to explore the consequences of anthropogenic land-use change. For example, Bagley et al. (2012) used a linear moisture availability model to show that changes in land use can potentially decrease crop yields through reductions in moisture recycling; Tuinenburg (2013) and Wei et al. (2012) showed that irrigation can increase downwind rainfall; and Keys et al. (2012) and Miralles et al. (2016) showed that some semiarid regions are particularly vulnerable to changes in their own moisture supply or upwind moisture source regions. Focusing on the moisture recycling mechanism has also enabled innovative application of network analysis of e.g., the risk of self-amplifying forest loss (Zemp et al., 2017).

1.2.1. EVAPORATION PARTITIONING — IS TIME OF THE ESSENCE?

Moisture recycling studies have in the past only analysed total evaporation. However, total evaporation consists of transpiration, interception, and soil moisture evaporation, which contrast in their temporal dynamics on land. For example, interception and soil moisture evaporation are ephemeral (Gerrits et al., 2009), whereas transpiration continues long into the dry season depending on infiltration rates and the capacity of the soil in the root zone to retain moisture. Therefore, the interception moisture feedback to the atmosphere often occurs instantaneously during a rainfall event, whereas transpiration occurs when there

is no longer any local condition for rain. Based on studies in Zimbabwe, Sahel, and the Amazon, Savenije (2004) suggested that the temporal differences of different evaporation fluxes result in different contribution to moisture recycling. With the development of global scale hydrological and moisture recycling models, the temporal dynamics of different evaporation fluxes can now be studied worldwide.

1.2.2. ROOT ZONE STORAGE CAPACITY — WHAT IS BENEATH THE SURFACE?

A key uncertainty in moisture recycling studies is evaporation partitioning, and global estimates of transpiration ratio ranges between 35 and 90 % of total evaporation (Coenders-Gerrits et al., 2014). A contributing factor to the uncertainty is the lack of a reliable global root zone storage capacity dataset. Root zone storage capacity (S_R) determines the maximum amount of soil moisture potentially available for vegetation transpiration, and is critical for correctly simulating land-atmosphere interactions (e.g., Bevan et al., 2014; Feddes et al., 2001; Kleidon and Heimann, 1998b, 2000; Lee et al., 2005; Milly and Dunne, 1994; Zeng et al., 1998). However, root zone storage capacity is very difficult to measure and observe in the field, especially at the larger scales that are relevant for many modelling needs. Rooting profiles measurements are also scarce, and difficult to generalise since vegetation rooting systems naturally adapt to prevailing climates and soil heterogeneities (e.g., Gentine et al., 2012; Sivandran and Bras, 2013). Even when rooting profiles are available, difficulties arise in translating them to root zone storage capacity, due to variations in root densities, hydrological activity, horizontal and vertical heterogeneities, and uncertainties in soil profile data. Recent advances in satellite based techniques, however, offer new possibilities to inspect the hydrological root zone depth.

1.2.3. LAND-USE CHANGE IMPACTS ON RIVER FLOWS — FAR AND NEAR

Moisture recycling studies have hitherto focused on precipitation and evaporation, and less on river flows. Paradoxically, perhaps due to a divide between the atmospheric and the hydrological disciplines, hydrological studies of land-use change effects on the water cycle have largely focused on the perturbation of river flows. Even though several studies suggest land system change to be the most important driver of past century (e.g., Piao et al., 2007; Sterling et al., 2012) and projected changes in river flows (Betts et al., 2015), they have either ignored that vegetation change influences precipitation or do not distinguish between the effects of land-use change within and outside the river basin boundary. While Stickler et al. (2013) demonstrated contrasting effects of local and regional deforestation on hydropower energy generation in the Amazon, questions remain on the moisture recycling mechanisms through which land-use change affects river flows.

1.3. RESEARCH QUESTIONS AND THESIS OUTLINE

Against the backdrop of the grand global challenges in understanding and achieving land–water sustainability, this thesis takes aim to advance our knowledge of *how land-use change influences the water cycle.*

Chapter 2 describes the global hydrological model Simple Terrestrial Evaporation to Atmosphere Model (STEAM), which was developed for and used in this thesis. Chapter 3

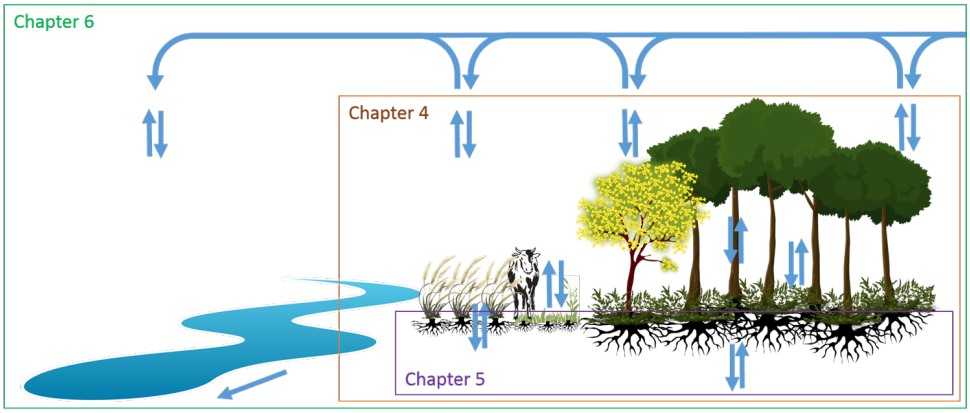

Figure 1.1: Different domains in the terrestrial water cycle covered by the different chapters. Chapter 4 focuses on the evaporation fluxes on land, Chapter 5 zooms in to the root zone storage capacity, and Chapter 6 zooms out to include moisture recycling and river flows.

describes the evaluation of the model.

Chapters 4-6 address different domains in the terrestrial water cycle, as illustrated in Fig. 1.1. The specific research questions addressed in these chapters are as follows:

- Chapter 4: What are the temporal characteristics of interception and transpiration in the terrestrial water cycle?
- Chapter 5: Can global root zone storage capacity estimates be improved using satellite-based evaporation data, and thus, improve global hydrological simulation?
- Chapter 6: How does anthropogenic land-use change affect river flows through moisture recycling?

Finally, Chapter 7 synthesises the findings and discusses future research needs.

2

SIMPLE TERRESTRIAL EVAPORATION TO ATMOSPHERE MODEL (STEAM)

'I have never tried that before,
so I think I should definitely be able to do that.'

Astrid Lindgren, (1907-2002)
'*Pippi Longstocking*'

Simple Terrestrial Evaporation to Atmosphere Model (STEAM) is a process-based, water balance model, developed to analyse land-use change impacts on the water cycle. STEAM simulates five evaporation fluxes at 3 hours resolution: vegetation interception, floor interception, transpiration, soil moisture evaporation, and open water evaporation. The goal of STEAM is to represent different land-use classes with only a limited number of parameters, and yet to produce realistic partitioning between direct and delayed evaporation. Because of our need to properly quantify evaporation and its seasonal variations, STEAM includes an irrigation module and calculates dynamic seasonal vegetation parameters based on meteorological conditions. STEAM is useful for understanding the links between land use and water resources, and can with benefit be employed on par with atmospheric moisture tracking.

This chapter is based on:

Wang-Erlandsson, L., van der Ent, R. J., Gordon, L. J., and Savenije, H. H. G.: *Contrasting roles of interception and transpiration in the hydrological cycle – Part 1: Temporal characteristics over land*, Earth System Dynamics, 5, 441–469, 2014.

2.1. Introduction

Global land evaporation data can be obtained from reanalysis, observations, and land surface model simulations (Mueller et al., 2013; Wang and Dickinson, 2012). All three data categories have their merits and shortcomings. Reanalysis data are generated from data assimilation based on numerical weather forecast model simulations and available observations from multiple sources (Dee et al., 2011). They have global coverage and offer high temporal resolution. However, because of the data assimilation procedure, the water balance is not closed and evaporation estimates are likely too high. Observation-based data can come from satellite retrieval and eddy covariance measurements network. Notwithstanding being close to ground truth, there are uncertainties and bias specific to each observation technique, and the temporal resolution of available observation-based data is often poor.

Land surface model simulations are the only category to provide evaporation partitioning at the high temporal resolution required for input to a moisture tracking model. However, most global land surface models have been developed for other types of use, such as to solve surface energy exchanges in climate simulations or to estimate river discharge for assessment of water availability (e.g., Haddeland et al., 2011). While some of them offer a comprehensive description of a large set of Earth system dynamics, they do not necessarily simulate evaporation partitioning realistically. Features important for evaporation partitioning, such as phenology and irrigation, are not always included in land surface models. Land surface models also normally do not simulate interception on other surfaces than tree canopy, despite otherwise suggested by field studies (e.g., Gerrits et al., 2010; De Groen and Savenije, 2006; Putuhena and Cordery, 1996; Savenije, 2004).

2.2. Model rationale

We developed the Simple Terrestrial Evaporation to Atmosphere Model (STEAM) as a process-based model assuming water balance at grid cell level. The original aim was to use STEAM to analyse land-use change impacts on the water cycle, separately or on par with the moisture tracking model Water Accounting Model-2layers (WAM-2layers) (van der Ent et al., 2014). The goal of STEAM is to represent different land-use classes with only a limited number of parameters, and yet to produce realistic partitioning between direct and delayed evaporation. The temporal and spatial resolution of STEAM is chosen to work together with WAM-2layers. Because of our need to properly quantify evaporation and its seasonal variations, STEAM includes an irrigation module and calculates dynamic seasonal vegetation parameters based on meteorological conditions.

STEAM can be considered a simple model with its pure focus on the evaporation process. For our current research purposes, we have considered it acceptable to disregard groundwater interaction and lateral flows. Complex models are necessary for holistic earth system modelling, but a simple model approach is convenient when only a few aspects of the Earth system are considered. A simple model is more transparent, contains fewer uncertain 'best guess' equations and parameters, and is more flexible to change. When targeting a specific aspect, (in our case evaporation partitioning and the link to moisture recycling), a simple model may even outperform more complex models that do not take the specific aspect into account or that has to compromise it with other aspects

(Orth et al., 2015).

2.3. MODEL DESCRIPTION

STEAM estimates five evaporative fluxes, and is represented by five stocks, see Fig. 2.1. The vegetation interception stock S_v represents canopy and vegetation surfaces (such as leafs, branches, and stems) that are the first to be wetted by rainfall ($P - P_{sf}$). The evaporation from this stock is vegetation interception E_v, and the water exceeding the vegetation interception storage capacity $S_{v,\,max}$ is throughfall P_{tf}. In most cases, the latter is intercepted by the ground and litter surface, forming a thin layer of the floor interception stock S_f. The evaporation from this stock is floor interception E_f. The remainder is effective precipitation P_{eff}, which is generated when the floor interception storage capacity $S_{f,\,max}$ is exceeded. Water that subsequently reaches the unsaturated root zone stock S_{uz} can be evaporated either as soil moisture evaporation E_{sm}, or be taken up by plant roots and transpire as E_t. In addition to these stocks, we assume that the land-cover types 'Water' (01:WAT) and 'Wetlands' (12:WET) contain open water, and that vegetation may grow directly in water, in 'Wetlands' (12:WET) and 'Rice paddies' (19:RIC), see Table 2.2. These waters are represented by the water stock S_w. Open water is replenished by adding water J_{add} that prevents dry-out in the absence of lateral flow routines. Vegetation covered water also receives P_{tf} from vegetation. Runoff is the sum of excess water Q_{uz} (exceeding the unsaturated root zone storage capacity S_R) from the unsaturated zone and Q_w from the water stock (exceeding the water storage capacity $S_{w,\,max}$). The last and fifth stock S_{snow} does not have a limit, and allows snowfall P_{sf} to accumulate until melting occurs. Snowmelt P_{melt} is allowed only if there is snow in S_{snow} and only up to the given amount of snowmelt given by the data. If the daily mean temperature T_{mean} is above 273 K, P_{melt} goes directly to the floor interception stock, otherwise it does not infiltrate and leaves directly as runoff Q_{uz}. In case of irrigation, some water is assumed to be spilled to the vegetation I_v, the floor I_f and the water bodies I_w. The parameterisation of the storage capacities are described in Sect. 2.3.4 and all notations are listed in Notations.

2.3.1. POTENTIAL EVAPORATION

PENMAN-MONTEITH EQUATION

Total evaporation – the sum of vegetation interception E_v, floor interception E_f, transpiration E_t, soil moisture evaporation E_{sm}, and open-water evaporation E_w – is driven by the daily potential evaporation and restricted by resistances and water availability. The Penman–Monteith equation (Monteith, 1965) is used to estimate the daily potential evaporation $E_{p,\,day}$ [m d^{-1}], which is formulated as follows:

$$E_{p,\,day}\,(r_a) = \frac{\delta\,(R_{net} - G) + \rho_a C_p D_a / r_a}{\rho_w \lambda\,(\delta + \gamma)}, \tag{2.1}$$

where δ [kPa K^{-1}] is the gradient of the saturated vapour pressure function, R_{net} [MJ m^{-2} d^{-1}] is the net radiation, G [MJ m^{-2} d^{-1}] is the ground heat flux, ρ_a [kg m^{-3}] is the density of air, C_p [1.01×10^{-3} MJ kg^{-1} K^{-1}] is the specific heat of moist air at constant pressure, D_a [kPa] is the vapour pressure deficit, ρ_w [kg m^{-3}] is the density of water,

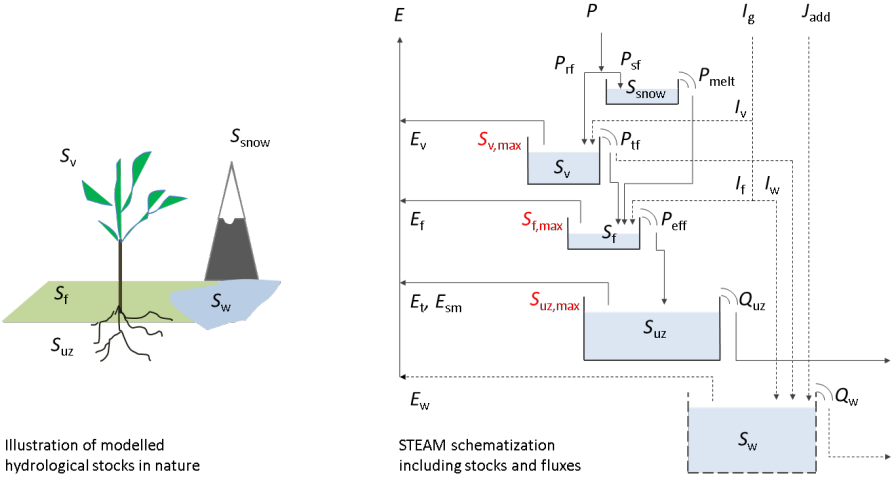

Figure 2.1: Water fluxes and stocks in STEAM. Arrows indicate fluxes, and boxes indicate stocks. Dashed lines indicate fluxes and stocks that only exist for particular land-use types. Symbols are listed in Notations.

λ [MJ kg^{-1}] is the latent heat of water vaporisation, γ [kPa K^{-1}] is the psychrometric constant, and r_a [d m^{-1}] is the aerodynamic resistance. Note that r_a is represented by $r_{a,v}$ for vegetation, $r_{a,f}$ for floor, and $r_{a,w}$ for water. The calculations of δ, R_{net}, G, D_a, λ, γ, and the different r_a's are given in Sect. 2.3.1. The potential evaporation $E_{p,day}$ in Eq. (2.1) does not include surface stomatal resistance $r_{s,st}$ for transpiration or surface soil moisture resistance $r_{s,sm}$ for soil moisture evaporation. Thus, we introduce k (used in Eqs. 2.30, 2.32, and 2.33), which is expressed as a function of a surface resistance r_s and an aerodynamic resistance r_a:

$$k(r_s, r_a) = \left(1 + \frac{r_s}{r_a}\frac{\gamma}{\delta+\gamma}\right)^{-1}. \tag{2.2}$$

SURFACE RESISTANCE

Surface resistance applies only to soil moisture evaporation and transpiration, since interception and open-water evaporation occur without resistance.

The soil moisture resistance $r_{s,sm}$ is applied to soil moisture evaporation and estimated based on the soil moisture content of the topsoil layer (Bastiaanssen et al., 2012):

$$r_{s,sm} = r_{s,sm,min}\Theta_{top}^{-3}, \tag{2.3}$$

where $r_{s,sm,min}$ is the minimum surface soil moisture resistance assumed as 3.5×10^{-4} d m^{-1}, and Θ_{top} [–] is the effective saturation expressed as

$$\Theta_{top} = \frac{\theta_{top,n} - \theta_{top,res}}{\theta_{top,sat} - \theta_{top,res}}. \tag{2.4}$$

The surface stomatal resistance $r_{s,st}$ of vegetation is simulated by the Jarvis–Stewart equation (Stewart, 1988), taking into account solar radiation, vapour pressure deficit, optimum temperature, and soil moisture stress:

$$r_{s,st} = \frac{r_{s,st,min}}{i_{LA,eff} f(R_{sw}) f(D_a) f(T_{mean}) f(\theta_{uz})}, \tag{2.5}$$

where $r_{s,st,min}$ is the minimum surface stomatal resistance dependent on land-use type and specified in the land-use look-up table (Table 2.1); $i_{LA,eff}$ is the effective leaf area index (unit leaf area per unit ground area that is actively participating in transpiration); and f is the four stress functions for incoming shortwave radiation R_{sw} (in W m^{-2}), vapour pressure deficit D_a, mean daily temperature T_{mean}, and soil moisture θ_{uz} (Stewart, 1988). Effective leaf area index $i_{LA,eff}$ is adapted from Allen et al. (2006) and Zhou et al. (2006) as

$$i_{LA,eff} = \frac{i_{LA}}{0.2 i_{LA} + 1}. \tag{2.6}$$

The stress functions vary between 0 and 1. The stress function of soil moisture $f(\theta_{uz})$ is the same as in Eq. (2.41). The other stress functions are as follows (Jarvis, 1976; Zhou et al., 2006; Matsumoto et al., 2008):

$$f(R_{sw}) = R_{sw}(1 + c_R/1000)(c_R + R_{sw})^{-1}, \tag{2.7}$$

$$f(D_a) = \left[1 + (D_a/D_{0.5})^{c_{D1}}\right]^{-1}(1 - c_{D2}) + c_{D2}, \tag{2.8}$$

$$f(T_{mean}) = \begin{cases} 0 & T_{mean} < 273.15 \\ 1 - T_{opt}^{-2}\left(T_{mean} - T_{opt}\right)^2 & \left(T_{mean} > T_{opt} + 1\right) \cup \\ & \left(273.15 \le T_{mean} < T_{opt} - 1\right) \\ 1 & T_{opt} - 1 \le T_{mean} \le T_{opt} + 1 \end{cases} \tag{2.9}$$

where c_R is the radiation stress parameter fixed at 100 (Zhou et al., 2006), $D_{0.5}$ is the vapour pressure deficit halfway between 1 and c_{D2} set at 1.5 kPa, c_{D1} is the first vapour pressure parameter set at 3, and c_{D2} is the second vapour pressure stress parameter set at 0.1 (Matsumoto et al., 2008). Optimum temperature T_{opt} [K] is based on elevation above sea level Z [m] and latitude ω [rad] (Cui et al., 2012):

$$T_{opt} = 302.45 - 0.003(Z - |\omega|). \tag{2.10}$$

Graphical representations of the stress functions are presented in Fig. 2.2. Under unfavourable conditions where at least one of the stress functions equals 0, $r_{s,st}$ is assumed to be 0.58 d m^{-1} (50 000 s m^{-1}), corresponding to the molecular diffusivity of water vapour through leaf cuticula (Tourula and Heikinheimo, 1998). If i_{LA} is 0, no transpiration is allowed.

OTHER INPUT VARIABLES TO THE PENMAN–MONTEITH EQUATION

The vapour pressure deficit D_a is defined as

$$D_a = e_s - e_a(T_{dew}), \tag{2.11}$$

where e_s [kPa] is the saturated vapour pressure at temperature T_{mean} [K] and estimated from the average of the saturated vapour pressures of the daily maximum and minimum temperature, e_a [kPa] is the vapour pressure of air at height z_{ref} [m], and T_{dew} [K] is the daily mean dew point temperature. Vapour pressure e_a is estimated from the formula below:

$$e_a(T_{dew}) = \frac{0.6108 \cdot e_a^{17.27(T_{dew}-273.15)}}{T_{dew} - 35.85}. \tag{2.12}$$

For the estimation of e_s, T_{dew} was replaced by T_{max} or T_{min}. The latent heat of water vaporisation λ [MJ kg^{-1}] is expressed as

$$\lambda = 2.501 - 0.002361\,(T_{mean} - 273.15). \tag{2.13}$$

The gradient δ [kPa K^{-1}] of the saturated vapour pressure function is given by

$$\delta = \frac{4098 \cdot e_s}{237.3 + (T_{mean} - 273.15)^2}. \tag{2.14}$$

The psychrometric constant γ [kPa K^{-1}] is

$$\gamma = \frac{C_p p}{\xi_{mw} \lambda}, \tag{2.15}$$

where p is the atmospheric pressure [kPa], and ξ_{mw} is the ratio of the molecular weight of water vapour to that for dry air [0.622].

Net radiation is calculated by

$$R_{net} = (1 - \alpha) R_{sw} - R_{net,lw}, \tag{2.16}$$

where α is albedo, R_{sw} is the incoming shortwave radiation, and $R_{net,lw}$ is the outgoing net longwave radiation. In reality, albedo varies with angle of reflection and the surface properties such as snow cover change and soil wetness. Here, we assume α to be fixed for each land-use type; see Table 2.1.

Daily ground heat flux G is derived from interpolating monthly ground heat flux G_{month} (Allen et al., 1998):

$$G_{month} = 0.07\,(T_{month+1} - T_{month-1}). \tag{2.17}$$

There are three types of aerodynamic resistances used in STEAM: the aerodynamic vegetation resistance $r_{a,v}$, the aerodynamic floor resistance $r_{a,f}$, and the aerodynamic

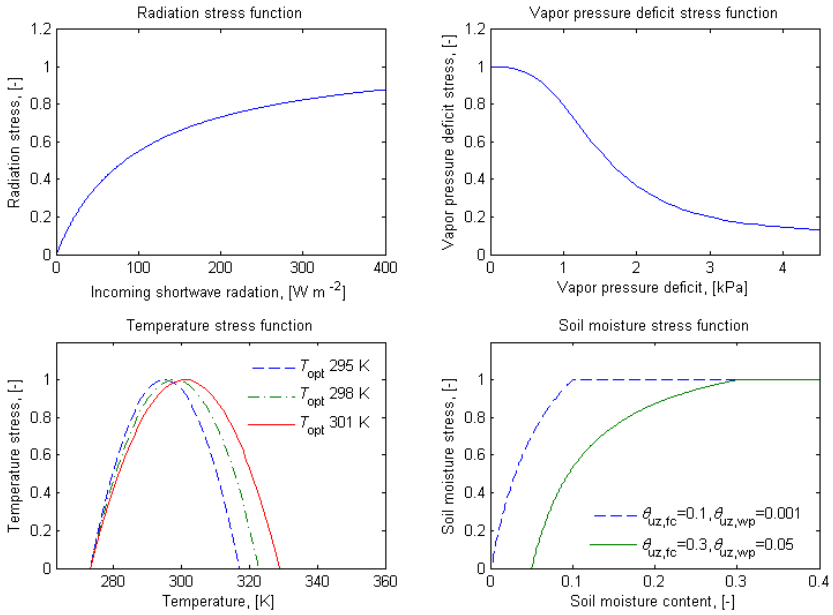

Figure 2.2: Stress functions used in the Jarvis–Stewart equation (see Eq. 2.5).

water resistance $r_{a,w}$. They are expressed as follows (Shuttleworth, 2012):

$$r_{a,v} = \frac{\ln \frac{z_{ref}-d}{z_0} \ln \frac{z_{ref}-d}{0.1 z_0}}{u_{ref,v} \kappa^2}, \tag{2.18}$$

$$r_{a,f} = \frac{\ln \frac{z_{ref,f}}{z_{0,f}} \ln \frac{z_{ref,f}}{0.1 z_{0,f}}}{u_{ref,f} \kappa^2}, \tag{2.19}$$

$$r_{a,w} = \frac{4.72 \ln^2 \frac{z_{ref,w}}{z_{0,f}}}{1 + 0.536 u_{ref,w}}, \tag{2.20}$$

where z_{ref} is the reference height [m], z_0 is the aerodynamic roughness length [m], d is the zero-plane displacement height [m], and u_{ref} is the wind speed [m d^{-1}] at z_{ref}. Wind speed u_{ref} is estimated from wind speed u_{10} given by data at 10 m z_{10} [m] under the assumption of a logarithmic wind profile and stable neutral atmospheric conditions:

$$u_{ref,f} = u_{10} \frac{\ln \frac{z_{ref,f}}{z_{0,f}}}{\ln \frac{z_{10}}{z_{0,f}}}, \tag{2.21}$$

$$u_{ref,w} = u_{10} \frac{\ln \frac{z_{ref,w}}{z_{0,f}}}{\ln \frac{z_{10}}{z_{0,f}}}, \tag{2.22}$$

where the reference height $z_{\mathrm{ref,f}}$ and $z_{\mathrm{ref,w}}$ are 2 m and $z_{\mathrm{ref,v}}$ is $2+h$ [m], with h being the plant height [m]. However, because some vegetation is higher than 10 m, wind speed at 200 m is substituted into the formula to derive wind speeds at lower elevations:

$$u_{\mathrm{ref,v}} = u_{10} \frac{\ln\left(\frac{z_{200}}{z_0}\right)}{\ln\left(\frac{z_{10}}{z_0}\right)} \frac{\ln\left(\frac{z_{\mathrm{ref,v}}-d}{z_0}\right)}{\ln\left(\frac{z_{200}-d}{z_0}\right)}. \tag{2.23}$$

The aerodynamic roughness length z_0 [m] is estimated from

$$z_0 = \begin{cases} z_{0,\mathrm{f}} + 0.29h\sqrt{0.2 i_{\mathrm{LA}}} & i_{\mathrm{LA}} \le 1 \\ 0.3h\,(1-d/h) & i_{\mathrm{LA}} > 1 \end{cases}. \tag{2.24}$$

Zero-plane displacement d is estimated from h [m] and i_{LA} m^2 m^{-2}:

$$d = 1.1h \ln\left[1 + (0.2 i_{\mathrm{LA}})^{0.25}\right], \tag{2.25}$$

$$h = h_{\min} + (h_{\max} - h_{\min})\, i_{\mathrm{LA}} / i_{\mathrm{LA,max}}. \tag{2.26}$$

TOP SOIL MOISTURE

Since there is no explicit topsoil storage in STEAM, topsoil moisture at the present time $\theta_{\mathrm{top},n}$ [–] is derived daily, based on the inflow to the unsaturated storage and topsoil moisture from the previous day $\theta_{\mathrm{top},n-1}$ (Pellarin et al., 2013):

$$\theta_{\mathrm{top},n} = \theta_{\mathrm{top},n-1} e^{-\Delta n/\chi} + \left(\theta_{\mathrm{sat}} - \theta_{\mathrm{top},n-1}\right)\left(1 - e^{-P_{\mathrm{eff}}/y_{\mathrm{top}}}\right) + \theta_{\mathrm{top,res}}, \tag{2.27}$$

where Δn is the time step of 24 h, $\theta_{\mathrm{top,res}}$ is the volumetric residual soil moisture content assumed as 0.01, y_{top} is the topsoil depth, and χ is the dry-out parameter which varies with clay content of the topsoil. The assumed y_{top} is 0.03 m. In Pellarin et al. (2013), the values used for y_{top} were 0.05 and 0.1 m, but we considered that a shallower depth is more relevant for estimating soil moisture evaporation stress. The dry-out parameter χ is estimated using the following semi-empirical equation:

$$\chi = \frac{y_{\mathrm{top}}}{0.1} \max\left[\chi_{\min}, 32 \ln\left(\eta_{\mathrm{clay}} + 174\right)\right], \tag{2.28}$$

where η_{clay} is the clay content [%] and $\chi_{\min}$ is the minimum of χ taken as 60 h. This set of equations (Eqs. 2.27 and 2.28) was tested in semi-arid west Africa, in the type of regions where soil moisture evaporation is most important. Factors not taken into account include solar radiation, the presence of vegetation and the wind velocity (Pellarin et al., 2013).

2.3.2. ACTUAL EVAPORATION

To simulate actual evaporation at 3 h time steps (Δt), we first downscale the daily potential evaporation $E_{\mathrm{p,day}}$ using the diurnal distribution of actual 3 h evaporation data. The downscaled potential evaporation is subsequently used to evaporate moisture in the following logical sequence – vegetation interception, transpiration, floor interception, and soil moisture evaporation:

$$E_{\mathrm{v,lu,vs}} = E_{\mathrm{v,lu,vw}} = \min\left(\frac{S_{\mathrm{v,lu}}}{\Delta t}, E_{\mathrm{p}}\left(r_{\mathrm{a,v}}\right)\right), \tag{2.29}$$

$$E_{\mathrm{t,lu,vs}} = \min\left(\frac{S_{\mathrm{uz,lu}}}{\Delta t}, \max\left\{0, \left[E_{\mathrm{p}}\left(r_{\mathrm{a,v}}\right) - E_{\mathrm{v,lu,vs}}\right] k\left(r_{\mathrm{a,v}}, r_{\mathrm{s,st}}\right)\right\}\right), \tag{2.30}$$

$$E_{\mathrm{f,lu,vs}} = \min\left(\frac{S_{\mathrm{f,lu}}}{\Delta t}, \max\left[0, E_{\mathrm{p}}\left(r_{\mathrm{a,f}}\right) - E_{\mathrm{v,lu,vs}} - E_{\mathrm{t,lu,vs}}\right]\right), \tag{2.31}$$

$$E_{\mathrm{sm,lu,vs}} = \min\left(\frac{S_{\mathrm{uz,lu}}}{\Delta t}, a\right), \tag{2.32}$$

$$a = \max\left\{0, \left[E_{\mathrm{p}}\left(r_{\mathrm{a,f}}\right) - E_{\mathrm{v,lu,vs}} - E_{\mathrm{t,lu,vs}} - E_{\mathrm{f,lu,vs}}\right] k\left(r_{\mathrm{a,f}}, r_{\mathrm{s,sm}}\right)\right\},$$

where the first subscript ($_{\mathrm{v}}$, $_{\mathrm{t}}$, $_{\mathrm{f}}$, $_{\mathrm{sm}}$, or $_{\mathrm{w}}$) denotes an individual evaporative flux; the second subscript ($_{\mathrm{lu}}$) the land-use type ID (see Table 2.1); and the third subscript ($_{\mathrm{vs}}$, $_{\mathrm{vw}}$, or $_{\mathrm{ow}}$) the type of vegetation-water occupancy (see Table 2.2). Thus, for the fraction of vegetation in water ϕ_{vw} in wetlands and rice paddies, there is no floor interception or soil evaporation. Here, transpiration is preceded by vegetation interception just as for the fraction of vegetation in soil ϕ_{vs}, whereas open-water evaporation takes the position of floor interception in the evaporation sequence and is preceded by both vegetation interception and transpiration:

$$E_{\mathrm{t,lu,vw}} = \min\frac{S_{\mathrm{w,lu}}}{\Delta t}, \max\left\{0, E_{\mathrm{p}}\left(r_{\mathrm{a,v}}\right) - E_{\mathrm{v,lu,vw}} k\left(r_{\mathrm{a,v}}, r_{\mathrm{s,st}}\right)\right\}, \tag{2.33}$$

$$E_{\mathrm{w,lu,vw}} = \min\left(\frac{S_{\mathrm{w,lu}}}{\Delta t}, \max\left[0, E_{\mathrm{p}}\left(r_{\mathrm{a,w}}\right) - E_{\mathrm{v,lu,vw}} - E_{\mathrm{t,lu,vw}}\right]\right). \tag{2.34}$$

For the water land-use type and the fraction of open-water ϕ_{ow} in wetlands, evaporation is expressed as

$$E_{\mathrm{w,lu,ow}} = \min\left(\frac{S_{\mathrm{w,lu}}}{\Delta t}, \max\left[0, E_{\mathrm{p}}\left(r_{\mathrm{a,w}}\right)\right]\right). \tag{2.35}$$

The total of an evaporation flux from wetlands (12:WET) or rice paddies (19:RIC) is determined by the weighted sum based on the fractions of vegetation covered soil ϕ_{vs}, vegetation covered water ϕ_{vw}, and open water ϕ_{ow} (see also Table 2.2):

$$E_{j,\mathrm{lu}} = \phi_{\mathrm{lu,vs}} E_{j,\mathrm{lu,vs}} + \phi_{\mathrm{lu,vw}} E_{j,\mathrm{lu,vw}} + \phi_{\mathrm{lu,ow}} E_{\mathrm{w,lu,ow}}, \tag{2.36}$$

where $E_{j,\mathrm{lu}}$ is an evaporation flux ($_j$ denotes $_{\mathrm{v}}$, $_{\mathrm{t}}$, $_{\mathrm{f}}$, $_{\mathrm{sm}}$, or $_{\mathrm{w}}$) of the land-use type $_{\mathrm{lu}}$.

Subsequently, the total of an evaporation flux from a grid cell is determined by the weighted sum of the land-use types:

$$E_j = \sum_{\mathrm{lu}=1}^{\mathrm{lu}=19} \phi_{\mathrm{lu}} E_{j,\mathrm{lu}}, \tag{2.37}$$

where ϕ_{lu} is the land-use occupancy fraction of the land-use type $_{\mathrm{lu}}$.

2.3.3. PHENOLOGY

The growing-season index i_{GS} (Jolly et al., 2005) varies between 0 and 1, and is used to determine the seasonal variations of leaf area i_{LA}. We formulate i_{GS} in STEAM as follows:

$$i_{GS} = f(T_{min})\, f(N)\, f(\theta_{uz}), \tag{2.38}$$

where $f(T_{min})$ is the stress function of minimum temperature, $f(N)$ is the stress function of day length, and $f(\theta_{uz})$ is the stress function of soil moisture. Note that $f(\theta_{uz})$ is a modification of the original expression for i_{GS}, where vapour pressure deficit D_a was used as a proxy for soil moisture (Jolly et al., 2005). However, since soil moisture is calculated in STEAM, it makes sense to use the soil moisture stress function to replace the original vapour pressure stress function. The stress functions are expressed as

$$f(T_{min}) = \begin{cases} 0 & T_{min} \le T_{min,low} \\ \frac{T_{min}-T_{min,low}}{T_{min,high}} - T_{min,low} & T_{min,high} > T_{min} \\ & > T_{min,low}, \\ 1 & T_{min} \ge T_{min,high} \end{cases} \tag{2.39}$$

$$f(N) = \begin{cases} 0 & N \le N_{low} \\ \frac{N-N_{low}}{N_{high}-N_{low}} & N_{high} > N > N_{low}, \\ 1 & N \ge N_{high} \end{cases} \tag{2.40}$$

$$f(\theta_{uz}) = \begin{cases} 0 & \theta_{uz} \le \theta_{uz,wp} \\ \frac{(\theta_{uz}-\theta_{uz,wp})(\theta_{uz,fc}-\theta_{uz,wp}+c_{uz})}{(\theta_{uz,fc}-\theta_{uz,wp})(\theta_{uz}-\theta_{uz,wp}+c_{uz})} & \theta_{uz,wp} < \theta_{uz} \\ & < \theta_{uz,fc}, \\ 1 & \theta_{uz} \ge \theta_{uz,fc}, \end{cases} \tag{2.41}$$

where the lower sub-optimal minimum temperature $T_{min,low}$ is 271.15 K, and the higher $T_{min,high}$ is 278.15 K. The lower sub-optimal threshold day length N_{low} is assumed to be 36 000 s, and the higher N_{high} is 39 600 s (Jolly et al., 2005). T_{min} is taken from the coldest 3 h temperature data of the day. Calculation of day length N follows the approach of Glarner (2006). The soil moisture stress parameter c_{uz} is fixed at 0.07 (Matsumoto et al., 2008). The soil moisture content θ_{uz} is S_{uz}/y_{uz}, where y_{uz} [m] is the depth of the unsaturated root zone. The soil moisture contents at wilting point $\theta_{uz,wp}$ and at field capacity $\theta_{uz,fc}$ depend on soil type. To prevent unrealistically unstable fluctuations in leaf area, the mean $i_{GS,21}$ of the past 21 days is used to scale i_{LA} between the land-use-type-dependent $i_{LA,max}$ and $i_{LA,min}$ (Jolly et al., 2005):

$$i_{LA} = i_{LA,min} + i_{GS,21}\left(i_{LA,max} - i_{LA,min}\right). \tag{2.42}$$

Note that stress function of soil moisture (Eq. 2.41) is reformulated in Chapter 5 and 6 as:

$$f(S_{uz}) = \frac{S_{uz}}{S_R}, \tag{2.43}$$

where S_R is the maximum root zone storage capacity.

2.3.4. STORAGE CAPACITIES

The storage capacity determines the maximum water availability for the evaporation flux in question. We derived vegetation interception storage capacity $S_{\mathrm{v,max}}$ [m] from the monthly i_{LA} based on the storage capacity factor c_{sc} of roughly 0.2 reported by, for example, de Jong and Jetten (2007) and used in van den Hoof et al. (2013):

$$S_{\mathrm{v,max}} = c_{\mathrm{sc}} c_{\mathrm{AR}} i_{\mathrm{LA}}, \tag{2.44}$$

where c_{AR} is the area reduction factor introduced to compensate for rainfall heterogeneity in space and time. The relationship between i_{LA} and vegetation interception storage varies with vegetation type, and a strong relationship has not yet been established. In fact, Breuer et al. (2003) even suggests that no general relationship can be established across vegetation types due to the inherent differences in vegetation structures. Nevertheless, vegetation stock linked to i_{LA} has proven to be useful in many cases where there is a lack of detailed vegetation information.

We assume c_{AR} to be 0.4 for STEAM running with a 3 h time step at the 1.5° scale. Area reduction factors have been developed to establish a relationship between average precipitation and extreme precipitation of a region but can be analogously used to reduce interception storage capacity. In an example diagram obtained from catchment analyses (Shuttleworth, 2012), areas larger than 10 000 km^2 have an area reduction factor up to approximately 0.6. In STEAM, grid cell areas with 1.5° resolution are 10 000 km^2 already at 68° N, and they grow to almost 28 000 km^2 at the Equator. Ideally, c_{AR} should vary with the area considered and rainfall duration, but due to a lack of well-established functions we consider $c_{\mathrm{AR}} = 0.4$ to be acceptable.

The floor interception storage capacity $S_{\mathrm{f,max}}$ [m] is modelled as a function of the leaf area and a certain base value:

$$S_{\mathrm{f,max}} = c_{\mathrm{sc}} c_{\mathrm{AR}} \left[1 + 0.5 \left(i_{\mathrm{LA,max}} + i_{\mathrm{LA,min}}\right)\right]. \tag{2.45}$$

The floor storage capacity increases in areas with vegetation, due to litter formation from fallen leafs. A base value is considered, because wetting of the surface always occurs irrespective of the land cover. However, litter is assumed to have been removed in croplands (i.e. 13:CRP, 15:MOS, 18:IRR, and 19:RIC). Thus, $S_{\mathrm{f,max}}$ [m] for crops corresponds to that of the litter-free floor:

$$S_{\mathrm{f,max,crops}} = c_{\mathrm{sc}} c_{\mathrm{AR}}. \tag{2.46}$$

As a result of the large grid scale (reflected in the area reduction factor), interception storage in STEAM is smaller than normally found in point scale field studies. For example, the vegetation interception storage capacity at the maximum i_{LA} of 5.5 is 0.44 mm, which is about a third of the 1.2 mm reported in a summer temperate forest (Gerrits et al., 2010) and a fraction of the 2.2–8.3 mm per unit of crown projected area in a tropical rainforest site (Herwitz, 1985).

The S_{R} is originally modelled as a function of soil texture and land-use-based rooting depth:

$$S_{\mathrm{R}} = \theta_{\mathrm{fc}} y_{\mathrm{uz}}. \tag{2.47}$$

This is a simplification as many other factors govern root water uptake, including topography (Gao et al., 2013), soil properties, hydraulic redistribution of soil water by roots (Lee et al., 2005), groundwater table (Miguez-Macho and Fan, 2012), and climate (Feddes et al., 2001). In addition, variations of rooting distribution (e.g. Jackson et al., 1996) and the existence of deep roots (e.g. Canadell et al., 1996; Kleidon and Heimann, 2000) may conflict with the assumption of uniform rooting depth within a land-use type. In Chapter 5 and 6, S_R is instead directly derived from observation-based precipitation and evaporation, see also Sect. 2.3.6.

2.3.5. IRRIGATION

STEAM includes irrigation because it has been shown to constitute an important moisture source to the atmosphere (e.g. Gordon et al., 2005; Lo and Famiglietti, 2013; Tuinenburg, 2013; Wei et al., 2012). Irrigation water supplied is assumed to meet the irrigation requirement and is not restricted by water availability. Net irrigation enters the unsaturated zone and is estimated as a function of soil moisture. In rice paddies (19:RIC), irrigation water simply upholds a 10 cm water level. For non-rice crops (18:IRR), irrigation requirement I_{req} is the amount of water needed to reach field capacity in the unsaturated root zone:

$$I_{req} = \max\left[0, \frac{y_{uz}\left(\theta_{uz,fc} - \theta_{uz}\right)}{\Delta t} - \frac{S_{uz,lu}}{\Delta t}\right]. \tag{2.48}$$

However, because a certain amount of irrigation water applied is always lost due to inefficiencies in the system, an irrigation efficiency should be applied in order to correctly estimate runoff and water withdrawal. In STEAM, we assume the gross irrigation I_g to be twice the I_{req}. Although irrigation efficiency in practice varies greatly with irrigation technique, crop type, and country (Rohwer et al., 2007), we consider our simplification acceptable since the gross irrigation assumption affects evaporation (our major concern) less than, e.g. runoff and water withdrawal. Of gross irrigation applied to irrigated non-rice crops (18:IRR), 15 % is directed to the vegetation interception stock S_v and 85 % to the floor interception stock S_f. Of the gross irrigation applied to rice paddies (19:RIC), 5 % is directed to vegetation interception stock S_v, 5 % to the floor interception stock S_f (assuming inter-paddy pathways), and 90 % to the water stock S_w.

2.3.6. LAND-USE PARAMETRISATION

The parameters used to describe land cover or land use (hereafter 'land use') include maximum and minimum leaf area index $i_{LA,max}$ and $i_{LA,min}$, maximum and minimum plant height h_{max} and h_{min}, depth of the unsaturated zone (or rather active rooting depth) y_{uz}, albedo α, minimum stomatal resistance $r_{s,st,min}$, and floor roughness $z_{0,f}$. Land-use parameters considered include those used in other large-scale land-surface or hydrological models (Federer et al., 1996; van den Hurk et al., 2000; van den Hurk, 2003; Zhou et al., 2006; Bastiaanssen et al., 2012) and studies of specific land-use properties (Scurlock et al., 2001; Zeng, 2001; Breuer et al., 2003; Kleidon, 2004). The range of parameters in the literature can sometimes be significant and contradictory, due to discrepancies in scale, parameter definitions, and methods of parameter estimation. The choice of land-use parameters is therefore not simply taken as a mean from the

literature values investigated but is rather based on the preservation of the internal consistency of STEAM, manual calibration, and priority for literature values with higher relevance. In addition, some land-use types are assumed to contain water, either as water below vegetation or as open water. The land-use parameters used in the model are shown in Table 2.1, and the parametrisation of water fractions are presented in Table 2.2. Slight modifications to the land-use parameters were made in Chapter 6, see details in Supplementary Information in Wang-Erlandsson et al. (2017).

In Chapter 5 and 6, S_R is used directly and y_{uz} is not needed. In Chapter 5, S_R is estimated from satellite-based data as described there. In Chapter 6, the root zone storage capacity map is based on the best performing Gumbel normalised root zone storage capacity ($S_{R,CRU-SM,merged}$) from Chapter 5. Root zone storage capacity for both current and potential land-cover and land-use scenarios were constructed from the mean S_R of a combined land use and Köppen-Geiger climate class (Kottek et al., 2006). The mean S_R of single land-use types was used only in places where the combination of land use and climate zone that exists in the potential land-cover scenario did not exist in the current land-use map.

In Chapter 4 and 5, each land use ($_{lu}$) is simulated for the whole world ('mosaic'), and the total terrestrial evaporation (E) is obtained by weighting each land use's evaporation (E_{lu}) by its fractional spatial occupation (ϕ_{lu}): $E = \Sigma E_{lu}\phi_{lu}$. In Chapter 6, we instead weight each land use specific parameter (Π_{lu}) with the land-use fractional occupation within each group of land-use. This merged land-use parametrisation map (Π) is then used to simulate total evaporation ('tile'): $E(\Pi) = E(\Sigma\Pi_{lu}\phi_{lu})$, see Fig. 2.3.

2.4. DATA

2.4.1. METEOROLOGICAL INPUT

Meteorological data were in principal all taken from ERA-I (European Reanalysis Interim), produced by the European Centre for Medium-range Weather Forecasts (ECMWF) (Dee et al., 2011). In the original STEAM set-up (Chapter 4), STEAM is forced by ERA-I precipitation, snowfall, snowmelt, temperature at 2 m height, dew point temperature at 2 m height, wind speed in meridional and zonal directions at 10 m height, incoming shortwave radiation, and net longwave radiation. Sub-daily evaporation was additionally used to downscale daily potential evaporation. Chapter 6 replaces ERA-I precipitation with the state-of-the-art precipitation product Multi-Source Weighted-Ensemble Precipitation (MSWEP) (Beck et al., 2017) that was specifically created for hydrological modelling. All meteorological forcings are given at 3 h and 1.5° latitude ×1.5° longitude resolution. The data used cover latitudes from 57° S to 79.5° N.

2.4.2. LAND-SURFACE DATA

The monthly varying land-surface map used in STEAM consists of 19 land-use types; see Table 2.1. The first 17 International Geosphere–Biosphere Programme (IGBP) land-use types are based on the Land Cover Type Climate Modeling Grid (CMG) MCD12C1 created from Terra and Aqua Moderate-resolution Imaging Spectroradiometer (MODIS) data (Friedl et al., 2010) for the year 2001. The two irrigated land-use classes are based on the data set of Monthly Irrigated and Rainfed Crop Areas around the year 2000 (MIRCA2000)

Table 2.1: Land-use parameters used in STEAM.

Land-use class	$i_{\mathrm{LA,max}}$	$i_{\mathrm{LA,min}}$	y_{uz}	α	h_{max}	h_{min}	$z_{0,\mathrm{f}}$	$r_{\mathrm{s,st,min}}$
Unit	–	–	m	–	m	m	m	$\mathrm{s\,m^{-1}}$ [a]
01:WAT (Water)	0	0	0	0.08	0	0	0.00137	0
02:ENF (Evergreen needleleaf forest)	5.5	2	2	0.15	17	17	0.02	300
03:EBF (Evergreen broadleaf forest)	5.5	2	2	0.18	30	30	0.02	200
04:DNF (Deciduous needleleaf forest)	5	1	2	0.18	17	17	0.02	300
05:DBF (Deciduous broadleaf forest)	5.5	1	2	0.18	25	25	0.02	200
06:MXF (Mixed forest)	5	1	2	0.18	20	20	0.02	250
07:CSH (Closed shrubland)	1.5	0.5	2	0.2	1.5	1.5	0.02	200
08:OSH (Open shrubland)	1.5	0.5	2	0.2	1	1	0.02	200
09:WSA (Woody savannah)	2	0.5	2	0.2	0.8	0.8	0.02	150
10:SAV (Savannah)	2	0.5	3.5	0.2	0.8	0.1	0.02	150
11:GRA (Grassland)	2	0.5	1.5	0.2	0.8	0.05	0.01	150
12:WET (Permanent wetland)	4	1	1.5	0.15	1	0.05	0.01	150
13:CRP (Cropland, rainfed)	3.5	0.5	1.5	0.2	0.8	0.05	0.005	150
14:URB (Urban and built-up)	1	0.1	0.5	0.18	0.8	0	0.001	250
15:MOS (Crop/natural mosaic)	3.5	0.5	1.5	0.2	0.8	0.1	0.005	150
16:ICE (Snow/ice)	0	0	0	0.7	0	0	0.001	0
17:BAR (Barren land)	0.1	0.01	1.5	0.25	0.8	0	0.001	200
18:IRR (Irrigated crop, excl. rice)	3.5	3.5	0.5	0.2	0.8	0.8	0.005	150
19:RIC (Irrigated rice paddies)	3.5	3.5	0.5	0.2	0.8	0.8	0.005	150

[a] The unit for $r_{\mathrm{s,st,min}}$ is $\mathrm{d\,m^{-1}}$ throughout this thesis; it is only given as $\mathrm{s\,m^{-1}}$ in this table to facilitate comparison with other studies.

Table 2.2: Fractions of vegetation in soil ϕ_{vs}, vegetation in water ϕ_{vw}, and open water ϕ_{ow} by land-use type. Related equations are described in Sect. 2.3.2.

Land-use type	ϕ_{vs}	ϕ_{vw}	ϕ_{ow}
12:WET	1/3	1/3	1/3
19:RIC	1/10	9/10	0
01:WAT	0	0	1
Other	1	0	0

V1.1. (Portmann et al., 2010). The resolution for MODIS is 0.05° and for MIRCA2000 5′. To create the joint map, monthly irrigated land from MIRCA2000 was taken to replace primarily MODIS cropland fraction (13:CRP) and secondarily MODIS cropland / natural mosaic fraction (15:MOS). The joint map has a total land area of 133 146 465 km^2 and includes inland waters except big lakes.

In Chapter 6, the land-use and land-cover data input to STEAM are primarily based on the potential land-cover from Ramankutty and Foley (1999) and current land-use scenarios from Ramankutty et al. (2008) for consistency. Permanent wetlands, permanent snow or ice, and urban or built-up areas were taken from MODIS for the year 2005. Monthly irrigated rice and irrigation non-rice crops were obtained from MIRCA2000. In this merging procedure, MODIS is allowed to override the Ramankutty datasets, and MIRCA2000 is allowed to override the Ramankutty map as long as it does not extend over the cropland areas.

Soil texture data have been taken from the Harmonized World Soil Database (HWSD) (FAO/IIASA/ISRIC/ISSCAS/JRC, 2012), and we assigned volumetric soil moisture content at saturation, field capacity, and wilting point based on the United States Department of Agriculture (USDA) soil classification (Saxton and Rawls, 2006). Topsoil saturation, subsoil field capacity, and subsoil wilting point have been assigned to the original 30″ resolution and scaled up to 1.5° by area weighting.

2.5. OVERVIEW OF THE DIFFERENT STEAM SET-UPS

As noticed, the STEAM settings in terms of process representation, data input, and parametrisation vary somewhat between the different chapters. Chapter 4 used the original settings of STEAM, Chapter 5 improved the S_R input, and Chapter 6 made use of the improvements of S_R and simplified certain processes in STEAM to gain computational efficiency in coupling STEAM with WAM-2layers. An overview of these different settings are given in Table 2.3.

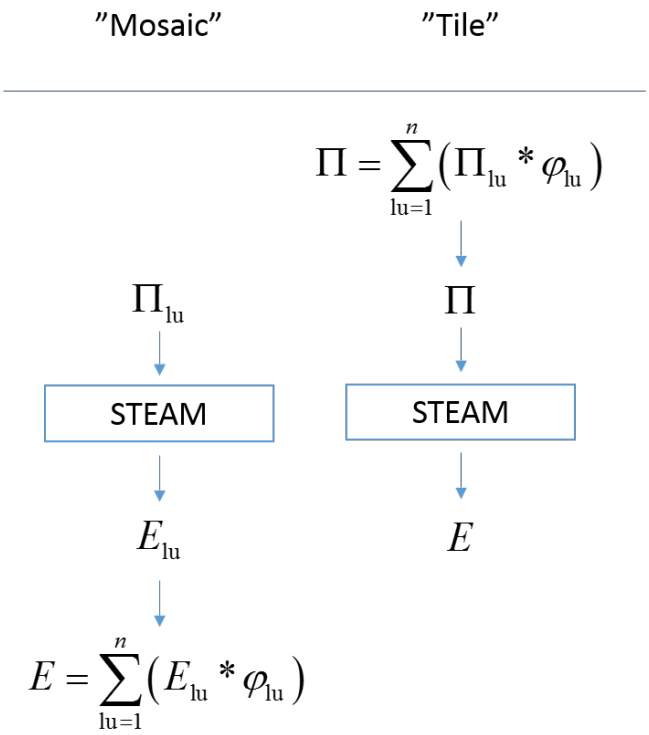

Figure 2.3: Parametrisation procedures in STEAM based on the 'mosaic' and 'tile' approach respectively.

Table 2.3: STEAM settings in different chapters of this thesis.

	Chapter 4	Chapter 5	Chapter 6	See also
Land precipitation	ERA-I	ERA-I	MSWEP	Sect. 2.4.1
Main LU map	MODIS	MODIS	Ramankutty	Sect. 2.4.2
S_R source	Look-up table	Satellite	Satellite, grouped	Sect. 2.3.6
Parametrisation approach	Mosaic	Mosaic	Tile	Sect. 2.3.6
Land-use parametrisation	Table 2.1	Table 2.1	SI in (Wang-Erlandsson et al., 2017)	Sect. 2.3.6
Snowfall	ERA-I	ERA-I	Temperature threshold 0°C	-

3

EVALUATION OF STEAM

The world turns softly
Not to spill its lakes and rivers,
The water is held in its arms
And the sky is held in the water.

Hilda Conkling (1910-1986)

This chapter compares model output from the Simple Terrestrial Evaporation to Atmosphere Model (STEAM) with independent data and studies of evaporation, evaporation partitioning, runoff, and irrigation. Despite a relatively simple model structure, validation shows that STEAM produces realistic evaporative partitioning and hydrological fluxes that compare well with other global estimates over different locations, seasons and land-use types.

This chapter is based on:

Wang-Erlandsson, L., van der Ent, R. J., Gordon, L. J., and Savenije, H. H. G.: *Contrasting roles of interception and transpiration in the hydrological cycle — Part 1: Temporal characteristics over land*, Earth System Dynamics, 5, 441–469, 2014.

Wang-Erlandsson, L., Fetzer, I., Keys, P., van der Ent, R. J., Savenije, H. H. G. and Gordon, L. J.: *Remote land-use impacts on river flows through atmospheric teleconnections*, Hydrology and Earth System Science Discussions, in review.

3.1. INTRODUCTION

Simple Terrestrial Evaporation to Atmosphere Model (STEAM) is here evaluated with respect to evaporation, evaporation partitioning, runoff, and irrigation. STEAM has been used in different contexts with different set-ups, see Sect. 2.5. Most of the evaluation presented in this chapter used the STEAM default 'Chapter 4' settings. Because river flows are in focus in Chapter 6, the 'Chapter 6'-settings are also re-evaluated here with regard to runoff. Finally, we investigate the sensitivity of model results to precipitation forcing.

3.2. METHODS

The model evaluation comprises the following: total and land-use-based evaporation, total and land-use-based evaporation partitioning, runoff, irrigation, and irrigation evaporation contribution. Total global fluxes are calculated based on a land area of 133 146 465 km^2 (including Greenland and excluding Antarctica). Land-use evaporation is obtained from Eq. (2.36). Irrigation evaporation contribution was calculated based on the difference in evaporation between STEAM simulations with and without the irrigation routine turned on. Mean annual runoff from STEAM is estimated as the difference between mean annual precipitation and evaporation.

3.3. DATA FOR VALIDATION AND COMPARISON

For evaporation evaluation, we used the LandFlux-EVAL evaporation benchmark products (Mueller et al., 2013) for the years 1989–2005. This data product consists of a merged synthesis from five satellite or observation-based data sets, five land-surface model simulations, and four reanalysis data sets.

For runoff evaluation, composite and model runoff fields from the Global Runoff Data Centre (GRDC) were used (Fekete et al., 2000). The model runoff fields are the simulations of the GRDC Water Balance Model ($GRDC_{WBM}$), whereas the composite runoff fields ($GRDC_{Comp}$) are the model runoff corrected by observed inter-station discharge (Fekete et al., 2000). The river basin map is based on the global 30 min drainage direction map of Döll and Lehner (2002). Precipitation data used to estimate STEAM runoff from STEAM evaporation are taken from ERA-Interim (Dee et al., 2011) and Multi-Source Weighted-Ensemble Precipitation (MSWEP) (Beck et al., 2017).

3.4. EVALUATION RESULTS

3.4.1. EVAPORATION

STEAM estimates global annual terrestrial evaporation as 555 mm $year^{-1}$ (i.e., 73 900 km^3 $year^{-1}$); spatial distribution is shown in Fig. 3.1. This is comparable to current global evaporation data sets. In the Water Model Intercomparison Project (WaterMIP), the range of evaporation given by 11 models was 415–585 mm $year^{-1}$ for the period 1985–1999 forced with WATCH (Water and Global Change) meteorological data (Haddeland et al., 2011). By subtracting global runoff from precipitation products for the years 1984–2007, Vinukollu et al. (2011) arrived at global evaporation rates of 488–558 mm $year^{-1}$ (i.e. 64 000–73 000 km^3 $year^{-1}$). In the LandFlux-EVAL multi-data-set synthesis, the global mean evaporation was 493 mm $year^{-1}$ as given by a combination of land-surface model

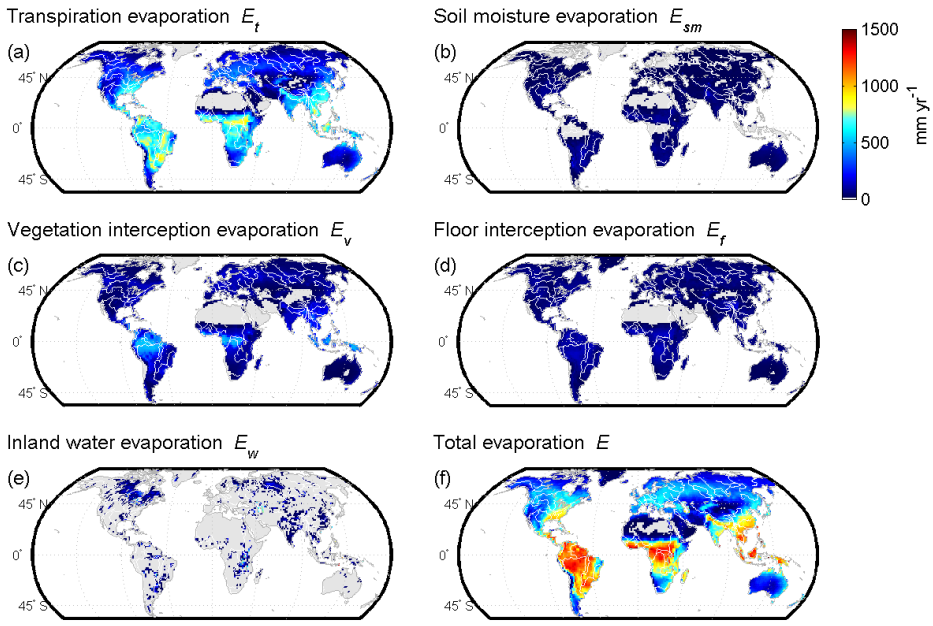

Figure 3.1: Mean annual evaporation as estimated by STEAM (1999–2008). Grey indicates areas where the evaporative flux is 0. Results are discussed in Sects. 3.4.1 and 3.4.2.

simulations, observational data set, and reanalysis data for both the period of 1989–1995 and 1989–2005 (Mueller et al., 2013).

Figure 3.2 shows how STEAM evaporation compares to the LandFlux-EVAL product for 1989–2005. STEAM evaporation is within the interquartile range of all LandFlux-EVAL products in the tropics, the United States, parts of Europe, south Asia, northern Russia, and large parts of Africa south of the Sahel. The upper quartile is mostly exceeded in the boreal forests in the northern latitudes, China, Argentina, and the Sahel. Most exceedance of STEAM evaporation is in comparison with the land-surface models, and the least with the reanalyses data included in the LandFlux-EVAL product. Only a few limited patches in northern Canada, Sudan, Argentina, and northern China exceed the LandFlux-EVAL maximum. Seasonally, Fig. 3.3 shows that Northern Hemisphere spring and summer are generally more in range compared to winter and autumn, when STEAM tends to have higher evaporation rates in the northernmost latitudes compared to LandFlux-EVAL. However, LandFlux-EVAL excluded some high evaporation values in the northern latitudes based on physical constraints (Mueller et al., 2013), which consequently eliminates potentially important wintertime interception (Schlaepfer et al., 2014).

Evaporation contributions per land-use type are listed in Table 3.1 and compared to the other studies in Table 3.2. The highest evaporation rates are found in irrigated

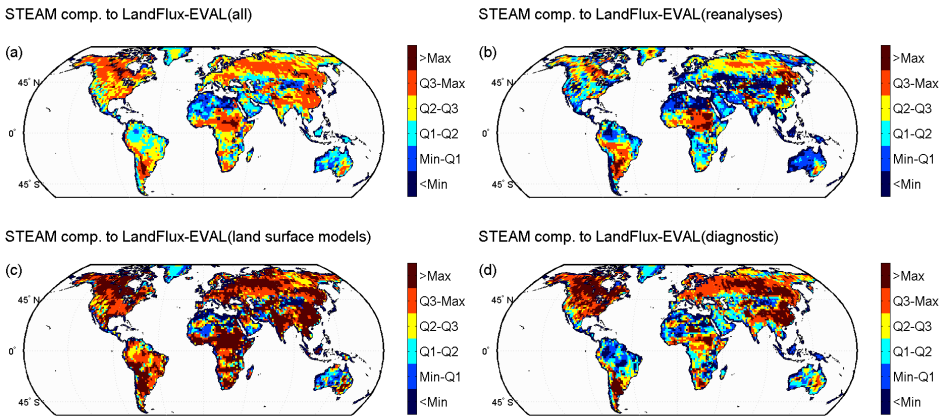

Figure 3.2: Annual mean STEAM evaporation compared to the statistics (minimum, first quartile, median, third quartile, maximum) of the LandFlux-EVAL product (1989–2005) for **(a)** merged synthesis, **(b)** reanalyses, **(c)** land-surface models, and **(d)** diagnostic data sets. Results are discussed in Sect. 3.4.1.

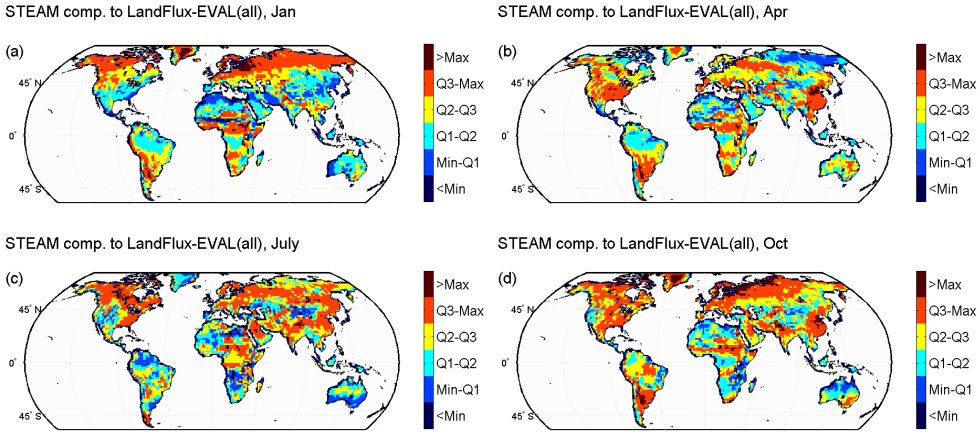

Figure 3.3: Monthly mean STEAM evaporation compared to the statistics (minimum, first quartile, median, third quartile, maximum) of the merged synthesis LandFlux-EVAL product (1989–2005) for **(a)** January, **(b)** April, **(c)** July, and **(d)** October. Results are discussed in Sect. 3.4.1.

lands, evergreen broadleaf forests, and open waters. This is followed by wetlands, savannahs, deciduous broadleaf forests, natural mosaics, woody savannahs, mixed forests, and rainfed croplands. Evaporation rates in the lower tier include contributions from needleleaf forests, grasslands, and shrublands. In general, STEAM evaporation is

comparable to the estimates of Gordon et al. (2005), the compilation results of Schlesinger and Jasechko (2014) (based on Mu et al., 2011), and the field data from Rockström et al. (1999). The mixed forest evaporation estimate in STEAM is double that of Gordon et al. (2005), but the area is also very different, suggesting substantial differences in forest definition. Closed shrublands in STEAM also produces higher evaporation rates, but, because the numbers are for shrublands in general and not closed shrublands in particular, the shrublands comparison is inevitably inconclusive. Some caution is warranted in comparing evaporation rates across studies. Nevertheless, this comparison shows that evaporation estimates in STEAM are within the range of previous estimates.

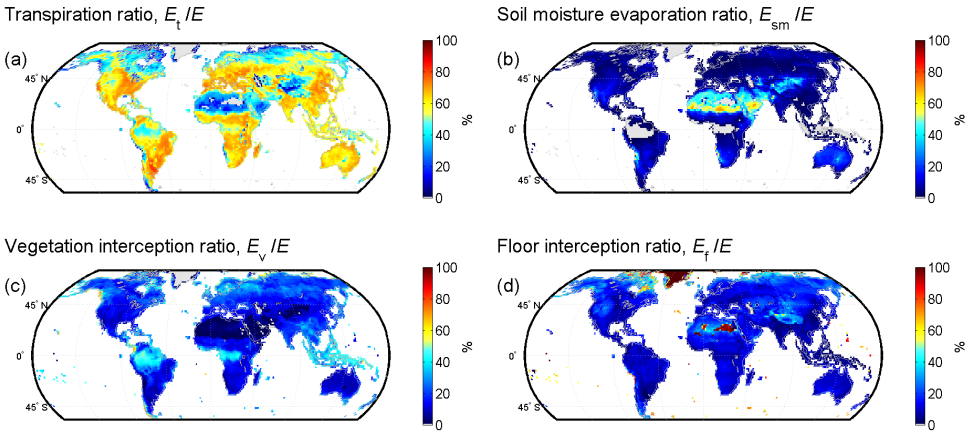

Figure 3.4: Partitioned evaporation fluxes expressed as a percentage of total mean annual evaporation (1999–2008). Grey indicates areas where evaporation percentage is 0. Results are discussed in Sect. 3.4.2.

3.4.2. EVAPORATION PARTITIONING

In STEAM, the dominating evaporation flux is transpiration E_t (59 %), followed by vegetation interception E_v (21 %), floor interception E_f (10 %), soil moisture evaporation E_{sm} (6 %), and lastly open-water evaporation E_w (4 %). The global distribution of the annual mean evaporation fluxes is shown in Figs. 3.1 and 3.4 (as percentage of total evaporation). Seasonal variations of evaporation fluxes are shown over latitudes in Fig. 3.5. It is shown that transpiration dominates in the densely vegetated areas in the tropics. In addition, transpiration rates increase over the boreal forests during the Northern Hemisphere summer.

Table 3.3 provides an overview of evaporative partitioning values in the literature and in STEAM. We note that the STEAM global mean transpiration ratio is in good agreement with the literature compilation results presented by Schlesinger and Jasechko (2014) and the Lund-Potsdam-Jena (LPJ) model estimate by Gerten et al. (2005), but higher than other land-surface model simulations (Alton et al., 2009; Lawrence et al., 2007; Choudhury

Table 3.1: Evaporation and evaporation partitioning by land-use type, 1999–2008. Symbols are explained in Notations. Results are discussed in Sects. 3.4.1 and 3.4.2.

Land use	Area	P	E	E_v	E_f	E_t	E_{sm}	E_w	E_v	E_f	E_t	E_{sm}	E_w	E_v
Unit	1000 km^2	mm year^{-1}							% of E					% of P
01:WAT	1071	937	1147	0	0	0	0	1147	0	0	0	0	100	0
02:ENF	3224	853	496	155	73	248	20	0	31	15	50	4	0	18
03:EBF	13 541	2542	1208	452	92	652	13	0	37	8	54	1	0	18
04:DNF	1341	481	366	95	67	191	14	0	26	18	52	4	0	20
05:DBF	1350	1057	853	179	83	543	48	0	21	10	64	6	0	17
06:MXF	9349	958	604	158	80	345	21	0	26	13	57	4	0	16
07:CSH	99	554	499	54	57	324	64	0	11	11	65	13	0	10
08:OSH	21 207	432	281	38	44	162	37	0	14	16	58	13	0	9
09:WSA	10 585	1210	735	103	89	495	48	0	14	12	67	6	0	9
10:SAV	9904	1122	861	102	91	602	66	0	12	11	70	8	0	9
11:GRA	18 253	616	394	54	66	241	33	0	14	17	61	8	0	9
12:WET	1218	1151	957	114	26	297	8	513	12	3	31	1	54	10
13:CRP	(10 352–10 851)*	789	577	99	23	417	38	0	17	4	72	7	0	13
14:URB	454	991	465	46	42	256	120	0	10	9	55	26	0	5
15:MOS	(7790–7814)*	1262	779	165	79	509	25	0	21	10	65	3	0	13
16:ICE	2710	560	32	0	32	0	0	0	0	100	0	0	0	0
17:BAR	18 943	90	57	1	11	20	25	0	1	19	36	44	0	1
18:IRR	(1060–1195)*	727	1375	271	81	910	113	0	20	6	66	8	0	37
19:RIC	(175–570)*	1453	1458	242	7	547	4	659	17	0	37	0	45	17
Global	133 146	888	555	115	58	326	33	24	21	10	59	6	4	13

* Area varies because a monthly varying irrigation map is applied.

Table 3.2: Evaporation of lumped land-use types in comparison with other studies. Results are discussed in Sect. 3.4.1.

	STEAM, year 1999–2008		Gordon et al. (2005)		Schlesinger and Jasechko (2014) based on Mu et al. (2011)	Rockström et al. (1999)
	Area	Average E	Area	Average E	Average E	Average E
Unit	1000 km^2	[mm year^{-1}]	1000 km^2	[mm year^{-1}]	[mm year^{-1}]	[mm year^{-1}]
Forest[a]	28 805	875	46 665	660		
Evergreen needleleaf	3224	496	2134	510	458[e]	487[i]
Evergreen broadleaf	13 541	1208	16 278	1146	1076	1245
Deciduous needleleaf	1341	366		293–795[d]	458[e]	
Deciduous broadleaf	1350	853		293–795[d]	549[f]	729–792[d]
Mixed	9349	604	14 222	313		
Savannah	20 489	735–861[b]	19 562	556		416[j]/882/1267[k]
Shrubland	21 306	281–499[c]	18 649	227	302[g]	270[l]
Grassland	18 253	393	14 393	258	332–583[h]	410[m]

[a] Includes all forest types. [b] Woody savannah (09:WSA) and savannah (10:SAV). [c] Closed shrubland (07:CSH) and open shrubland (08:OSH). [d] Deciduous forests in general. [e] Temperate coniferous forest. [f] Temperate deciduous forest. [g] Mediterranean shrubland. [h] Temperate and tropical grassland. [i] Coniferous forest in general. [j] Woody savannah. [k] Wet savannah. [l] Dry shrubland. [m] Cool grassland.

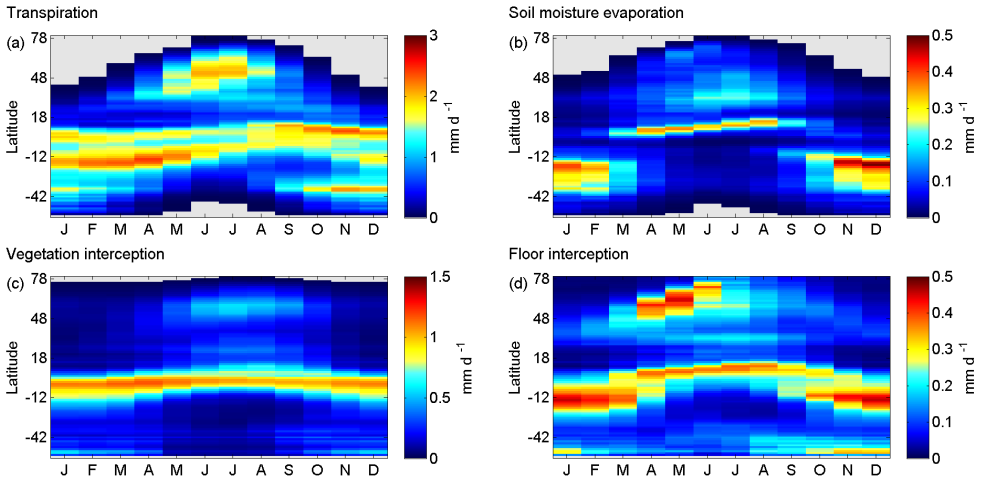

Figure 3.5: Mean monthly evaporation as estimated by STEAM for different latitudes (1999–2008). Note that the scales are different for the different evaporation fluxes. Grey indicates where the evaporative flux is near 0. Results are discussed in Sect. 3.4.2.

et al., 1998; Dirmeyer et al., 2006). Jasechko et al. (2013, 2014) estimated the transpiration ratio to be 80–90 % using a combination of isotope measurement techniques and satellite observations at river basin and global scales. However, their results have been challenged by Coenders-Gerrits et al. (2014), who showed that the transpiration ratio reduces to 35–80 % by using other input data; Schlesinger and Jasechko (2014), who estimated the global transpiration ratio to be 61 % based on literature data compilation; and by Schlaepfer et al. (2014), who argued that the underlying assumption of Jasechko et al. (2013) that isotope ratios of a lake would be representative for the entire catchment is flawed. A number of possible explanations for the high transpiration ratio bias in isotope studies is also offered by Sutanto et al. (2014).

Table 3.1 shows the annual average evaporation fluxes as a percentage of total evaporation per land-use class. Transpiration is the dominant evaporation flux in almost all land-use types: 50–64 % in forests, 61 % in grasslands, 72 % in croplands, and 58–65 % in shrublands. The exceptions are, logically, barren lands (17:BAR), snow/ice (16:ICE), and open waters (01:WAT).

Among the more vegetated land-use types, vegetation interception ratios are highest in forests (21–37 % of E), followed by croplands (17 %), and lowest in the sparsely vegetated land-use types: shrublands, savannahs, grasslands, wetlands, and urban lands (10–14 %). Floor interception values follow the pattern of vegetation interception. Thus, floor interception is generally higher than soil moisture evaporation in forests, whereas soil moisture evaporation equals or exceeds floor interception more often in shrublands and croplands.

Reported land-use specific evaporative partitioning in previous research is scarce at the global scale. Lawrence et al. (2007) do not report evaporative partitioning by land use (from simulation using Community Land Model version 3, CLM3), but map

Table 3.3: Overview of global evaporative partitioning estimates. Results are discussed in Sect. 3.4.2.

Unit	E_t	E_v	(E_f, E_{sm})	Source
	% of E			
Land-surface models				
STEAM	59	21	16	This study
JULES (with SiB or SPA scheme)	38–48			Alton et al. (2009)
CLM3	44	17	39	Lawrence et al. (2007)
LPJ	65			Gerten et al. (2005)
A biophysical process-based model	52	20	28	Choudhury et al. (1998)
Other methods				
Literature	61			Schlesinger and Jasechko (2014)
Literature	57			Wei et al. (2017)
Isotope + literature	35–80			Coenders-Gerrits et al. (2014)
Isotope + literature	80–90			Jasechko et al. (2013)
GLEAM, satellite-based method	80	11	7	Miralles et al. (2011)
Multimodel, GSWP2	48	16	36	Dirmeyer et al. (2006)

figures indicate that their soil evaporation is higher and canopy interception is lower in savannah, grassland, and shrubland compared to STEAM. Transpiration ratios of CLM3 are comparable with STEAM in forested and savannah areas but are much lower (down to < 30 %) in the western US, India, southeastern China, and South Africa. Alton et al. (2009) report global mean transpiration ratios of 49–65 % in forests, 32–60 % in grassland, and 44–51 % in shrublands. The order of magnitude is similar to STEAM, but transpiration ratios for shrublands are lower. Schlesinger and Jasechko (2014) compiled satellite-based estimates from Mu et al. (2011) and arrived at 70 % transpiration in tropical forests, 55–67 % in other forests, and 57–62 % in grasslands. Choudhury et al. (1998) used a biophysical process-based model and estimated the transpiration ratio to amount to 56–77 % in three rainforest regions, 63–82 % in three savannah regions, and 37–82 % in seven cropland areas. Transpiration for river basins shown in the isotope study of Jasechko et al. (2013) shows transpiration ratios above 70 % in grassland dominated areas in the western United States. Van den Hoof (2013) evaluated model performance against sites in temperate Europe and reported transpiration rates of 47–78 % at eight forest sites and 59–79 % at three grassland sites. A recent upscaling of site-scale measurements (Wei et al., 2017) suggests transpiration to account for about 57 % of global land evaporation. Overall, STEAM falls well in the range of the reported evaporation partitioning ratios.

STEAM estimates the vegetation interception ratio as 18 % of rainfall in evergreen broadleaf forest, 17 % in deciduous broadleaf forest, and 18–20 % in needleleaf forest. In

comparison, Miralles et al. (2010) arrived at higher canopy interception in coniferous (22 %) and deciduous forest (19 %) than in tropical forest (13 %) using satellite data analysis and literature review. Thus, interception ratios are comparable, except for tropical forest. In an interception scheme comparison study, Wang et al. (2007) found that taking rainfall type into account increased the performance and decreased interception in the tropics in comparison to the default CLM3 interception scheme. Although STEAM uses an area reduction factor to scale interception, this may simply not be enough in the tropical, convective rainfall regimes. On the other hand, field studies have shown high interception ratios in the tropics. For example, Cuartas et al. (2007) reported 16.5 % for 2 years in the central Amazon, Franken et al. (1992) reported 19.8 % in the central Amazon, and Tobón Marin et al. (2000) reported 12–17 % in the Colombian Amazon over 4 years. Interestingly, Cuartas et al. (2007) also showed that the differences in dry and normal years can differ substantially: 13.3 % in a normal year and 22.6 % in a dry year.

3.4.3. RUNOFF

STEAM estimates the mean annual global runoff as 43 216 $km^3\,year^{-1}$ (325 $mm\,year^{-1}$, 37 % of $\overline{P}$) based on ERA-I precipitation forcing and 'Chapter 4'-settings, and 39 253 $km^3\,year^{-1}$ based on MSWEP precipitation and the 'Chapter 6'-settings (see Sect. 2.5). Based on discharge data and simulated stream flow simulations, Dai and Trenberth (2002) estimated runoff to be 37 288 $\pm$ 662 $km^3\ year^{-1}$ (35 % of $\overline{P}$, excluding Greenland and Antarctica). Syed et al. (2010) arrived at 36 055 $km^3\,year^{-1}$ based on the global ocean mass balance, Oki and Kanae (2006) reported 45 500 $km^3\,year^{-1}$ including groundwater runoff, and the GRDC composite runoff ($GRDC_{Comp}$) is about 38 000 $km^3\,year^{-1}$ (Fekete et al., 2000). Thus, the STEAM runoff estimate is well within the literature range, with the major uncertainty being associated with the precipitation forcing data.

STEAM runoff was further compared to $GRDC_{Comp}$, $GRDC_{WBM}$ runoff data in 19 major river basins of the world (Fig. 3.6). The standard deviations (σ) shown in Fig. 3.6 are derived based on the differences between the multiyear mean runoffs in $GRDC_{Comp}$ (which we here consider as the benchmark runoff) and the other runoffs ($GRDC_{WBM}$ and STEAM with various settings) Among the compared data sets, STEAM runoff that was derived with the combination of ERA-I precipitation and 'Chapter 6'-settings (Sect. 2.5) deviates the most from $GRDC_{Comp}$, and the least with the combination of MSWEP precipitation and 'Chapter 6'-settings. The considerable differences in σ between using different precipitation datasets for deriving runoff further demonstrates the high sensitivity of runoff to precipitation. The role of precipitation input is especially clear in the Congo, Yangtze, Mekong, and Brahmaputra basins (Fig. 3.6).

3.4.4. IRRIGATION

The simulated mean gross irrigation is 1970 $km^3\,year^{-1}$, and the simulated mean increase in evaporation from irrigation is 1134 $km^3\,year^{-1}$. The irrigation hotspots in especially India, south-eastern China, and the central US coincide well with where evaporation is enhanced by irrigation input. Our estimates are comparable to previous estimates. Gross irrigation was estimated at 2500 $km^3\,year^{-1}$ by Döll and Siebert (2002), at 2353 $km^3\,year^{-1}$ by Seckler et al. (1998), and at 1660 $km^3\,year^{-1}$ by Rost et al. (2008). The latter study did,

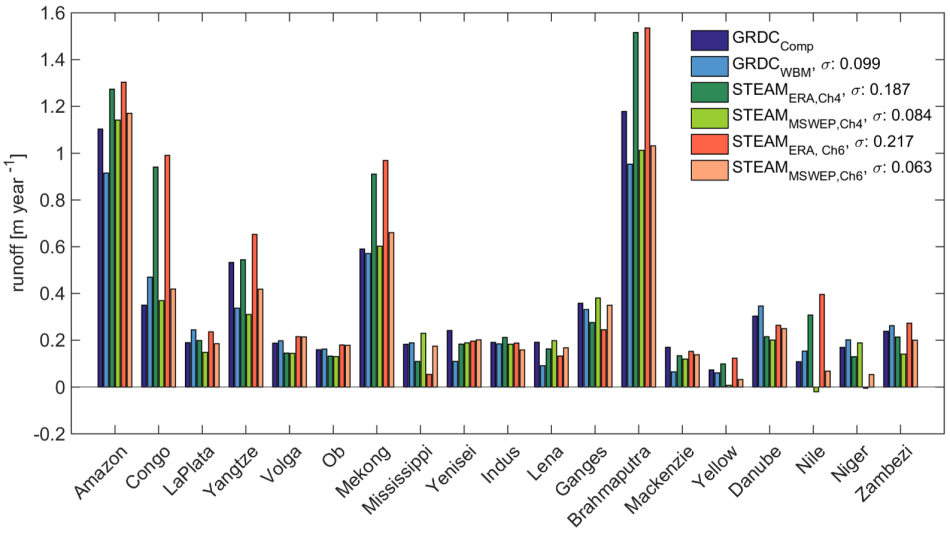

Figure 3.6: Mean annual runoff of STEAM compared to GRDC-Comp (Global Runoff Data Centre composite runoff fields) and the GRDC-WBM (Water Balance Model) runoff corrected using inter-station discharge data. STEAM runoff is derived from the difference between a precipitation dataset (ERA-I or MSWEP), and STEAM evaporation (as used in Chapter 4 or 6). In Chapter 4, STEAM is forced with ERA-I precipitation, and root zone storage capacity is taken from land-use based look-up table. In Chapter 6, STEAM is forced with MSWEP precipitation and root zone storage capacity is based on both climate and land-use. STEAM runoff are for the years 2000–2009, whereas GRDC-Comp and GRDC-WBM represent long-term runoff.

however, not take into account recharge to the groundwater. Evaporation contribution by irrigation was simulated at 1100 km^3 year^{-1} by Döll and Siebert (2002). While higher evaporation contributions have also been reported in the literature, such as 2600 km^3 year^{-1} by Gordon et al. (2005), they could possibly be explained by differences in methods and irrigation maps. Given the uncertainties, the modelling results are considered acceptable in terms of total amounts.

3.4.5. SENSITIVITY TO PRECIPITATION

We perform a sensitivity check against precipitation because STEAM is forced by ERA-I precipitation reanalyses data, which is higher than several other satellite- and/or gauge-based precipitation data sets. For the period 1999–2008, the mean global ERA-I precipitation is 118 236 km^3 year^{-1} for a land area of 133 146 465 km^2. Other reported terrestrial precipitation values include 111 000 km^3 year^{-1} (Oki and Kanae, 2006), 109 500 km^3 year^{-1} from Climatic Research Unit (CRU), 111 200 km^3 year^{-1} from Precipitation Reconstruction over Land (PREC/L), and 112 600 km^3 year^{-1} from Global Precipitation Climatology Project (GPCP) (Trenberth et al., 2007).

Table 3.4 provides an overview of the sensitivity of runoff and evaporation fluxes to a uniform 5 % reduction in precipitation. A number of observations can be noted.

First, the mean annual STEAM runoff is clearly more sensitive (−10.95 %) to precipitation reduction compared to evaporation (−1.78 %). Second, among the evaporation fluxes, soil moisture evaporation (−2.95 %) and transpiration (−2.32 %) respond most strongly, whereas the vegetation (−0.89 %) and floor interception (−0.65 %) evaporation fluxes reduce only marginally. This is logical because interception stocks are already small and depend more on rainfall frequency than on rainfall amount. Third, the increase in open-water evaporation (+0.25 %) is small and can be explained by decreases in vegetation interception that translated into increases in available energy for water evaporation in wetlands and rice paddies. Fourth, the relative reduction in snow accumulation (−14.63 %) is high since snow melt is unchanged. Lastly, the global mean evaporative partitioning is changed only insignificantly towards lower transpiration ratio.

The sensitivity of transpiration is highest over the US, Australia, subtropical South America and Africa, and other areas that at least during a part of the year are water-constrained. In the wet tropics, transpiration rates do not react to precipitation reductions. Vegetation interception experiences an insignificant relative decrease, which is highest in the north and the tropics. This is probably caused by a combination of lower original interception rates in the boreal forests and the relatively higher dependence on high rainfall frequency in the tropical forests. This uniform perturbation of precipitation forcing indicates that STEAM evaporation is much less sensitive to precipitation than runoff. This can be explained by the fact that evaporation is constrained by potential evaporation, which relates to other factors than just precipitation. In wet regions where soil moisture is close to saturation, any excess precipitation would more likely lead to increase in runoff rather than evaporation. The sensitivity of runoff to precipitation data is also reported in the literature (e.g. Fekete et al., 2004; Materia et al., 2010) and supports the view that runoff comparisons will not accurately describe how well land-surface models estimate evaporation when precipitation is uncertain.

Table 3.4: Overview of the sensitivity of runoff, evaporation, and model snow accumulation to uniform reduction in precipitation quantity (global mean for 1999–2008).

Flux	Default		5 % reduction in P		Change
	$km^3\ year^{-1}$	% E	$km^3\ year^{-1}$	% E	%
P	118 236	–	112 324	–	−5
Q	43 216	–	38 762	–	−10.3
E	73 933	100	72 644	100	−1.74
E_t	43 376	58.7	42 392	58.4	−2.27
E_v	15 288	20.7	15 152	20.9	−0.89
E_f	7706	10.4	7,657	10.5	−0.64
E_{sm}	4335	5.9	4207	5.8	−2.95
E_w	3228	4.4	3236	4.5	+0.25
dS_{snow}/dt	1087	–	918	–	−15.5

3.5. CONCLUSIONS

This chapter evaluated the global hydrological land-surface model STEAM. The ability of STEAM to simulate evaporation and evaporation partitioning realistically was evaluated

by comparison with other modelling studies, global data sets, and reported values from field studies. STEAM's total terrestrial evaporation rate (73 900 km^3 $year^{-1}$) is comparable with previous estimates – lower than reanalysis products, but higher than other land-surface models. Reasons for this include that we do not add water in data assimilation as in reanalysis, and compared to other land-surface models we use a relatively high precipitation input and also include irrigation and wetlands. Overall, STEAM simulates global evaporation partitioning within the range of previous estimates: 59 % transpiration, 21 % vegetation interception, 10 % floor interception, and 6 % soil moisture evaporation. The global mean transpiration ratio in STEAM is similar to or somewhat higher than other land-surface models, and in line with the recent literature compilation study of Schlesinger and Jasechko (2014). Vegetation interception ratios in forests are comparable with both the findings from a global satellite-based estimate of interception (Miralles et al., 2010) and with reported values from field studies in the tropics. In agreement with previous studies (McNaughton and Jarvis, 1983; de Bruin and Jacobs, 1989; Teuling et al., 2010), STEAM also simulates higher transpiration ratios in short vegetation types than in forests.

Runoff is highly sensitive to precipitation input data, and the runoff evaluation shows that the choice of precipitation forcing has a much higher influence on simulated mean annual runoff than model tuning. The use of the state-of-the-art precipitation product MSWEP considerably improved runoff simulations in a number of large basins, including Yangtze, Congo, and Brahmaputra.

Simplifications in STEAM include neglect of runoff routing, groundwater, and sublimation processes. Koster and Milly (1997) and Koster and P. Mahanama (2012) concluded among others that compatibility between runoff and evaporation formulations can be important due to interaction through soil moisture. Dry-season evaporation might also be underestimated by the neglect of groundwater (Miguez-Macho and Fan, 2012) and hydraulic redistribution of soil water by roots (Lee et al., 2005). Crop simulations presently also do not follow sowing and harvesting dates. The neglect of sublimation can further cause underestimation of interception (Schlaepfer et al., 2014). Nevertheless, the model evaluation analyses and the sensitivity tests suggest that that the current model set-up is a reasonable simplification for the research questions asked.

STEAM runs at the same temporal and spatial scale as the atmospheric moisture recycling model WAM-2layers, and can be used in both one- and two-way coupling. One-way coupling, i.e., forcing WAM-2layers with STEAM output, is used in van der Ent et al. (2014) to investigate the differences in moisture recycling between direct and delayed evaporation fluxes. Two-way coupling, i.e. feeding induced changes in precipitation from WAM-2layers back to STEAM, is applied in Chapter 6 to investigate the effect of land-use change on moisture recycling. Although WAM-2layers does not simulate precipitation, such analyses are possible by for example assuming that changes in terrestrial evaporation proportionally alter the atmospheric moisture content or the precipitation with continental origin.

4

TEMPORAL CHARACTERISTICS OF INTERCEPTION AND TRANSPIRATION

A good rain knows its proper time

Du Fu (712-770)

Although terrestrial evaporation consists of different fluxes (i.e. transpiration, vegetation interception, floor interception, soil moisture evaporation, and open-water evaporation), moisture recycling studies have up to now only analysed their combined total. This chapter investigates the temporal characteristics of partitioned evaporation. We show that the terrestrial residence timescale of transpiration (days to months) has larger inter-seasonal variation and is substantially longer than that of interception (hours). This cause the atmospheric residence time of interception evaporation to be slightly shorter (8 days) than transpiration (9 days). Transpiration is more likely to occur during dry periods and to be advected over large distances. Changes in evaporative partitioning following land-use change may have implications and provide answers for distant agriculture and landscape resilience.

This chapter is based on:

Wang-Erlandsson, L., van der Ent, R. J., Gordon, L. J., and Savenije, H. H. G.: *Contrasting roles of interception and transpiration in the hydrological cycle — Part 1: Temporal characteristics over land*, Earth System Dynamics, 5, 441–469, 2014.

van der Ent, R. J., Wang-Erlandsson, L., Keys, P.W., and Savenije, H. H. G.: *Contrasting roles of interception and transpiration in the hydrological cycle — Part 2: Moisture recycling*, Earth System Dynamics, 5, 471–489, 2014.

4.1. INTRODUCTION

Terrestrial evaporation is mediated by land-surface properties, rainfall characteristics, and evaporative demand – conditions that humans are modifying at an unprecedented scale (e.g. Crutzen, 2002; Dore, 2005; Gordon et al., 2005; Rockström et al., 2009b; Trenberth et al., 2011). Understanding evaporation interaction with land and climate is essential, because evaporation holds a key role in regulating hydrological flows as well as atmospheric feedback. One important land–atmosphere mechanism is the contribution of terrestrial evaporation to precipitation through the process of moisture recycling, which has implications for both water and land management. For example, studies have shown that changes in land use may potentially reduce crop yields through reductions in moisture recycling (Bagley et al., 2012), that irrigation may increase moisture recycling (e.g. Tuinenburg, 2013; Wei et al., 2012), and that livelihoods in some semi-arid regions are particularly vulnerable to changes in upwind moisture source regions (Keys et al., 2012).

Up to now, moisture recycling studies have only analysed total evaporation. However, the partitioning between transpiration, vegetation interception, floor interception, soil moisture evaporation, and open-water evaporation has depended on land use and meteorological conditions. For example, interception and soil moisture evaporation are ephemeral (Gerrits et al., 2009), whereas transpiration continues long into the dry season depending on infiltration rates and the capacity of the soil in the root zone to retain moisture. Vegetation that can access deeper soil moisture can therefore maintain evaporation through transpiration beyond what can be sustained by interception alone. Another example is that transpiration ratios (i.e. transpiration as part of total evaporation) can be relatively higher in wet years (compared to dry years), but smaller in wet months (compared to dry months) (Savenije, 2004). The reason is that wet months tend to have high interception preceding transpiration and consuming the already limited energy available for evaporation, whereas wet years tend to receive increased rainfall during the rainy season that stores and transpires into the dry season. Savenije (2004) suggested that these temporal differences of different evaporation fluxes would have different moisture recycling patterns.

Earlier studies of evaporation timescales have analysed the role of soil moisture for drought (e.g. Serafini and Sud, 1987; Delworth and Manabe, 1988), the precipitation persistence in climate modelling (e.g. Koster and Suarez, 1996), and the evaporation response timescale to drying soils (e.g. Teuling et al., 2006) as well as for inter-comparing and improving land-surface models (e.g. Lohmann and Wood, 2003; Wang et al., 2006). Scott et al. (1997) described the timescale of evaporation response through convolution representation of precipitation history and applied it on interception, soil evaporation, and transpiration globally. Lohmann and Wood (2003) employed a similar approach to compare 16 land-surface models and found significant differences in response between models. Nevertheless, the role of evaporation partitioning and evaporation timescales specifically for moisture recycling has not been studied.

Although there have been many efforts in estimating global land evaporation and evaporation partitioning, the actual magnitudes of the different evaporative fluxes remain disputed. Methods to estimate spatially distributed global land evaporation can broadly be grouped into land-surface models, remote sensing, reanalysis, and data-upscaling

methods. While the latter two generally do not provide evaporation partitioning, the first two methods are highly reliant on the assumed parameters, algorithms, and terminology definitions in order to assess the partitioning. Thus, it is not surprising that the range of reported evaporation partitioning is large. Model-based global mean transpiration ratio estimates range from 38 to 80 % (see Sect. 3.4.2 and Table 3.3).

Validation of spatially and temporally distributed global evaporation partitioning data is challenging, as observational measurements are constrained in space and time, and suffer from uncertainties themselves. Although eddy covariance measurements have often been used in validating modelled total evaporation (e.g. Liu et al., 2012; Miralles et al., 2013; van den Hoof et al., 2013; Bagley et al., 2011) and sporadically used for deriving evaporation (e.g. Jung et al., 2010) and evaporation partitioning (e.g. Czikowsky and Fitzjarrald, 2009), there are still many issues to be resolved: e.g. non-closure of energy balance, location bias, and upscaling (e.g. Twine et al., 2000; Wilson et al., 2002; Chen et al., 2011; Xiao et al., 2012). A combination of isotope measurement techniques and satellite observations were recently used to investigate evaporative partitioning at the river basin and global scale (Jasechko et al., 2013, 2014), leading to high and disputed (Coenders-Gerrits et al., 2014; Schlaepfer et al., 2014; Sutanto et al., 2014) estimates of the transpiration ratio (80–90 %) (see also Sect. 3.4.2). In addition, research initiatives such as GEWEX (Global Energy and Water Cycle Experiment) LandFlux-EVAL and ESA (European Space Agency) WACMOS-ET (WAter Cycle Observation Multi-mission Strategy – EvapoTranspiration) (e.g. Jiménez et al., 2011; Miralles et al., 2013) that accumulate knowledge by inter-comparing evaporation and evaporation partitioning are still ongoing.

Thus, there remain many difficulties and uncertainties in estimating evaporation partitioning. In particular, the lack of evaporation partitioning data available at the spatial and temporal scale required for moisture tracking might be a reason for the omission of moisture recycling research in the potentially contrasting effects of separated evaporation fluxes.

This chapter investigates the temporal characteristics of evaporation fluxes on land and in the atmosphere: (1) what are the terrestrial residence timescales of evaporation fluxes? (2) How does the timing of precipitation relate to evaporation partitioning? (3) How robust are the temporal characteristics to uncertainties in storage capacities? (4) What are the atmospheric residence times of the individual evaporation components? This provides new information on the susceptibility of regions to land-use changes.

4.2. METHODS

4.2.1. TIMESCALES OF EVAPORATION FLUXES

The timescales τ_{ts} of the evaporation fluxes is defined as the mean stock over the mean flux rate in question j:

$$\tau_{\mathrm{ts},\,j} = \frac{\overline{S_j}}{\overline{E_j}}. \tag{4.1}$$

Figure 2.1 shows the stock of origin for each evaporation flux. Because both E_{sm} and E_{t} come from S_{uz}, we assumed a stock of soil moisture evaporation $S_{\mathrm{uz,sm}}$ and a stock of transpiration $S_{\mathrm{uz,t}}$. To obtain $S_{\mathrm{uz,sm}}$, we multiplied θ_{top} with the assumed topsoil depth

y_{top}. To obtain the stock $S_{uz,t}$, $S_{uz,sm}$ was subtracted from the total water available in the unsaturated zone S_{uz}:

$$S_{uz,t} = S_{uz} - S_{uz,sm} = \theta_{uz} y_{uz} - \theta_{top} y_{top}. \tag{4.2}$$

Because the timescale becomes infinite when the flux approaches 0, timescales are not given for areas where the mean evaporation flux is below 0.01 mm d^{-1}. Coastal areas where the land area fraction is less than 100 % were removed from the timescale analysis. The timescale for open-water evaporation was not calculated.

4.2.2. EVAPORATION PARTITIONING: TIME SINCE PRECIPITATION

We are interested in how evaporation partitioning evolves with time after precipitation ceases. To do this, we grouped each grid cell at every time step in categories depending on the time that has past since precipitation. Grid cells at a certain time step that has not received precipitation since n time steps back are placed in the $(n+1)$th category. Subsequently, evaporation partitioning for each category was retrieved from the model simulation.

In addition, the importance of the evaporation partitioning in relation to rainfall also depends on the evaporated quantity. Thus, we present the portion of evaporation flux during rainy or dry conditions by using evaporation efficiencies β_{wet} and β_{dry} as measures:

$$\beta_{wet,j} = \frac{\sum E_{wet,j}}{\sum E_j}, \quad \beta_{dry,j} = \frac{\sum E_{dry,j}}{\sum E_j}. \tag{4.3}$$

Here, β_{wet} represents the mean annual portion of an evaporation flux that evaporates during a 3 h time step with precipitation, and β_{dry} represents the mean annual portion of an evaporation flux that evaporates after experiencing more than 24 h of no precipitation. To qualify as a wet time step, a 3 h time step must have > 0.01 mm precipitation. The subscript $_j$ denotes the evaporation flux in question. Construction of these evaporation efficiency measures is useful for answering questions such as, how much of total vegetation interception occurs during rainy periods?

4.2.3. ROBUSTNESS

Large uncertainties exist in evaporation partitioning and estimation of storage capacities. To verify how robust or sensitive the temporal characteristics are to these uncertainties, we performed a sensitivity analysis with two scenarios: transpiration-plus and interception-plus. In transpiration-plus, the unsaturated zone storage capacity increased by 20 % and the vegetation and floor interception storage capacity decreased by 50 %. In interception-plus, the increase and decrease in the storages are reversed; see Table 4.1.

4.2.4. ATMOSPHERIC MOISTURE TRACKING

The moisture tracking model WAM-2layers is used to track the different evaporation fluxes. WAM-2layers is an update to the previously used WAM-1layer (van der Ent et al., 2010; Keys et al., 2012; van der Ent and Savenije, 2013). The key difference being the addition of a second atmospheric layer instead of merely having one layer. The underlying principle

of WAM-2layers is the water balance:

$$\frac{\partial S_k}{\partial t} = \frac{\partial (S_k u)}{\partial x} + \frac{\partial (S_k v)}{\partial y} + E_{\mathrm{i},k} + E_{\mathrm{t},k} - P_k + \xi_k \pm F_{\mathrm{v}} \left[\mathrm{L}^3\,\mathrm{T}^{-1}\right], \tag{4.4}$$

where S_k is the atmospheric moisture storage (i.e., precipitable water) in layer k (either the top or the bottom layer), t is time, u and v stand for the wind components in x (zonal) and y (meridional) direction, ξ is a residual and F_{v} is the vertical moisture transport. We calculate moisture transport over the boundaries of the grid cells. Change in atmospheric moisture due to horizontal transport is described by

$$\frac{\Delta (S_k u)}{\Delta x} = F^{-}_{k,x} - F^{+}_{k,x} \tag{4.5}$$

and

$$\frac{\Delta (S_k v)}{\Delta y} = F^{-}_{k,y} - F^{+}_{k,y}, \tag{4.6}$$

where F_k is the moisture flux over the boundary of a grid cell in the bottom or top layer. Superscript "−" stands for the western and southern boundaries of the grid cell respectively and "+" stands for the eastern and northern boundaries respectively. The moisture flux can be calculated as follows:

$$F_k = \frac{L}{g\rho_{\mathrm{w}}} \int_{p_{\mathrm{top}}}^{p_{\mathrm{bottom}}} q u_{\mathrm{h}} \mathrm{d}p, \tag{4.7}$$

where L is the length of the grid cell perpendicular to the direction of the moisture flux, g is the gravitational acceleration, ρ_{w} the density of liquid water ($1000\,\mathrm{kg\,m^{-3}}$), p stands for pressure, q for specific humidity and u_{h} is the horizontal component in either x or y direction. For the top layer applies: $p_{\mathrm{top}} = 0$ and $p_{\mathrm{bottom}} = p_{\mathrm{divide}}$. For the bottom layer applies: $p_{\mathrm{top}} = p_{\mathrm{divide}}$ and $p_{\mathrm{bottom}} = p_{\mathrm{surface}}$.

The evaporation from interception and transpiration E_{i} and E_{t} (together E) enter only in the bottom layer, thus $E_k = E$ in the bottom layer and $E_k = 0$ in the top layer. Precipitation is assumed to be immediately removed from the moisture storage (i.e., no exchange of falling precipitation between the top and bottom layer) and we assume "well-mixed" conditions for precipitation. For further details, see van der Ent et al. (2014).

In the context of continental moisture recycling (see also van der Ent et al., 2010) precipitation on land P were separated as follows:

$$P = P_{\mathrm{o}} + P_{\mathrm{c}} = P_{\mathrm{o}} + P_{\mathrm{c,i}} + P_{\mathrm{c,t}}, \tag{4.8}$$

where P_{o} is the part that is of oceanic origin and P_{c} is the continentally recycled part of the precipitation (i.e., most recently evaporated from a continental area). P_{c} can be split further into $P_{\mathrm{c,i}}$ (i.e., the recycled precipitation that originates from vegetation interception, floor interception, soil moisture and inland waters) and $P_{\mathrm{c,t}}$ (i.e., the recycled precipitation that originates from transpiration).

Similarly, we split land evaporation E:

$$E = E_o + E_c = E_{o,i} + E_{o,t} + E_{c,i} + E_{c,t}, \tag{4.9}$$

where E_o is the part of the evaporation that precipitates on the ocean and E_c is the continental recycling part (i.e., returns as continental precipitation). Subscripts i and t denote the interception (Eq. 4.14) and transpiration respectively. It also holds that $E_i = E_{o,i} + E_{c,i}$ and that $E_t = E_{o,t} + E_{c,t}$.

4.2.5. ATMOSPHERIC LIFETIME OF RECYCLED MOISTURE

Previous studies by Trenberth (1998) and by van der Ent and Savenije (2011) calculated the local depletion and restoration time scales of atmospheric moisture, defined as the atmospheric moisture storage over precipitation and evaporation respectively. Trenberth (1998) estimated the average time scale over land to be around nine days. However meaningful, these time scales only provided local information, but did not indicate the actual time spent in the atmosphere by a recycled water particle. Therefore, we propose new metrics that describe the actual time spent in the atmospheric. We define the "lifetime of continentally recycled precipitation":

$$\tau_{\rho,c} = N(P_c \leftarrow E_c), \tag{4.10}$$

where N stands for the time spent in the atmosphere, or in other words, the age of the water particle. The lifetime of continentally recycled precipitation $\tau_{\rho,c}$ is a measure at the point where a water particle precipitates and stands for the average time spent between continental evaporation and continental precipitation, or in other words, the average age at the point where a water particle precipitates. Note that $\tau_{\rho,c}$ only provides information on the recycled part of the precipitation and not on the total precipitation (see Eq. 4.8). Likewise we define the "lifetime of the interception that recycles on land":

$$\tau_{\varepsilon,c,i} = N\left(E_{c,i} \rightarrow P_{c,i}\right) \tag{4.11}$$

and the "lifetime of the transpiration that recycles on land":

$$\tau_{\varepsilon,c,t} = N\left(E_{c,t} \rightarrow P_{c,t}\right). \tag{4.12}$$

Both metrics in Eqs. (4.11) and (4.12) are defined at the place where evaporation occurs at the land surface (E_c in Eq. 4.9) and determine the average time an evaporated water particle that returns as precipitation on land will spend in the atmosphere.

Age tracers were used to calculate the lifetimes. An age tracer increases linearly with time and at each time step t the model calculates the age N_g of the tagged moisture present at that location according to the following formula:

$$N_g(t) = \begin{pmatrix} S_g(t-1)\left(N_g(t-1)+\Delta t\right) \\ +\sum F_g^{in}\Delta t\left(N_g^{in}(t-1)+\Delta t\right) \\ -\sum F_g^{out}\Delta t\left(N_g(t-1)+\Delta t\right) \\ -P_g\Delta t\left(N_g(t-1)+\Delta t\right)+E_g\Delta t\dfrac{\Delta t}{2} \end{pmatrix} / S_g(t), \tag{4.13}$$

where the subscript $_g$ stands for tagged water, here referring to either interception or transpiration.

4.2.6. DATA INPUT FOR MOISTURE TRACKING

The input data for WAM-2layers comes from ERA-I (Dee et al., 2011) and STEAM. From ERA-I we use precipitation and evaporation over the oceans, as well as specific humidity and zonal and meridional wind speed. We downloaded these data at model levels spanning the atmosphere from zero pressure to surface pressure. Surface fluxes were downloaded at three-hourly intervals and the other data at six-hourly. The data we use are on a 1.5° latitude × 1.5° longitude grid and cover the period of 1998–2009, but the results are presented for 1999–2008, because we use 1 year as model spin-up for both the backward and forward tracking. For the terrestrial evaporation, we use the partitioned evaporation fluxes computed by STEAM.

In the moisture tracking, we combine the direct (purely physical) terrestrial evaporative fluxes from STEAM into one term E_i, containing evaporation from interception, soil moisture and inland waters:

$$E_i = E_\mathrm{v} + E_\mathrm{f} + E_\mathrm{sm} + E_\mathrm{w} \tag{4.14}$$

Transpiration E_t, the delayed (biophysical) evaporative flux, on the other hand provides a slow feedback with a large storage reservoir, which is the other component that we track.

4.3. RESULTS AND DISCUSSION

4.3.1. TERRESTRIAL TIMESCALES

The modelled global average timescale (Eq. 4.1) is 1.3 h for vegetation interception and 7.7 h for floor interception, but 42 days for soil moisture evaporation and 274 days for transpiration in areas with mean evaporation rates higher than 0.01 mm d^{-1}. Evaporation rates from vegetation cover and floor are large compared to their respective stocks, resulting in small timescales for interception. In contrast, the stocks in the unsaturated zone are many times larger than the interception stocks and cause the timescales of soil moisture evaporation and transpiration to extend to several days and even months. The use of an area reduction factor (see Eqs. 2.44 and 2.45) leads to interception storage capacities that are smaller in the model than in reality, thus presumably causing some underestimation of the interception timescales. Nevertheless, the robustness test (Table 4.1) shows that the magnitude of all evaporation timescales (except for transpiration) are relatively robust against uncertainties in storage capacities.

Figure 4.1 shows the spatial distribution of mean terrestrial residence timescales (i.e. stock divided by flux) of the partitioned evaporation fluxes (Eq. 4.1). We see that timescales are in general prolonged over the tropics and over the cold northern latitudes. This finding is consistent with the transpiration response timescale provided by Scott et al. (1997). Over the tropics, evaporation rates are high, but the stocks are also relatively larger. The timescales of floor and soil moisture evaporation are extended in the tropics, because these fluxes there are suppressed by the relatively high vegetation interception and transpiration.

The temporal variation of the evaporation fluxes at different latitudes is displayed in Fig. 4.2. Seasonality is distinct for all evaporation fluxes, in particular for transpiration timescales. While the mean latitude transpiration timescale can extend to over 500 days in the mid-latitude winter, it falls well below 100 days in the summer.

Regions and seasons with extremely high transpiration timescales (> 300 days) largely coincide with low transpiration in the north, whereas high transpiration rates coincide with intermediate or low timescales (< 100 days). However, relatively high vegetation interception timescales seem positively correlated with high vegetation interception in the tropics (compare Fig. 3.1 and Fig. 4.1). This difference can be explained by the limiting factor to evaporation. Transpiration timescales approach infinity as the stock is still wet, whereas vegetation interception timescales often approach 0 when vegetation interception is caused by depletion in vegetation interception stock rather than in evaporative demand. Thus, the high transpiration timescales in the north should be understood as the result of declining evaporative demand, whereas the high vegetation interception timescales in the tropics can be interpreted as the result of a steady and ample supply of precipitation to the vegetation interception stock.

The higher the interception ratios, the lower the evaporation timescales on land (also in consistency with, e.g., Scott et al., 1995), and the faster the overall feedback to the atmosphere. The regions that have a high vegetation interception ratio (Fig. 3.4) coincide with the regions with low atmospheric moisture recycling length scales (van der Ent and Savenije, 2011). This suggests that tropical interception is very important for vegetation to maintain atmospheric moisture in the air, and it could constitute a large portion of local recycling due to immediate feedback. However, moisture supplied to continents in general (van der Ent et al., 2010), the world's most important croplands (Bagley et al., 2012), or rainfall-dependent regions (Keys et al., 2012) also relies on remote evaporation sources, which could account for a large part of transpiration. For such cases, upwind modifications that result in changed transpiration rates (e.g. changes in vegetation species, rainwater harvesting practice, CO_2 concentrations) may play a larger role for downwind regions than changes in interception. A detailed investigation of the role of interception and transpiration for local and remote moisture recycling is performed in Part 2.

4.3.2. EVAPORATION PARTITIONING AFTER PRECIPITATION EVENT

Figure 4.3 shows the mean latitudinal evaporation ratios by time since precipitation last occurred. Mean latitudinal transpiration ratio is up to 40 % during the wet time steps with precipitation, but it can amount to up to 90 % after just a few dry 3 h time steps. The largest increase in transpiration ratios with time since precipitation are seen in the cold northern latitudes, where moisture availability is expected to exceed evaporative demand. However, the vegetation interception ratio is high (up to approximately 60 %) during wet time steps but falls drastically to almost no interception within 6 h. Similarly to transpiration, soil moisture evaporation ratios generally increase with precipitation-free hours. However, the steepest increase in soil moisture evaporation ratios are found in the equatorial band where the total soil moisture evaporation is very low.

4.3.3. ROBUSTNESS

Table 4.1 shows that transpiration and soil moisture evaporation occur both during wet and dry conditions, whereas vegetation and floor interception evaporation occur almost exclusively during time steps with precipitation. The table shows that 31 % of all transpiration occurs during time steps that have endured more than 1 day

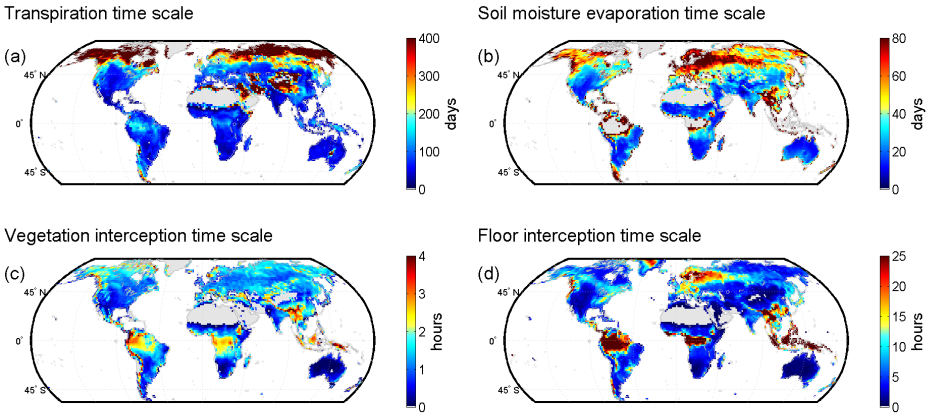

Figure 4.1: Average surface timescales of different evaporation fluxes: **(a)** transpiration, **(b)** soil moisture evaporation, **(c)** vegetation interception, and **(d)** floor interception (1999–2008). Grey indicates grid cells with mean evaporation rates below 0.01 mm d^{-1}. Note that the units are in hours for E_v and E_f, and in days for E_t and E_{sm}; see Eq. (4.1). Results are discussed in Sect. 4.3.1.

of no precipitation, when no vegetation interception occurs. Instead, 96 % of the vegetation interception occurs on a 3 h time step with precipitation, whereas only 45 % of transpiration evaporates in such conditions. It is also noteworthy that these evaporation efficiency numbers (Eq. 4.3) are robust to changes in the evaporation partitioning: for example, the 96 % vegetation interception efficiency persists even when the vegetation interception ratio varies between 12 and 27 %. In other words, even with large differences in the evaporation ratio, interception is likely to occur almost exclusively within the wet period, whereas transpiration may have a substantial time lag between the moment water enters the soil and exits through a plant's stomata. In for example the field study of Farah et al. (2004), transpiration at a tropical woodland site continued for 2 months after rainfall. This also explains why transpiration dominates in the dry season and could have substantial effects on moisture recycling patterns. Furthermore, although a change in evaporation partitioning does not change the vegetation interception and transpiration efficiencies, it changes the total evaporation efficiency and the overall temporal distribution of evaporation.

4.3.4. GLOBAL AVERAGE LIFETIME OF HYDROLOGICAL FLUXES

Figure 4.4 presents an image of the global hydrological cycle over land. In contrast to traditional images of the hydrological cycle (e.g., Chahine, 1992) we include a quantification of moisture recycling, partitioned evaporation and the lifetime of all these components separately. Before precipitation falls on land, its average atmospheric residence time is about 10 days. We estimate that about 38 % of continental precipitation P is transformed into runoff Q and the remaining part evaporates by direct (purely physical) fluxes E_i and by the delayed (biophysical) flux E_t. A portion of this land evaporation

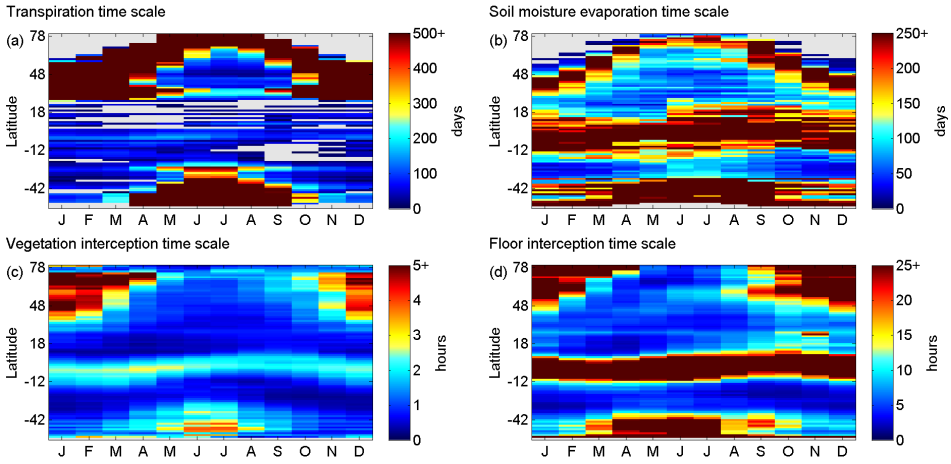

Figure 4.2: Changes in terrestrial timescales (Eq. 4.1) over the year and different latitudes (1999–2008). Note that the units are in hours for E_v and E_f, and in days for E_t and E_{sm}. Grey indicates when a timescale approaches infinity. Results are discussed in Sect. 4.3.1

is advected to the oceans and precipitates there E_o. The remaining part recycles over land, but interestingly, interception $E_{c,i}$ and transpiration $E_{c,t}$ do so in different relative magnitudes. Of interception, 60 % ($E_{c,i}/E_i$) recycles, while transpiration recycles slightly less at 56 % ($E_{c,t}/E_t$). The lifetime in the atmosphere of evaporated water is on average more than a week, which is similar to a previous estimate of 9.2 days (Bosilovich et al., 2002). The recycled part of evaporation, however, spends on average less than a week in the atmosphere on average. We can also observe that (the recycled part of) interception has a shorter lifetime in the atmosphere. Finally, global continental precipitation recycling P_c is estimated at 36 %, slightly less than the 40 % estimated in a previous study using WAM-1layer and ERA-I evaporation (van der Ent et al., 2010). This is mainly caused by the other forcing data, STEAM instead of ERA-Interim, but about 0.5 % is due to the inclusion of the second layer in WAM-2layers. Globally averaged, the recycling efficiencies and atmospheric lifetimes are not very different for interception and transpiration, but locally these differences can be large.

4.3.5. ATMOSPHERIC LIFETIME OF RECYCLED MOISTURE

Figure 4.5 shows the time spent in the atmosphere by the moisture that recycles over land. Figure 4.5a indicates the time that continentally evaporated moisture has spent in the atmosphere until it precipitates (Eq. 4.10). Figure 4.5b (Eq. 4.11) and c (Eq. 4.12) indicate the time it takes before direct (interception, soil moisture and inland waters) and delayed (transpiration) evaporative fluxes return to the terrestrial land surface.

We can see that in general the direct evaporative fluxes (Fig. 4.5b) remain in the atmosphere for a shorter period of time compared to transpiration (Fig. 4.5c). We can explain this by the fact that the terrestrial time scales of the direct evaporative fluxes are much shorter than those of transpiration. The differences between Fig. 4.5b and c are less

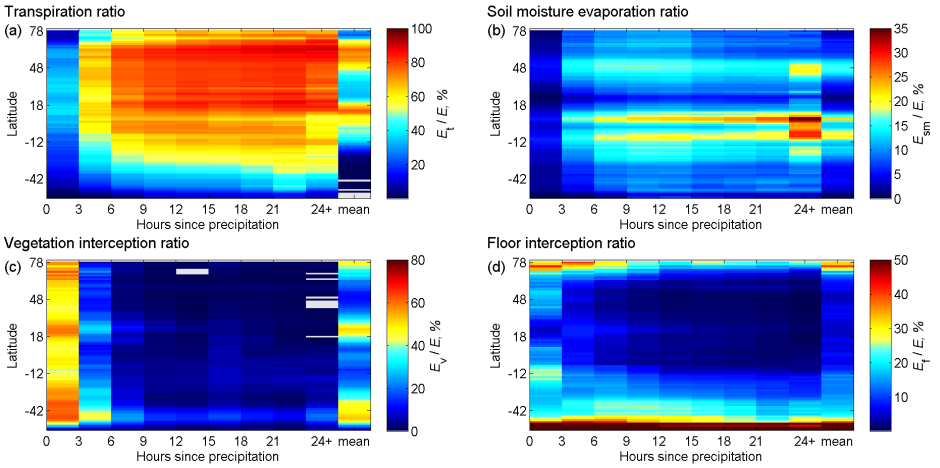

Figure 4.3: Evaporation partitioning with time since precipitation over terrestrial latitudes (1999–2008). Results are discussed in Sect. 4.3.2.

strong in the very wet tropical regions around the equator, as well as in the Andes and Himalaya mountains. This is probably caused by the absence of distinctively different precipitation triggering mechanisms throughout the year. On the other hand, we see several regions where the atmospheric lifetime of interception recycling (Fig. 4.5b) is much lower than that of transpiration recycling (Fig. 4.5c).

Interestingly, recycled precipitation (Fig. 4.5a) in North America has spent less time in the atmosphere than in Eurasia. We think that this could be explained by a fraction of evaporation in North America that passes over the Atlantic Ocean in summer and precipitates in Europe, which obviously increases the average atmospheric residence time. It seems that transpiration (Fig. 4.5c) is a slightly larger contributor to this cross-continental transport than the direct evaporative fluxes (Fig. 4.5b). See also animations in the Supplementary Information of van der Ent et al. (2014).

4.4. CONCLUSIONS

This chapter analysed the terrestrial temporal characteristics of different evaporation fluxes on land. Our analyses show a striking difference in mean annual global timescales between the different evaporation fluxes: 95–434 days for transpiration, 42–46 days for soil moisture evaporation, 5.2–11.6 h for floor interception, and 1.1–1.6 h for vegetation interception. The timescales also vary greatly over the seasons and latitudes. Most transpiration occurs several hours or days after a rain event, whereas interception is immediate. We find that 31 % of all transpiration occurs in time steps that have endured more than 1 day without precipitation, when no vegetation interception occurs. Instead, 96 % of the vegetation interception occurs on a 3 h time step with precipitation, whereas only 45 % of the transpiration occurs in such conditions. Uncertainties in parametrising storage capacities affect the evaporation partitioning ratios but have a smaller effect on

Table 4.1: Robustness to storage capacity parametrisation of STEAM (global mean for 1999–2008). The subscript t stands for transpiration, $_{sm}$ for soil moisture evaporation, $_{v}$ for vegetation interception, $_{f}$ for floor interception, and $_{uz}$ for unsaturated zone. Methods are described in Sect. 4.2.3, and results are discussed in Sects. 4.3.1 and 4.3.2.

	Default	Transpiration-plus	Interception-plus
Storage capacity			
$S_{v,max}$	100 %	50 %	150 %
$S_{f,max}$	100 %	50 %	150 %
S_R	100 %	120 %	80 %
Total evaporation	73 900 km^3 year^{-1}	73 200 km^3 year^{-1}	74 200 km^3 year^{-1}
Evaporation ratio			
E_t/E	59 %	64 %	54 %
E_{sm}/E	6 %	7 %	5 %
E_v/E	21 %	12 %	27 %
E_f/E	10 %	12 %	10 %
Timescales			
$\tau_{ts,t}$	274 days	434 days	95 days
$\tau_{ts,sm}$	42 days	43 days	46 days
$\tau_{ts,v}$	1.3 h	1.1 h	1.6 h
$\tau_{ts,f}$	7.7 h	5.2 h	11.6 h
Evaporation efficiency, <3 h after precipitation[a]			
β_{wet}	58 %	56 %	60 %
$\beta_{wet,t}$	45 %	46 %	43 %
$\beta_{wet,sm}$	39 %	44 %	35 %
$\beta_{wet,v}$	96 %	96 %	96 %
$\beta_{wet,f}$	83 %	87 %	79 %
Evaporation efficiency, >24 h without precipitation[b]			
β_{dry}	23 %	24 %	21 %
$\beta_{dry,t}$	31 %	31 %	31 %
$\beta_{dry,sm}$	32 %	29 %	34 %
$\beta_{dry,v}$	1 %	1.2 %	0.8 %
$\beta_{dry,f}$	3.9 %	2.8 %	5 %

[a] The evaporation efficiency is calculated for 3 h time steps with precipitation.
[b] The evaporation efficiency is calculated for 3 h time steps without precipitation for more than 24 h.

the relative differences in temporal characteristics. Only the transpiration timescales are significantly modified by storage capacity changes, but they are still substantially different from the interception timescales.

Moisture tracking reveals that 60 % of direct evaporation returns to the land surface, whereas this is 56 % for transpiration. The residence time of direct evaporation in the

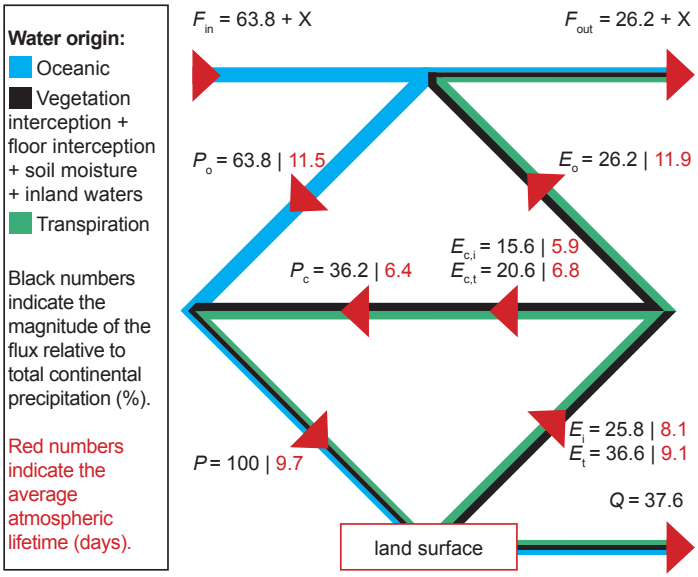

Figure 4.4: Global hydrological cycle over land, i.e., all continents considered together (1999–2008). F_{in} is the atmospheric moisture of oceanic origin that crosses the ocean-land boundary and enters the atmosphere above land. F_{out} is the atmospheric moisture that leaves the ocean-land boundary towards the ocean. Thus, X represents the atmospheric moisture of oceanic origin that passes through the continental atmosphere, but never precipitates. Precipitation on land P (set to 100 %) is composed of moisture evaporated from the ocean P_{o} and a recycled part P_{c}. On the land surface water runs off Q, or evaporates through direct evaporation E_{i} or through transpiration E_t. Part of this evaporation is lost to the ocean E_o, while other parts of the evaporation recycle $E_{\text{c,i}}$ and $E_{\text{c,t}}$. Evaporation data are from STEAM, precipitation data are from ERA-I, the recycled fractions and lifetimes are calculated by WAM-2layers (van der Ent et al., 2014) and the other terms follow from the water balance.

atmosphere is 8 days (6 for the recycling part only) and 9 days for transpiration. We attribute these results to the fact that interception has a small storage reservoir and therefore occurs mostly during wet spells. Transpiration on the other hand draws from a large storage reservoir and can occur during dry periods, when evaporated moisture is more likely to be advected over large distances, as well.

The results found are particularly useful from a landscape resilience perspective. Regions that receive precipitation from continentally recycled evaporation are vulnerable to upwind land-use changes. However, a region that receives precipitation originating from interception is more resilient to land-use changes in their source region than a region that depends on transpiration. A land-use change could for example reduce interception

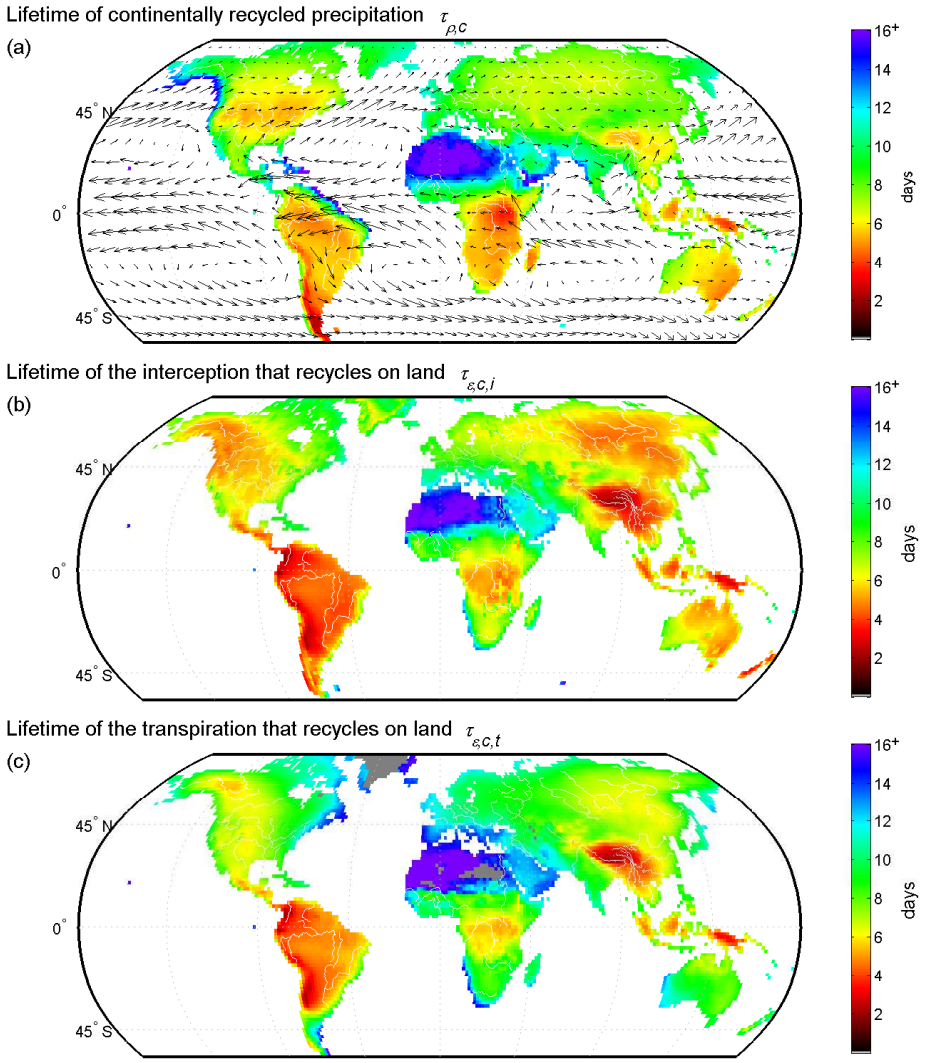

Figure 4.5: Average atmospheric lifetimes of recycled moisture (1999–2008). **(a)** lifetime of continentally recycled precipitation $\tau_{\rho,c}$ (defined at the point of precipitation), **(b)** lifetime of the interception that recycles on land $\tau_{\varepsilon,c,i}$ (defined at the point of evaporation), and **(c)** lifetime of the transpiration that recycles on land $\tau_{\varepsilon,c,t}$ (defined at the point of evaporation). Grey values on land indicate no data, due to the fact that the evaporative flux in question is zero. The arrows in **(a)** indicate the vertically integrated moisture fluxes.

capacity, but during a wet period this is likely to be compensated by other evaporative fluxes. Regions that receive precipitation from continentally recycled transpiration are less resilient to land-use changes in their source region, especially if a region's precipitation depends on transpiration in the dry season. Because when vegetation is removed, the

mechanism to retain and draw moisture from the root zone is lost as well, and total evaporation will be significantly reduced.

We conclude that changes in evaporative partitioning following land-use change may have implications and provide answers for landscape resilience, drought development, and effects on remote freshwater resources.

5

GLOBAL ROOT ZONE STORAGE CAPACITY FROM SATELLITE-BASED EVAPORATION

We know more about celestial bodies than soils underfoot.

Leonardo Da Vinci (1452-1519)

This chapter presents an "Earth observation-based" method for estimating root zone storage capacity (S_R). By assuming that vegetation does not root deeper than necessary to bridge critical dry periods, state-of-the-art satellite-based evaporation could be used to derive (S_R). Implementing the estimated (S_R) in the global hydrological model STEAM improved evaporation simulation overall, and in particular during the least evaporating months in sub-humid to humid regions with moderate to high seasonality. The results suggest that several forest types are able to create a large storage to buffer for severe droughts (with very long return period), in contrast to for example savannahs and woody savannahs (medium length return period), as well as grasslands, shrublands, and croplands (very short return period). The presented method eliminates the need for poor resolution soil and rooting depth data that form a limitation for achieving progress in the global land surface modelling community.

This chapter is based on:

Wang-Erlandsson, L., Bastiaanssen, W. G. M., Gao, H., Jägermeyr, J., Senay, G. B., van Dijk, A. I. J. M. Guerschman, J. P., Keys, P. W., van der Ent, R. J., Gordon, L. J., and Savenije, H. H. G.: *Global root zone storage capacity from satellite-based evaporation*, Hydrology and Earth System Sciences, 4, 1459–1481, 2016.

5.1. INTRODUCTION

Root zone storage capacity (S_R) determines the maximum amount of soil moisture potentially available for vegetation transpiration, and is critical for correctly simulating deep drainage and surface runoff (Milly, 1994). Its parameterisation is also important for land-atmosphere interactions, the carbon cycle, and climate modelling (e.g., Bevan et al., 2014; Feddes et al., 2001; Hagemann and Kleidon, 1999; Hallgren and Pitman, 2000; Kleidon and Heimann, 1998b, 2000; Lee et al., 2005; Milly and Dunne, 1994; Zeng et al., 1998), and for irrigation management and crop yield models (e.g., Bastiaanssen et al., 2007; Hoogeveen et al., 2015).

However, root zone storage capacity is very difficult to measure and observe in the field, especially at the larger scales that are relevant for many modelling needs. Rooting profiles measurements are also scarce, and difficult to generalise since vegetation rooting systems naturally adapt to prevailing climates and soil heterogeneities (e.g., Gentine et al., 2012; Sivandran and Bras, 2013). Even when rooting profiles are available, difficulties arise in translating them to root zone storage capacity, due to variations in root densities, hydrological activity, horizontal spatial heterogeneities, and uncertainties in soil profile data including hard pans.

5.1.1. BACKGROUND

Broadly six types of approaches to estimate the root zone storage capacity have been suggested or are in use in hydrological and land surface models: the *field observation based approach*, the *look-up table approach*, the *optimisation approach*, the *inverse modelling approach*, the *calibration approach*, and the *mass balance based approach*. These approaches are described below and compared in Supplementary Table S1 in Wang-Erlandsson et al. (2016). Some of these approaches estimate rooting depth or root profiles, and can be translated to root zone storage capacity through combination with soil plant available water (Sect. 5.3.3., Eq. 5.12), even though it is a simplification.

The *field observation based approach* provide estimates of rooting depths based on rooting depth measurements (Doorenbos and Pruitt, 1977; Dunne and Willmott, 1996; Jackson et al., 1996; Schenk and Jackson, 2002; Zeng, 2001) and has the advantage of being constructed from actual observations of vertical rooting distribution (Canadell et al., 1996; Jackson et al., 1996). To scale up rooting depth to the global scale, Schenk and Jackson (2002) used the mean biome rooting depth and Schenk and Jackson (2009) employed an empirical regression model based on reported root profile from literature. However, this method suffers from data scarcity and location bias, and risks unlikely vegetation and soil combinations due to data uncertainty (Feddes et al., 2001). Moreover, it requires assumptions on water uptake from a certain fraction of the entire observed root profile. Observations show that many woody and herbaceous vegetation species are able to access very deep layers in a variety of soil conditions (Canadell et al., 1996; Stone and Kalisz, 1991), up to 18 m in Amazonian tropical forest (Nepstad et al., 1994), 53 m in the desert of the south-western United States (Phillips, 1963), and 68 m (possibly 140 m) in the central Kalahari dry savannah (Jennings, 1974). However, isolated roots that go very deep does not necessarily mean that vegetation across the landscape can exploit the full soil to that depth.

The *look-up table approach* is used in hydrological and land surface modelling to

parametrise root zone storage capacity based on literature values of mean biome rooting depth and soil texture data (e.g., Müller Schmied et al., 2014; Wang-Erlandsson et al., 2014). This approach facilitates land-cover change experiments and is grounded in literature, but assumes root zone storage capacity to be a function of merely land-cover and soil type, with little consideration for climatic adjustments. This is a major oversight, as plants within the same vegetation type can exhibit a large span of root zone storage capacities in different climates and landscapes by adaptation to environmental conditions (Collins and Bras, 2007; Feldman, 1984; Gentine et al., 2012; Nepstad et al., 1994). Moreover, an incompatibility issue may arise if the literature based rooting depths employs a land-cover classification different from that of the land surface model (Zeng, 2001).

The *optimisation approach* predicts vertical rooting depth based on soil, climate, and vegetation data, and assumptions about the soil hydraulic properties and root distribution behaviour. Often, optimal root profiles are derived based on maximised net primary production (Kleidon and Heimann, 1998a), carbon or transpiration gain (e.g., Collins and Bras, 2007; Schwinning and Ehleringer, 2001; van Wijk and Bouten, 2001; Yang et al., 2016), sometimes also while being as shallow as possible (e.g., Laio et al., 2006; Schenk, 2008). The optimisation techniques used differ widely, including genetic algorithm (Schwinning and Ehleringer, 2001; van Wijk and Bouten, 2001), physical ecohydrological modelling (Collins and Bras, 2007; Hildebrandt and Eltahir, 2007), simple analytical modelling (Laio et al., 2006), and stochastic modelling (Schenk, 2008). This approach is powerful for improving the understanding of root profile development and can be useful for land surface models with explicit root distribution description (Smithwick et al., 2014). Nevertheless, further model development is needed to handle all types of environments (e.g., additional routines to handle groundwater uptake, acidic soil horizons, or low soil temperature) (Schenk, 2008). Moreover, the optimisation models commonly ignores the soil evaporation component and may thus overestimate the effective rooting depth (Yang et al., 2016). This is, however, addressed in Yang et al. (2016).

The *inverse modelling approach* estimate rooting depth using a model to iteratively simulate a variable available from satellite data (e.g., net or gross primary production, absorbed photosynthetically active radiation, or total terrestrial evaporation) with different rooting depth parameterisations (Ichii et al., 2007, 2009; Kleidon, 2004). This approach has a large spatial coverage while being indirectly observation-based, but is also dependent on soil information as well as the land surface model performance. Recently, this approach has also been applied at the local scale to approximate the root zone storage capacity by minimising differences between evaporation modelled from water balance and evaporation from remote sensing (Campos et al., 2016).

The *calibration approach* is widely used in hydrology, whereby a hydrological model is calibrated on the root zone storage capacity, using hydrological records on precipitation, runoff and evaporation, sometimes in combination with expert knowledge (e.g., Feddes et al., 1993; Fenicia et al., 2008; Jhorar et al., 2004; Winsemius et al., 2009; Gharari et al., 2014). However, the parameters derived are tied to the model used for calibration and are not necessarily comparable to measurable variables in nature, since they tend to compensate for uncertainties in model structure and data. In addition, since discharge is often the only observed variable (or one of only a few), the calibration approach is only suitable for applications at the catchment scale. For global hydrological

models, parameters can be calibrated separately for a selection of gauged river basins and transferred to neighbouring ungauged catchments (Döll et al., 2003; Güntner, 2008; Hunger and Döll, 2008; Nijssen et al., 2001; Widén-Nilsson et al., 2007). This procedure, known as regionalisation, has (to our knowledge) only been performed for other parameter values than the root zone storage capacity, although the principle does not change with the parameters tuned. Nevertheless, challenges remain with discharge data uncertainty and parameter equifinality (Beven, 2006).

Recently, Gao et al. (2014) used a *mass balance approach* – more specifically, the mass curve technique – to estimate the root zone storage capacity at the catchment scale in the US and in Thailand. The underlying assumption is based on the tested hypothesis that plants will not root deeper than necessary (Milly and Dunne, 1994; Milly, 1994; Schenk, 2008). The water demand during the dry season equaled a constant transpiration rate, which was obtained through a water balance approach together with a normalised difference vegetation index (NDVI). Their results suggested that ecosystems develop their root zone storage capacity to deal with droughts with specific return periods, beyond which the costs of carbon allocation to roots are too high from the perspective of the plants. This resonates well with past economic analyses of plant behaviour and traits, e.g. Givnish (1986). Yet another mass balance approach was applied by de Boer-Euser et al. (2016) to catchments in New Zealand, using an interception and a root zone storage reservoir to record soil moisture storage deficit from variations in precipitation and transpiration. They derived mean annual transpiration from annual water balances, and seasonality of transpiration was added through estimate of potential transpiration and assumption about vegetation dormancy. The largest storage deficit of individual years were then used to derive catchment representative root zone storage capacity from Gumbel extreme value distribution assuming dry spell return periods of 10 years. These two applications of the mass balance approach have the advantage of being both model-independent and indirectly observation-based. In addition, no land-cover or soil information is needed, making the method parsimonious and flexible. Irrigation was, however, not considered and their assumption of ecosystem adaptation does not apply very well to seasonal crops (de Boer-Euser et al., 2016).

In a similar cumulative mass balance approach, van Dijk et al. (2014) combined a satellite evapotranspiration product with monthly precipitation data to estimate a 'mean seasonal storage range' (MSSR) at 250 m resolution across Australia, as one of the inputs into national-scale mapping of groundwater dependent ecosystems (`http://www.bom.gov.au/water/groundwater/gde/`). MSSR expresses the estimated mean seasonal range in the amount of water stored in all water stores combined (surface, soil and groundwater). A large range was considered likely to indicate a large use of water from storage during low rainfall periods from, for example, root water uptake from deeper soil or groundwater storages. Separate mapping of areas subject to irrigation or flood inundation was used to identify areas likely to rely on groundwater. The main conceptual drawback of this method is that the longer-term average seasonal pattern is likely to underestimate rooting depth in general, and even more so in regions without a strong seasonality in rainfall. The method also proved sensitive to any bias in evaporation and rainfall estimates and, in some conditions, simplifying assumptions about runoff and drainage rates (van Dijk et al., 2014).

5.1.2. RESEARCH AIMS

This study constitutes a first attempt to estimate global root zone storage capacity from satellite based evaporation and precipitation data using a mass balance approach, which is possible thanks to recent development, testing and validation of remote sensing evaporation products (e.g., Anderson et al., 2011; Guerschman et al., 2009; Hofste, 2014; Hu and Jia, 2015; Mu et al., 2011). Similar to the other mass balance based approaches, we assume that all hydrologically active roots are being used during the driest time and is not deeper than necessary. While we make use of the same mass balance principle as applied by Gao et al. (2014) and de Boer-Euser et al. (2016), our algorithm is based on indirect measurements of every unique pixel. Methodologically, in contrast to these two studies, the analyses here are carried out on global gridded data rather than by catchment and use total evaporation instead of interception and transpiration estimates.

Our aims are to: (1) present a method for estimating root zone storage capacity using remote sensing evaporation and precipitation data at global scale that includes the influence of irrigation; (2) evaluate how the new method influences evaporation simulation in a global hydrological model, in comparison to a classical look-up table approach; and (3) investigate the drought return periods different land-cover types adjust to. This study, thus, provides an earth observation-based and model-independent estimate of global root zone storage capacity that can be useful in models without the need for root distribution and soil information.

5.2. METHODS

5.2.1. ESTIMATING ROOT ZONE STORAGE CAPACITY

The root zone storage capacity S_R is estimated from soil moisture deficit D constructed from time series of water outflow F_{out} and inflow F_{in} from the root zone storage system. The algorithm is explained in this section and conceptually illustrated in Fig. 5.1.

First, we define the inflows and outflows from the system. The drying F_{out} of the system is the total daily evaporation E:

$$F_{out} = E. \tag{5.1}$$

Note that the total evaporation E is defined as the sum of transpiration, interception evaporation, soil moisture evaporation and open water evaporation.

The wetting F_{in} of the system is the total daily precipitation P and the effective irrigation water F_{irr} (i.e., additional evaporation from surface, wet soil, and ponding water at the tail end of irrigation borders that originates from irrigation):

$$F_{in} = P + F_{irr}. \tag{5.2}$$

We need the term F_{irr} in order to prevent S_R from becoming overestimated in irrigated regions. This is because irrigation is captured in satellite-based evaporation data, but obviously not in precipitation data. Without correction, the irrigation evaporation in the satellite evaporation data would erroneously contribute to accumulation of soil moisture deficit in our computations. Beside irrigation, additional evaporation from natural non-soil water storages (e.g, floodplains, wetlands, and groundwater) may contribute to overestimation of soil storage dynamics (see also Sect. 5.4.6). In regions (see Sect. 5.3.2)

where the annual accumulated evaporation exceeds annual accumulated precipitation, also the long term average of the difference of $E-(P+F_{\mathrm{irr}})$ is added to F_{in} in order to compensate for lateral inflow or estimation errors in evaporation or precipitation.

Second, the difference between inflow and outflow is calculated at the daily scale. The accumulated difference A is represented by the shaded areas in Fig. 5.1 and can be defined as

$$\underset{t_n \rightarrow t_{n+1}}{A} = \int_{t_n}^{t_{n+1}} F_{\mathrm{out}} - F_{\mathrm{in}} \mathrm{d}t, \tag{5.3}$$

where t_n is either the start of the accounting period or a point in time when $F_{\mathrm{out}} = F_{\mathrm{in}}$.

Third, we calculate the moisture deficit D, being the shortage of water from rainfall:

$$D(t_{n+1}) = \max\left(0, D(t_n) + \underset{t_n \rightarrow t_{n+1}}{A}\right). \tag{5.4}$$

The accumulation of D will occur in our algorithm only during periods where $F_{\mathrm{out}} > F_{\mathrm{in}}$, and reductions of D will occur when $F_{\mathrm{out}} < F_{\mathrm{in}}$. However, D never becomes negative by definition, since it can be considered a running estimate of the root zone storage reservoir size (see Fig. 5.1 at t_2). Not allowing negative D also means that any excess precipitation is assumed to be runoff or deep drainage. In this way, for every hydrological year, one maximum accumulated moisture deficit can be determined, representing the largest annual drought. A long time series of these maximum annual values creates the opportunity to study the return period of the maximum moisture deficits. Extreme values analysis, such as by Gumbel's method (Gumbel, 1935), then yield estimates of extreme moisture deficits with different probabilities of exceedance, see Sect. 5.2.3.

Finally, the root zone storage capacity (S_{R}) is defined as the maximum of the obtained D values:

$$\underset{t_0 \rightarrow t_{\mathrm{end}}}{S_{\mathrm{R}}} = \max\left(D(t_0), D(t_1), D(t_2), \ldots, D(t_{\mathrm{end}})\right). \tag{5.5}$$

S_{R} estimate based on an evaporation and precipitation time series would (in the absence of additional water supply) theoretically constitute a *minimum* root zone storage capacity, see Supplementary Fig. S1 in Wang-Erlandsson et al. (2016). If the root water uptake by plants does not abstract water until wilting point, the root zone storage may not utilise its full capacity. Note also that the S_{R} computed is not to be confused with time variable moisture availability. The time-variable water availability can be inferred from hydrological models using S_{R} as the water holding capacity.

During dry periods, the magnitude of surface runoff and deep drainage is usually small, and therefore is assumed to not affect root zone storage capacity calculations.

5.2.2. IMPLEMENTATION IN A HYDROLOGICAL MODEL

The newly derived root zone storage capacity is used in the global hydrological model STEAM (Wang-Erlandsson et al., 2014) to evaluate its influence on evaporation simulation.

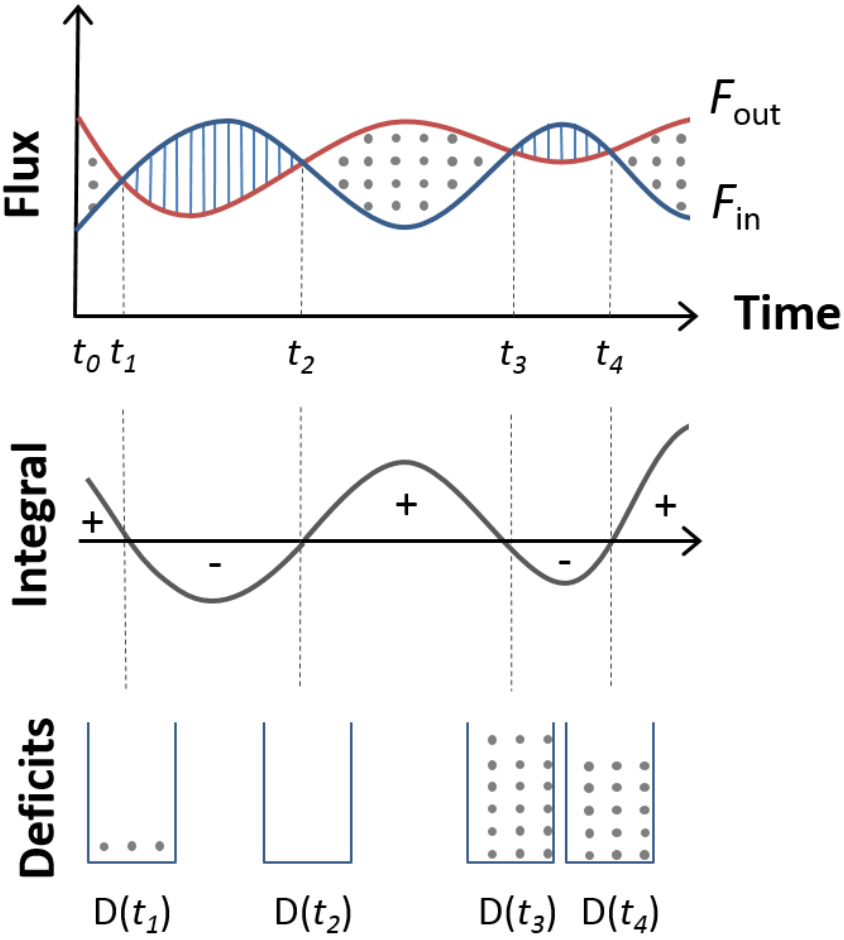

Figure 5.1: Conceptual illustration of the algorithm for calculating the root zone storage capacity S_R. The shaded areas represent the accumulated differences A that are positive when outflow F_{out} > inflow F_{in}, and negative when F_{out} < F_{in}. Moisture deficit D is increased by positive A and decreased by negative A. Note that D never becomes negative.

In STEAM, root zone storage capacity is originally calculated as the product of soil plant available water (depending on soil texture) and rooting depth (depending on land-cover type), using volumetric soil moisture as input to the stress function (here, the

formulation of van Genuchten (1980)):

$$f(\theta_{uz}) = \frac{\theta_{uz} - \theta_{uz,wp}}{\theta_{uz,fc} - \theta_{uz,wp}}, \tag{5.6}$$

where θ_{uz} is the actual volumetric soil moisture content (dimensionless), $\theta_{uz,wp}$ is the volumetric soil moisture content at wilting point, $\theta_{uz,fc}$ at field capacity.

However, the root zone storage capacity S_R is simply location-bound (depending on climatic variables alone) and no longer considered a land-cover and soil based parameter. Thus, to use S_R directly, we do not account for soil moisture below wilting point and assume $S_R = y_{uz}(\theta_{uz,fc} - \theta_{uz,wp})$, where y_{uz} is the rooting depth (m). The reformulated stress function of soil moisture becomes:

$$f(S_{uz}) = \frac{S_{uz}}{S_R}, \tag{5.7}$$

where S is the actual root zone storage (m). This reformulation is possible since the stress function retains its shape. Thus, S_R can in similar ways be implemented in other hydrological models.

To measure improvement, the root mean square error (ε_{RMS}) for simulated evaporation is calculated using the original look-up table based root zone storage capacity $S_{R,STEAM}$ and the newly derived root zone storage capacity $S_{R,new}$ (i.e., $S_{R,CRU-SM}$ or $S_{R,CHIRPS-CSM}$) respectively. The root mean square error improvement ($\varepsilon_{RMS,\,imp}$) is positive if the E simulated using S_R is closer to a benchmark evaporation data set than the E simulated using $S_{R,STEAM}$. The equation below shows the $\varepsilon_{RMS,imp}$ of $S_{R,new}$:

$$\varepsilon_{RMS,\,imp} = \varepsilon_{RMS}(E_{S_{R,STEAM}}, E_{benchmark}) - \varepsilon_{RMS}(E_{S_{R,new}}, E_{benchmark}).$$

The remote sensing based ensemble evaporation product E_{SM} (see Supplementary Fig. S7 in Wang-Erlandsson et al. (2016)) was used as benchmark $E_{benchmark}$. This use may seem circular when $E_{benchmark}$ is used to derive $S_{R,new}$, but is in fact valid due to differences in algorithms, precipitation input data, model types, and time span covered. First, the algorithms for estimating $S_{R,new}$, and for estimating E in STEAM are very different. While $S_{R,new}$ is derived based on the E overshoot over P, STEAM is a process-based model where evaporation originates from five different compartments, each constrained by potential evaporation and related stress functions. This means that it is impossible to reproduce $E_{benchmark}$ simply by inserting $S_{R,new}$ to STEAM. Second, the precipitation products (CRU and CHIRPS respectively) used for deriving $S_{R,new}$ differ from the precipitation forcing (ERA-I) used in STEAM. Third, $E_{benchmark}$ and STEAM are truly independent to each other as well. Whereas STEAM is process and water balance based, the ensemble E product is based on a combination of two (E_{SM}) or three (E_{CSM}) energy balance methods. Last, $S_{R,new}$ is based on a single year value of $E_{benchmark}$ (i.e., the year of maximum storage deficit), whereas the analyses of improvements are based on the entire available time series of 10-11 years. The only difference of the new STEAM simulations is the inclusion of updated information on root zone storage so that during longer periods of drought, more realistic estimations of continued evaporation processes can be expected. Thus, if $S_{R,new}$ dimensioned on one year of $E_{benchmark}$ nevertheless

improves E simulation in STEAM with regard to 10-11 years of $E_{\text{benchmark}}$ (i.e., the overall ϵ_{RMS} decreases when $S_{\text{R,new}}$ is used in STEAM) is a strong indication that the storage capacity correction was implemented for the right reason.

To investigate where the performance increases are most significant, improvements in mean annual, mean maximum monthly and mean minimum monthly E is calculated separately. $\epsilon_{\text{RMS,imp}}$ by climate are done for bins of precipitation seasonality index and aridity index (defined in Sect. 5.2.4) containing more than 200 grid cells. $\epsilon_{\text{RMS,imp}}$ by land-cover types are analysed for grid cells where single land-cover occupancy exceeds 90 % in a 1.5° grid cell. ϵ_{RMS} analyses are carried out on area weighted evaporation values to avoid bias caused by differences in grid cell areas. Results are shown in Sect. 5.4.4.

5.2.3. FREQUENCY ANALYSIS

We calculate S_{R} for 10 to 11 years (2003–2012 and 2003–2013 respectively, see Sect. 5.3.1) depending on data availability. However, different ecosystems may adapt their root system depths to different return periods of drought which may or may not correspond to the available data time series length. Thus, we also determine the $S_{\text{R},L\text{ yrs}}$ for different return periods of drought L (see Sect. 5.4.4) based on Gumbel's distribution (Gumbel, 1935). The resulting $S_{\text{R},L\text{ yrs}}$ is a function of the mean and standard deviation of the extremes in the data series:

$$S_{\text{R},L\text{ yrs}} = \overline{S_{\text{R}}} + \frac{\sigma_{S_{\text{R}}}}{\sigma_n}\left(y_L - y_n\right), \tag{5.8}$$

where y_n is the reduced mean as a function of the number of available years n (y_{10} = 0.4952 and y_{11} = 0.4996), σ_n is the reduced standard deviation as a function of n (σ_{10} = 0.9496 and σ_{11} = 0.9676), $\sigma_{S_{\text{R}}}$ is the standard deviation of S_{R}, while y_L is the reduced variate of the Gumbel distribution:

$$y_L = -\ln\left(-\ln\left[1 - \frac{1}{L}\right]\right). \tag{5.9}$$

5.2.4. CLIMATIC INFLUENCE OF LAND-COVER TYPE

We analyse how $S_{\text{R,CRU-SM}}$ of different land-cover types can be associated with climatic indicators. Stepwise multiple regression method based on the Akaike information criterion (AIC) is used to analyse how these climatic indicators may explain variations in S_{R} within a land-cover type. The climatic indicators used are precipitation seasonality (I_{s}), aridity (I_{a}), and interstorm duration (I_{isd}) (as these were found to be important by Gao et al. (2014)):

$$I_{\text{S}} = \frac{1}{P_{\text{a}}} \sum_{\text{m}=1}^{m=12} \left| \overline{P_{\text{m}}} - \frac{\overline{P_{\text{a}}}}{12} \right|, \text{ and} \tag{5.10}$$

$$I_{\text{a}} = \frac{\overline{P_{\text{a}}}}{\overline{E_{\text{p}}}}, \tag{5.11}$$

where $\overline{P_{\text{m}}}$ is the mean precipitation of the month, $\overline{P_{\text{a}}}$ is the mean annual precipitation, and $\overline{E_{\text{p}}}$ is the potential evaporation. We defined I_{isd} as the mean continuous number of days per year without precipitation. Interaction effects between the variables are taken into account.

Table 5.1: Overview of the time period, latitudinal coverage and data input for the two root zone storage capacity S_R datasets ($S_{R,CHIRPS\text{-}CSM}$ and $S_{R,CRU\text{-}SM}$) produced in this study.

	$S_{R,CHIRPS\text{-}CSM}$	$S_{R,CRU\text{-}SM}$
Years	2003–2012	2003–2013
Latitude coverage	50° N–50° S	80° N–56° S
Monthly P data input	CHIRPS	CRU
Monthly E data input	Mean of CMRSET, SSEBop, and MOD16 (E_{CSM})	Mean of SSEBop and MOD16 (E_{SM})
Monthly irrigation data input	LPJmL (2003–2009)	LPJmL (2003–2009)
Daily E and P data for downscaling	ERA-I	ERA-I

5.3. DATA

5.3.1. EVAPORATION AND PRECIPITATION INPUT FOR ESTIMATING S_R

We present two S_R datasets, one covering the latitudes 50° N–50° S ($S_{R,CHIRPS-CSM}$), and one with global coverage 80° N–56° S ($S_{R,CRU-SM}$). See Table 1 for an overview of the data input for each S_R dataset.

For the clipped 50° N–50° S $S_{R,CHIRPS-CSM}$ map, we matched the 0.05° USGS Climate Hazards Group InfraRed Precipitation with Stations (CHIRPS) precipitation data (P_{CHIRPS}) (Funk et al., 2014) with the ensemble mean of three satellite-based global scale evaporation datasets (E_{CSM}): the CSIRO MODIS Reflectance Scaling EvapoTranspiration (CMRSET) v1405 at 0.05° (Guerschman et al., 2009), the Operational Simplified Surface Energy Balance (SSEBop) at 30″ (Senay et al., 2013), and the MODIS evapotranspiration (MOD16) at 0.05° (Mu et al., 2011). These three different evaporation models are all based on MODIS satellite data, but they use different parts of the electro-magnetic spectrum. CMRSET combines a vegetation index, which estimates vegetation photosynthetic activity, and shortwave infrared spectral data to estimate vegetation water content and presence of standing water. SSEBop relies on the thermal infrared data for determination of the latent heat flux and MOD16 on the visible and near-infrared data to account for Leaf Area Index variability. Hence, their input data, model structure and output data are not necessarily similar, which makes them attractive for deriving an ensemble evaporation product. $S_{R,CHIRPS-CSM}$ is based on data covering the years 2003–2012 as CMRSET was not available for 2013.

For the global coverage $S_{R,CRU-SM}$ map, we used the 0.5° Climatic Research Unit Timeseries version 3.22 (CRU TS3.22) precipitation data (P_{CRU}) (Harris et al., 2014) together with the ensemble mean (E_{SM}) of only SSEBop and MOD16, since we found CMRSET to overestimate evaporation at high latitudes, possibly due to the effect of snow cover on estimates. In addition, the irrigation effect was analysed for $S_{R,CRU-SM}$ by including evaporation originating from irrigation water simulated at 0.5° and at the daily scale by the dynamic global vegetation model LPJmL (Jägermeyr et al., 2015). $S_{R,CRU-SM}$ is computed based on evaporation data covering the years 2003–2013. Irrigation data cover the years 2003–2009 (monthly mean irrigation evaporation were used for years after 2009).

We present $S_{R,CHIRPS-CSM}$, because P_{CHIRPS} is the lead precipitation product and we can make use of three evaporation datasets. However, P_{CHIRPS} is unfortunately not available at the global scale, and CMRSET is not reliable in high latitudes. Thus, we added the global scale $S_{R,CRU-SM}$ to this study. This allows for application in global scale models

as well as investigations at the global scale (e.g., climate and land-cover based analyses).

The input precipitation and evaporation data are shown in Figs. 5.2 and S2 in Supplementary Information of Wang-Erlandsson et al. (2016). This study required global coverage data at a grid cell resolution for both evaporation and precipitation. Importantly, these products must not be produced using assumptions on root zone storage capacity, to prevent circularity (since we are estimating root zone storage capacity). In other words, there should be no water balance type of computation process involved in the determination of S_R. We used satellite-based evaporation products because they are the only options available that fulfill these criteria, (i.e., reanalyses and land surface model evaporation contain soil depth information, whereas FLUXNET data are too sparse for acquiring consistently good quality global coverage). The monthly satellite-based evaporation data used in the manuscript were those available at the time of this research. Conversely, precipitation data do not need to be satellite-based, but can also be ground-based. Inter-comparisons of precipitation products show that both CRU and CHIRPS are good quality precipitation products. In particular, CHIRPS performance stands out in a comprehensive inter-comparison of 13 difference precipitation products in the Nile basin (Hessels, 2015). Nevertheless, data uncertainties still persist. The mean annual accumulated evaporation of E_{CSM} and E_{SM} is sometimes higher than the mean annual accumulated precipitation P_{CHIRPS} and P_{CRU}, which is discussed in Sect. 5.3.2. The use of three evaporation datasets decreases uncertainties related to individual evaporation products, because there is simply not one single preferred model. To compare the effect of different input data, we also present results of S_R based on the separate evaporation and precipitation data (Supplementary Figs. S4 and S5, Wang-Erlandsson et al. (2016)).

In addition, ECMWF re-analysis interim (ERA-I) (Dee et al., 2011) daily 0.5° evaporation and precipitation data were used to temporally downscale the monthly evaporation and precipitation data. In the temporal downscaling, we first established the ratios between daily values to the mean monthly ERA-I, and second, used the relationship to estimate daily values from monthly E_{SM} or E_{CSM} values. This allows daily products of evaporation and precipitation, which was necessary in order to incorporate also short drought periods.

5.3.2. EVAPORATION EXCEEDANCE OVER PRECIPITATION

The mean annual accumulated evaporation of E_{CSM} and E_{SM} is sometimes higher than the mean annual accumulated precipitation P_{CHIRPS} and P_{CRU} (see Fig. 5.3). In these areas, overestimation of S_R may be expected, because it is unlikely that the 10 or 11 year accumulation of E is more than rainfall, except for hydrological situations with lateral inflow through inundation, irrigation or groundwater inflow. The evaporation dataset E_{CSM} exhibits larger and more widely spread exceedance over P_{CHIRPS} in comparison to the $E_{SM} - P_{CRU}$ combination. Most notably, the exceedance is high and potentially spurious in arid and semi-arid zones (e.g., the Sahara, western US, and Central Asia) which suggests that the evaporation from deserts is not accurate. Regions where both $S_{R,CRU-SM}$ and $S_{R,CHIRPS-CSM}$ show high accumulated evaporation exceedance are along the Andes, patches in western US, East Africa, Ivory Coast, Central Asia, Northwest China and spots in Australia. These are essentially irrigated areas, lakes, reservoirs, wetlands and coastal deltas. Possibly, overestimation of S_R can also be caused for example by vegetation

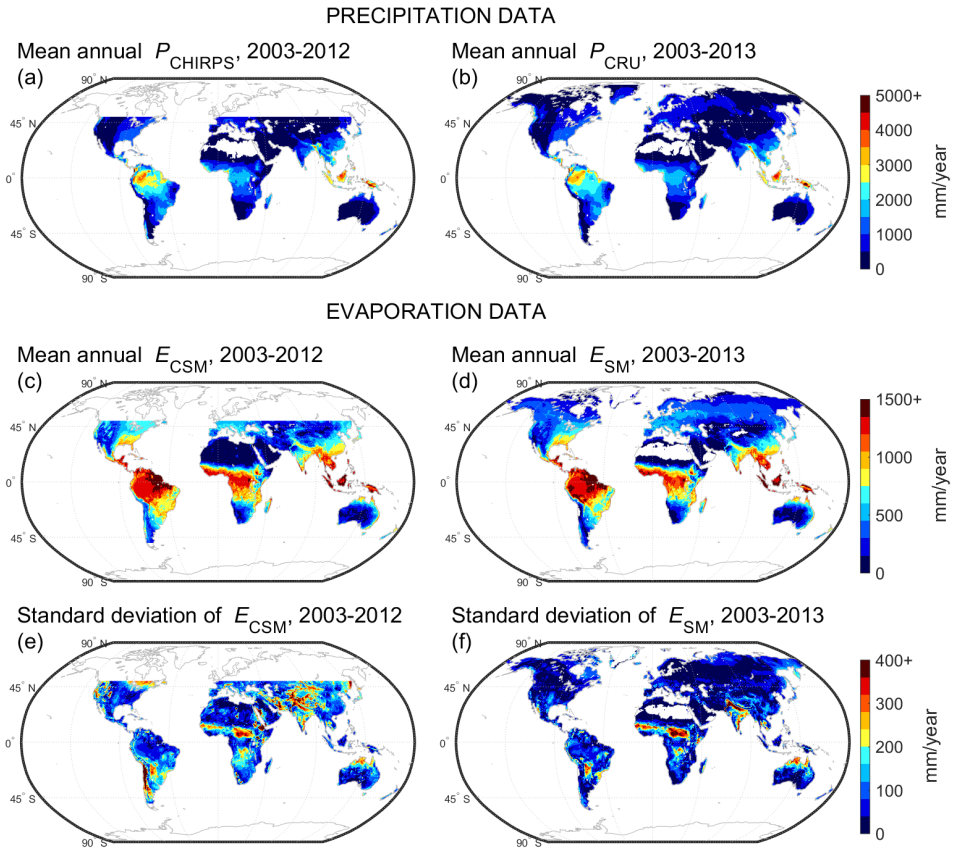

Figure 5.2: The mean annual precipitation of **(a)** CHIRPS (P_{CHIRPS}) for the years 2003–2012 (50° N–50° S), and **(b)** CRU (P_{CRU}) for the years 2003–2013 (80° N–56° S). The mean annual ensemble evaporation of **(c)** CMRSET, SSEBop and MOD16 (E_{CSM}) for the years 2003–2012 (50° N–50° S), and **(e)** SSEBop and MOD16 (E_{SM}) for the years 2003–2013 (80° N–56° S). Standard deviation of ensemble evaporation of **(e)** E_{CSM}, and **(f)** E_{SM}. Values below 0.5 % of the maximum are displayed as white.

tapping into groundwater. Uncertainty in evaporation and precipitation products also propagates to errors in S_R. The uncertainty of evaporation is location specific, (grid cells with a large standard deviation between the individual E products are shown in Fig. 5.2e and f).

Interestingly, the high evaporation exceedance appears to be much more pronounced during drier years. In Fig. 5.4, we sort every grid cell by the annual precipitation amount, from dry to wet, and plot the mean latitudinal E exceedance for the regions where the long term accumulated $E - P$ is positive. The figure clearly shows that E exceedance decreases with increase in rainfall, indicating that increased water demand during dry years is satisfied by withdrawing moisture from the soil matrix that is bounded with more potential

(higher pF), or from underlying groundwater through deeply rooting vegetation.

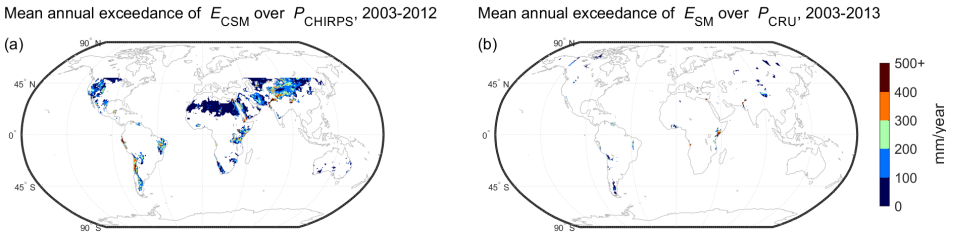

Figure 5.3: Mean annual accumulated exceedance of **(a)** E_{CSM} (ensemble evaporation of CMRSET, SSEBop, and MOD16) over P_{CHIRPS}, and **(b)** E_{SM} (ensemble evaporation of SSEBop, and MOD16) over P_{CRU}.

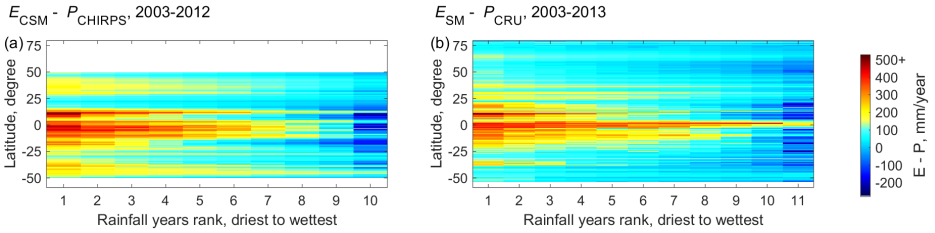

Figure 5.4: Mean latitudinal difference between **(a)** E_{CSM} (ensemble evaporation of CMRSET, SSEBop, and MOD16) and P_{CHIRPS} (CHIRPS precipitation), and **(b)** E_{SM} (ensemble evaporation of SSEBop, and MOD16) and P_{CRU} (CRU precipitation) sorted from the driest to the wettest years. The figure only includes regions where accumulated $E - P$ over the entire available time series (2003–2012 and 2003–2013 respectively) are positive.

5.3.3. OTHER DATA USED IN ANALYSES

The following datasets were compared with our S_R estimates:

- the estimated 1° rooting depth for 95 % of the roots from Schenk and Jackson (2009);
- the 1° rooting depth estimated by the optimised inverse modelling from Kleidon (2004), (where the minimum rooting depth producing the long-term maximum net primary production is selected as the best estimate);
- the 1° rooting depth estimated by the assimilated inverse modelling from Kleidon (2004), (where the rooting depth that minimises the difference between the modelled and the satellite-derived absorbed photosynthetically active radiation is selected as the best estimate); and
- the root zone storage capacity look-up table based parametrisation used in a global hydrological model, i.e., the Simple Terrestrial Evaporation to Atmosphere Model (STEAM) (Wang-Erlandsson et al., 2014).

In order to enable comparison between rooting depth y_{uz} and root zone storage capacity S_R, we assumed that the root zone reaches its wilting point and converted between y_{uz} and S_R using soil properties:

$$S_R = h\theta_{paw} = h\left(\theta_{uz,fc} - \theta_{uz,wp}\right), \tag{5.12}$$

where θ_{paw} is the maximum plant available soil moisture, $\theta_{uz,fc}$ is the volumetric soil moisture content at field capacity and $\theta_{uz,wp}$ is the volumetric soil moisture content at wilting point. Soil texture data at 30″ is taken from the Harmonised World Soil Database (HWSD) (FAO/IIASA/ISRIC/ISSCAS/JRC, 2012), and field capacity and wilting point information is based on the United States Department of Agriculture (USDA) soil classification (Saxton and Rawls, 2006).

To analyse if and how the inferred S_R may improve simulations in a hydrological model, we applied $S_{R,CRU-SM}$ to the evaporation simulation model STEAM (see Chapter 2 for model description and data input). To analyse the improvements in simulated evaporation by using $S_{R,CRU-SM}$ as input to STEAM (see Sect. 5.4.3), we used an aridity index based on precipitation and reference evaporation from CRU TS3.22 (Harris et al., 2014).

For land-cover based analyses, we used the 0.05° Land Cover Type Climate Modeling Grid (CMG) MCD12C1 created from Terra and Aqua Moderate Resolution Imaging Spectroradiometer (MODIS) data (Friedl et al., 2010) for the year 2008, based on the land-cover classification according to the International Geosphere – Biosphere Programme (IGBP) (shown in Supplementary Fig. S3 in Wang-Erlandsson et al. (2016)). Land-cover fractions are preserved in upscaling to 0.5°. Only 0.5° grid cells containing at least 95 % of a single land-cover type are used in the land-cover based analyses (see Sect. 5.4.2) and grid cells containing at least 95 % water are removed from all S_R analyses.

In the analysis of contrasting climatic influence from different land-cover types (see Sect. 5.2.4), the climate variables interstorm duration, aridity and precipitation seasonality are developed based on monthly 0.5° reference evaporation from CRU TS3.22 (Harris et al., 2014) and monthly 0.5° precipitation for 1982–2009 from the Global Precipitation Climatology Centre (GPCC) (Schneider et al., 2011). Here, GPCC data (instead of CRU) are used in order to prevent false correlation with the CRU-based $S_{R,CRU-SM}$.

Data with finer resolution than 0.5° have been upscaled to 0.5° by simple averaging (i.e., assuming that the value of a 0.5° grid cell correspond to the mean of the overlapping finer grid cell values). Data with coarser resolution than 0.5° were downscaled by oversampling (i.e., transferring grid cell values assuming that the finer 0.5° grid cell values correspond to those overlapped by the coarser degree grid cell values).

5.4. RESULTS AND DISCUSSION

5.4.1. ROOT ZONE STORAGE CAPACITY ESTIMATES

Figure 5.5 shows the $S_{R,CHIRPS-CSM}$ (clipped, based on E_{CSM} and P_{CHIRPS}) and $S_{R,CRU-SM}$ (global, based on E_{SM} and P_{CRU}) estimates adjusted for irrigation, (provided in the Supplements in Wang-Erlandsson et al. (2016) as ASCII-files). Independent of the input data used, large root zone storage capacities are observed in the semi-arid Sahel, South American and African savannah, central US, India, parts of Southeast Asia, and northern

Australia. The lowest root zone storage capacities are observed in the most arid and barren areas, and in the humid and densely-vegetated tropics. The largest differences between $S_{R,CHIRPS-CSM}$ and $S_{R,CRU-SM}$ are observed over the Amazon, along the Andes, in Central Asia, and in the Sahara. Along mountain ridges (for example along the Andes and Himalaya), the S_R estimates are generally large, possibly due to data uncertainty in these transition regions or evaporation in foothills sustained by lateral water fluxes from the mountains in addition to precipitation. The positive values of $S_{R,CHIRPS-CSM}$ in the Sahara desert are caused by overestimation of evaporation in the CMRSET evaporation product, (see also Supplementary Figs. S4 and S5 in Wang-Erlandsson et al. (2016)).

Notably, Fig. 5.5 shows contrasting root zone storage capacity over the South American and African tropical forests, although they belong to the same ecological class (i.e., evergreen broadleaf forests). This variability is purely due to temporal fluctuations between precipitation and evaporation and is independent of soil properties.

5.4.2. COMPARISON TO OTHER ROOT ZONE STORAGE CAPACITY ESTIMATES

GEOGRAPHIC COMPARISON

Figure 5.6 shows root zone storage capacity estimates (directly determined or converted from rooting depth, see Sect. 5.3.3) from other studies and compares them to $S_{R,CRU-SM}$. The estimates shown are based on: rooting depths containing 95 % of all roots from Schenk and Jackson (2009) ($S_{R,Schenk}$, Fig. 5.6a), hydrologically active rooting depth from inverse modelling (Kleidon, 2004) using the optimisation ($S_{R,Kleidon,O}$, Fig. 5.6c) and assimilation approach ($S_{R,Kleidon,A}$, Fig. 5.6e), and from a literature-based look-up table used in the hydrological model STEAM ($S_{R,STEAM}$, Fig. 5.6g) (Wang-Erlandsson et al., 2014).

When the different datasets are compared to $S_{R,CRU-SM}$ (Fig. 5.6b, 5.6d, 5.6f and 5.6h), we see both agreements and significant differences. All datasets appear to more or less agree on the approximate range of root zone storage capacity in large parts of the Northern Hemisphere. Around the Equator, all datasets indicate root zone storage capacity to be lower or similar to that of $S_{R,CRU-SM}$ in the tropical forests of the Amazon and the Indonesian islands. In the Congo region and in Central America, $S_{R,Kleidon,O}$ and $S_{R,Kleidon,A}$ are larger than both $S_{R,CRU-SM}$ and the other. In the south temperate zone, $S_{R,CRU-SM}$ appear to correspond to or be lower than the other datasets.

Figure 5.6 also reveal patterns specific to the different datasets that can be explained by the underlying method used for estimating rooting depth or root zone storage. For example, both $S_{R,Schenk}$ and $S_{R,STEAM}$ contain spuriously large values in the deserts (such as the Sahara and the Gobi) where vegetation is non-existent or extremely sparse. The methods based on satellite data ($S_{R,CRU-SM}$, $S_{R,Kleidon,O}$ and $S_{R,Kleidon,A}$) appear to reflect reality in deserts more accurately. The $S_{R,Kleidon,O}$ presents the largest root zone storage capacities (most pronounced over Africa, India, parts of South America), since this dataset represent an idealised and optimised case. On the contrary, the smallest root zone storage capacities are presented in the Amazon rainforest by $S_{R,Schenk}$. These smaller values could be due to the lack of observations, since $S_{R,Schenk}$ is derived from rooting depth field measurements. But any difference between rooting depth and root zone storage capacity could also be due to discrepancies between actual rooting depth and hydrologically active rooting depth (see also Sect. 5.3.3). In contrast to the other datasets, $S_{R,STEAM}$ is relatively homogenous and does not contain any large values (basically all < 400 mm) (Fig. 5.6g).

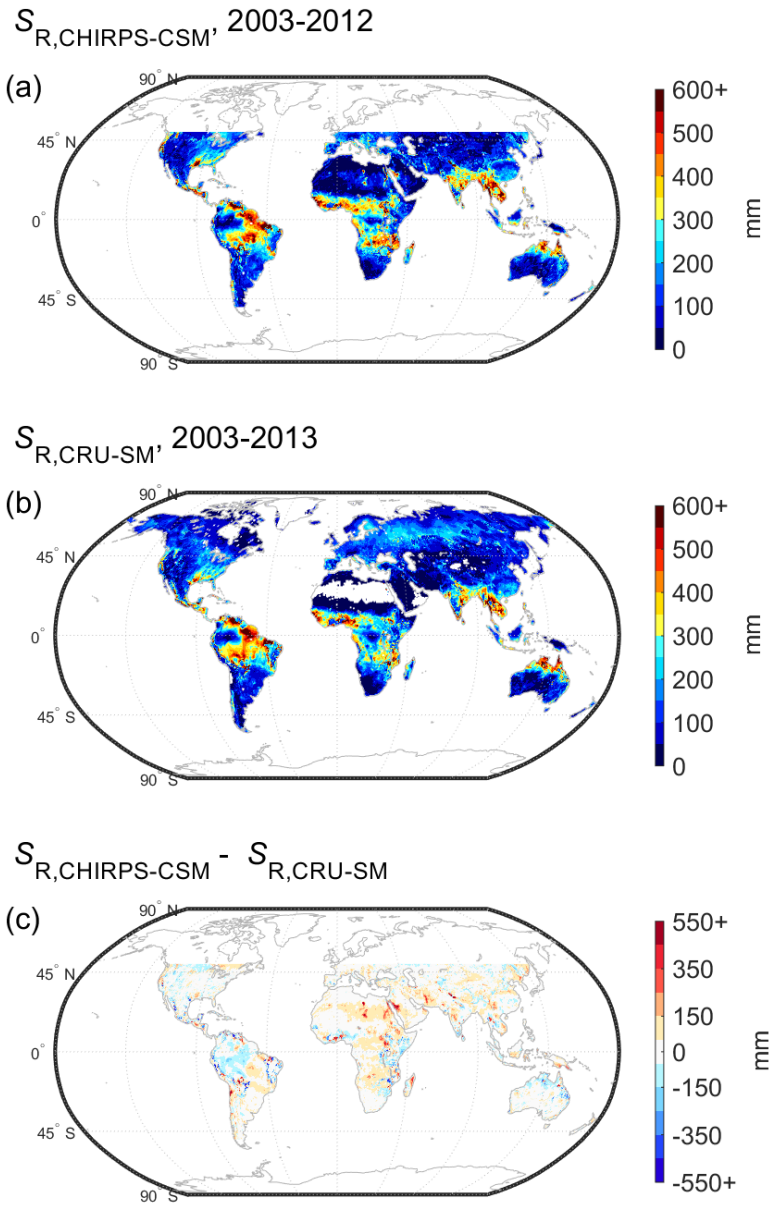

Figure 5.5: Root zone storage capacity estimates of **(a)** $S_{R,CHIRPS-CSM}$ (based on P_{CHIRPS} and E_{CSM}), **(b)** $S_{R,CRU-SM}$ (based on P_{CRU} and E_{SM}), and **(c)** the difference between $S_{R,CHIRPS-CSM}$ and $S_{R,CRU-SM}$. Values below 0.5 % of the maximum in (a) and (b) are displayed as white.

This is natural, since the other datasets are based on more heterogeneous observations, whereas $S_{R,STEAM}$ is based on a homogenous look-up table. Nevertheless, different input data were also used in the different studies. Thus, it is difficult to attribute the variations in root zone storage capacity estimates to differences in methods or differences in input data. Additional comparisons in scatter plots and root mean square error are shown in Supplementary Fig. S6 and Table S2 in Wang-Erlandsson et al. (2016).

DISTRIBUTION BY LAND-COVER TYPE

Figure 5.7 shows the root zone storage capacity distribution for different land cover types and S_R datasets, ($S_{R,CHIRPS-CSM}$ is not shown since it does not have global coverage). Except for deciduous broadleaf forests, the $S_{R,CRU-SM}$ of forests (Fig. 5.7a–e) are closer to $S_{R,Kleidon,O}$ and $S_{R,Kleidon,A}$ than to $S_{R,Schenk}$. Interestingly, the range of S_R is large in the evergreen forest types for the "adaptive" estimates ($S_{R,CRU-SM}$, $S_{R,Kleidon,O}$, and $S_{R,Kleidon,A}$), but small for the literature based methods ($S_{R,Schenk}$ and $S_{R,STEAM}$). In open shrublands and grasslands (Fig. 5.7f and i) root zone storage capacities are similar across all estimates, except for the higher $S_{R,STEAM}$. In savannahs, croplands, and natural/vegetation mosaic areas (Fig. 5.7h, j, k), $S_{R,Kleidon,O}$, and $S_{R,Kleidon,A}$ appear to have higher values than others. In woody savannahs (Fig. 5.7g), $S_{R,Kleidon,O}$ has a notably large range as well as high mean root zone storage capacity. In barren land (Fig. 5.7l), $S_{R,Schenk}$ and $S_{R,STEAM}$ are counter-intuitively high.

5.4.3. IMPLEMENTATION IN A HYDROLOGICAL MODEL

We implemented $S_{R,CRU-SM}$, $S_{R,CHIRPS-CSM}$, and $S_{R,STEAM}$ in the hydrological model STEAM (see Sect. 5.2.2 for methods) in order to analyse how the new root zone storage capacities might improve model performance. This section shows the performance analyses using $S_{R,CRU-SM}$ as input, since it has global coverage. A comparison in E simulation performance between using $S_{R,CHIRPS-CSM}$ and $S_{R,CRU-SM}$ as input to STEAM is shown and discussed in the Supplementary Information of Wang-Erlandsson et al. (2016).

Figure 5.8 compares the STEAM-simulated evaporation when using, on the one hand, $S_{R,CRU-SM}$ and, on the other, the look-up table based $S_{R,STEAM}$. In general, $S_{R,CRU-SM}$ estimated higher evaporation rates in the tropics and lower evaporation in the subtropics and temperate zone. In particular, the differences are pronounced during the warm and dry seasons. For example, the evaporation reductions with $S_{R,CRU-SM}$ is widespread in the Northern Hemisphere during July. During the dry seasons (e.g., January in the Sahel, July in Congo south of the Equator), the evaporation increase is the most significant. Moreover, the changes in evaporation also depend on land-cover type. In South America, evaporation increases in the seasonal tropical forests of the Amazon, whereas evaporation decreases in the savannas and shrublands in the south. These results suggest that $S_{R,CRU-SM}$ has the greatest potential to influence model simulations for the hot and dry seasons, in regions where the root zone storage varies strongly.

Figure 5.9 shows the ε_{RMS} improvements of simulated mean annual, mean maximum monthly and mean minimum monthly E sorted by seasonality and aridity, using $S_{R,CRU-SM}$ as input and E_{SM} as benchmark. The analysis reveals that our $S_{R,CRU-SM}$ estimate has the greatest potential to improve model simulations for minimum monthly

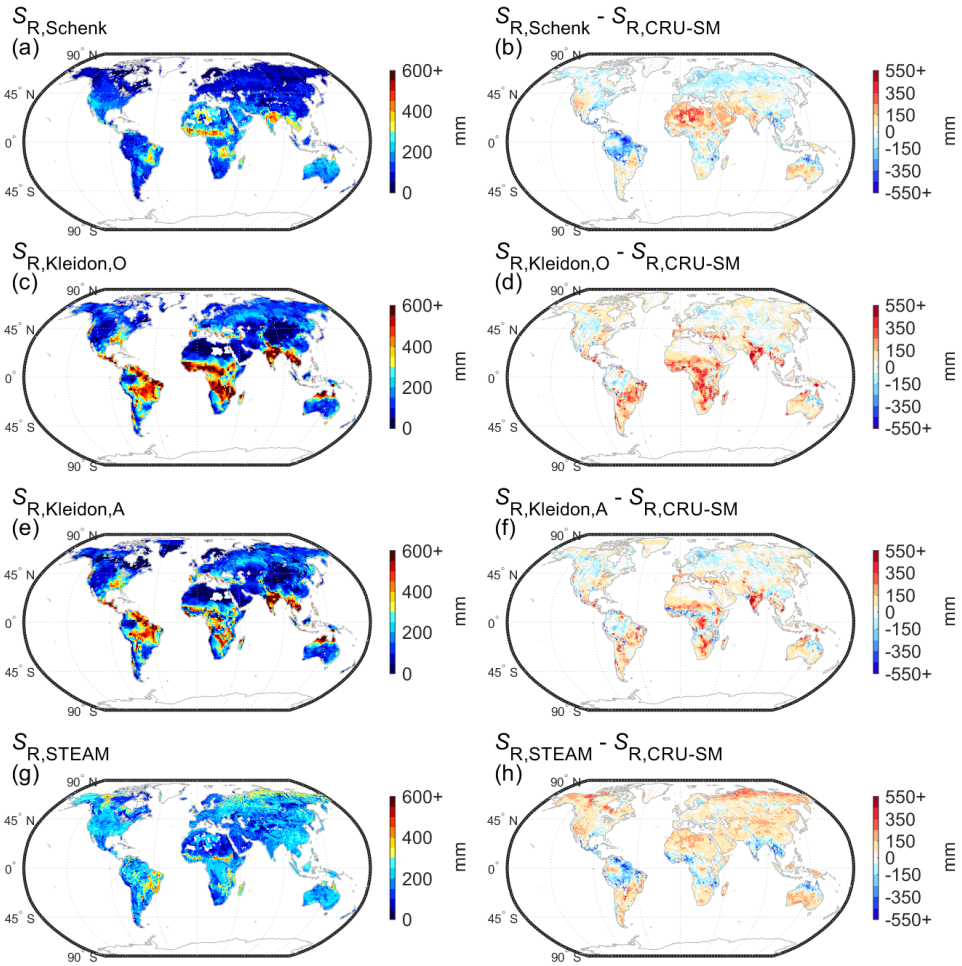

Figure 5.6: Root zone storage capacities of **(a)** $S_{R,Schenk}$ (Schenk and Jackson, 2009), **(c)** $S_{R,Kleidon,O}$ (Kleidon, 2004), **(e)** $S_{R,Kleidon,A}$ (Kleidon, 2004), **(g)** $S_{R,STEAM}$ (based on look-up table in Wang-Erlandsson et al. (2014)) and **(b, d, f, h)** their differences with $S_{R,CRU-SM}$ (estimated based on E_{SM} and P_{CRU} in this study). Values below 0.5 % of the maximum in (a), (c), (e), and (g) are displayed as white.

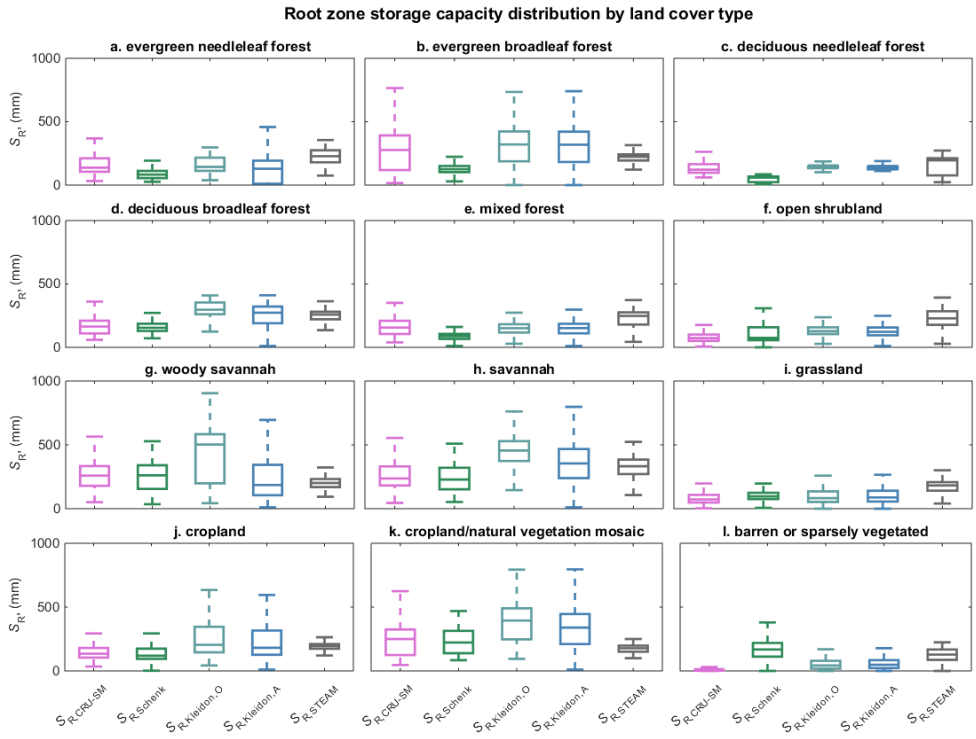

Figure 5.7: Comparison of root zone storage capacity estimates by land-cover type using Tukey boxplots. The central markers of the boxes mark the median, and the box edges mark the 25th and 75th percentile. The whiskers extend to 1.5 times the interquartile range.

evaporation. In particular, the improvements become significant with increased seasonality of rainfall, and in subhumid to humid regions, resonating the findings of de Boer-Euser et al. (2016).

5.4.4. THE EFFECT OF DIFFERENT DROUGHT RETURN PERIODS

Vegetation may adapt to a different time period than the 10–11 years of data that were available for this study. Thus, we normalised S_R using the Gumbel distribution in order to assess the effect of different drought return periods (see Sect. 5.2.3). Normalised S_R are provided in the Supplements as ASCII-files (see online material of Wang-Erlandsson et al. (2016)).

Figure 5.10 shows the mean latitudinal $S_{R,CHIRPS-CSM,L\ yrs}$ and $S_{R,CRU-SM,L\ yrs}$ for different drought return periods L based on the Gumbel distribution. As may be expected, both $S_{R,CHIRPS-CSM}$ and $S_{R,CRU-SM}$ based on the 10–11 years where data were available correspond most closely to the $S_{R,L\ yrs}$ for $L = 10$ years ($S_{R,10\ yrs}$). $S_{R,L\ yrs}$ always increases with L, but more strongly for small L and less so for large L following the Gumbel distribution. The largest spans are seen in the northern latitudes and around the equator.

Figure 5.11 shows a comparison of how Gumbel normalised $S_{R,CRU-SM,L\ yrs}$ affect

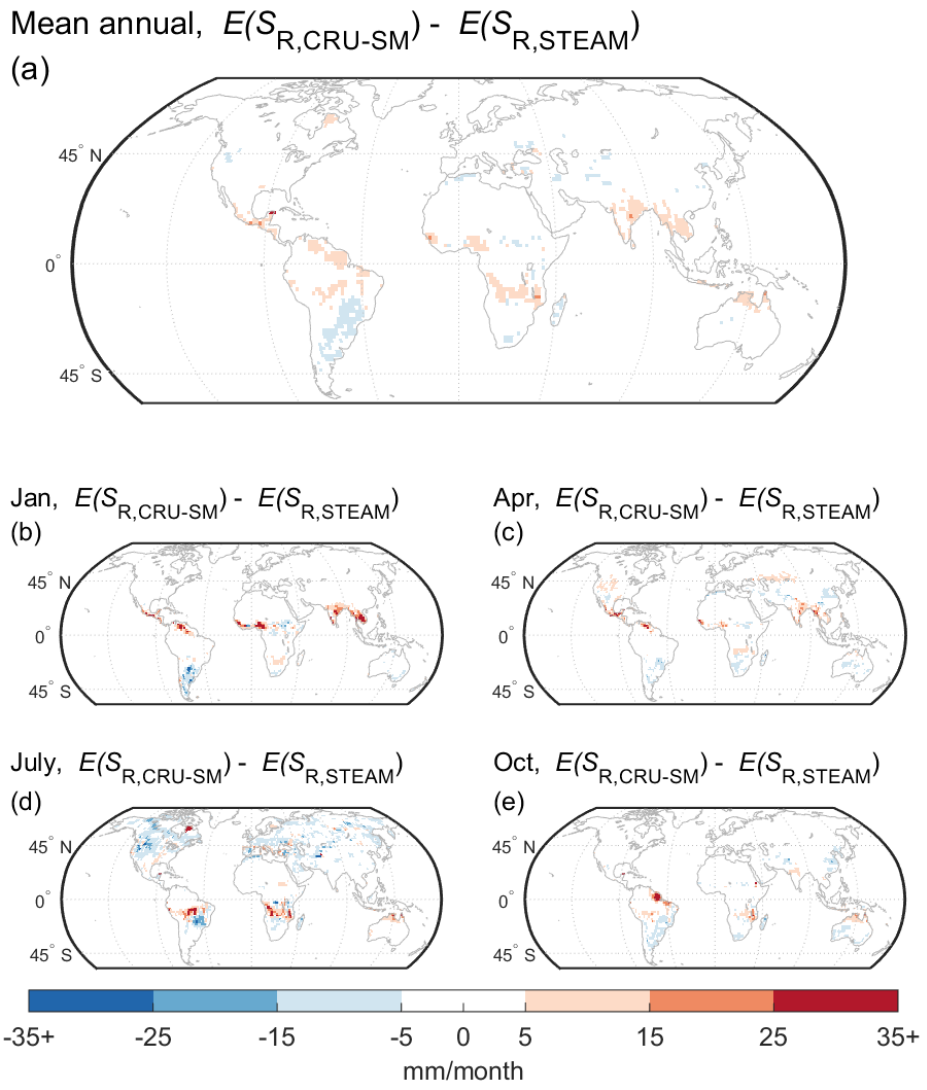

Figure 5.8: Difference in STEAM-simulated evaporation between using $S_{R,CRU-SM}$ (estimated based on E_{SM} and P_{CRU} in this study) and $S_{R,STEAM}$ (based on look-up table in Wang-Erlandsson et al. (2014)) as root zone storage capacity parametrisation at **(a)** mean annual scale and averages for the months of **(b)** January, **(c)** April, **(d)** July, and **(e)** October over the time period 2003–2013. See also Sect. 5.4.3.

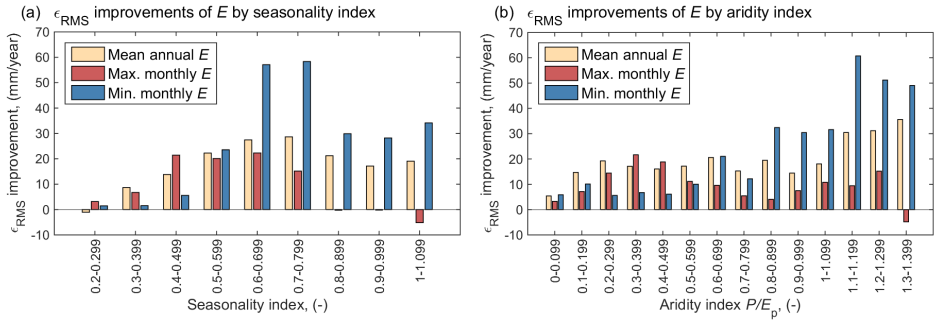

Figure 5.9: The improvement in root mean square error (ϵ_{RMS}) in simulated mean monthly evaporation E by implementing $S_{R,CRU-SM}$ (estimated based on E_{SM} and P_{CRU} in this study) instead $S_{R,STEAM}$ (based on look-up table in Wang-Erlandsson et al. (2014)) in the global hydrological model STEAM. The improvements in mean annual, mean maximum monthly and mean minimum monthly E (over the years 2003–2013) are sorted by **(a)** precipitation seasonality index and **(b)** aridity index (defined in Sect. 5.2.4). The satellite based ensemble evaporation based on SSEBop and MOD16 (E_{SM}) was used as the benchmark for improvements, (see methods described in Sect. 5.2.2). Only bins containing a minimum of 200 grid cells are shown.

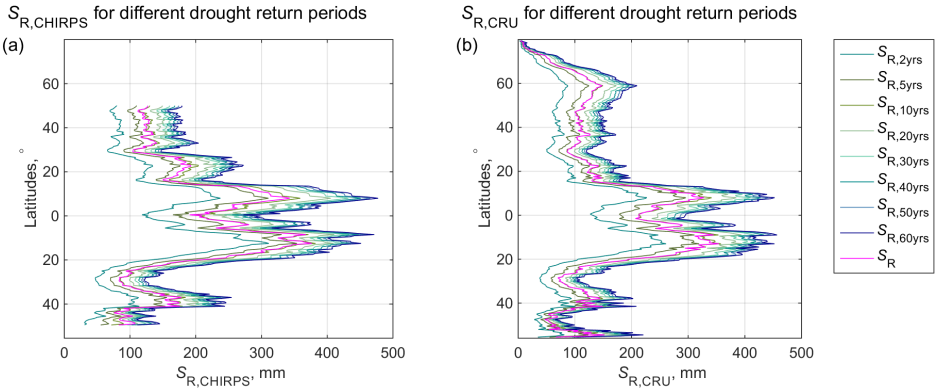

Figure 5.10: Mean latitudinal root zone storage capacity **(a)** $S_{R,CHIRPS-CSM}$ (based on P_{CHIRPS} and E_{CSM}) and **(b)** $S_{R,CRU-SM}$ (based on P_{CRU} and E_{SM}) dimensioned by drought return periods between 2 and 60 years estimated using Gumbel distribution (see methods described in Sect. 5.2.3).

the evaporation simulation ϵ_{RMS} improvements by land-cover type. Interestingly, a drought return period of 2 years ($S_{R,CRU-SM,2\ yrs}$) offers the best evaporation simulation performance in deciduous broadleaf forests, open shrublands, grasslands, croplands and barren lands, whereas $S_{R,CRU-SM,10\ yrs}$ or $S_{R,CRU-SM,20\ yrs}$ are best in evergreen needleleaf forests, woody savannahs, and savannahs, and $S_{R,CRU-SM,60\ yrs}$ is best in evergreen broadleaf forests, deciduous needleleaf forests, and mixed forests.

A short drought return period of 2 years improves evaporation simulation the most in short vegetation types probably because these land-cover types adapt to average years

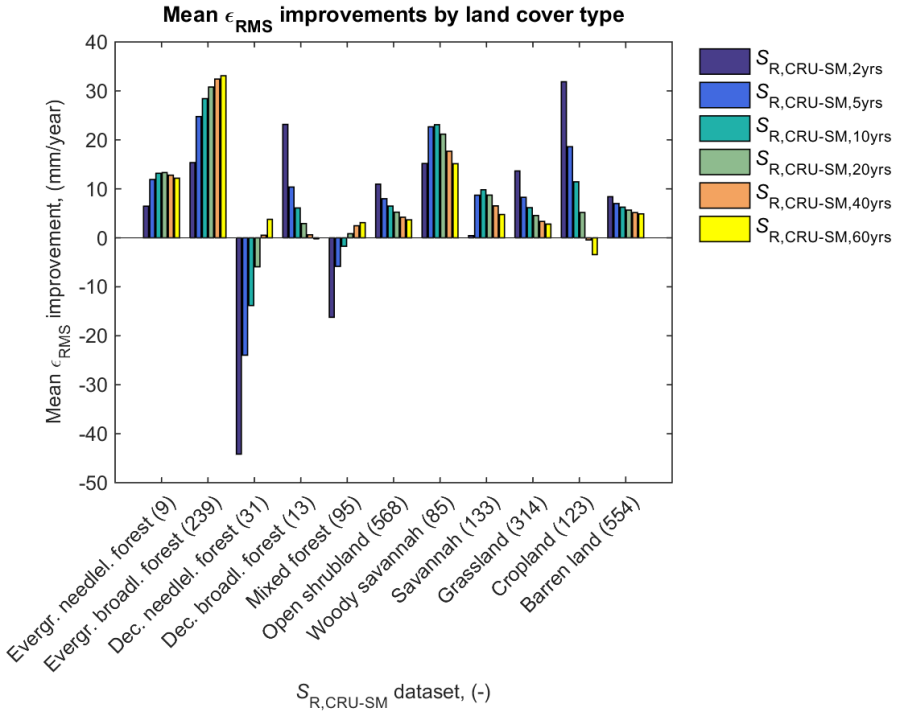

Figure 5.11: The mean ε_{RMS} improvement in simulated monthly evaporation E (2003–2013) by implementing $S_{R,CRU-SM,Lyrs}$ (based on P_{CRU} and E_{SM}) instead of $S_{R,STEAM}$ (based on look-up table in Wang-Erlandsson et al. (2014)) in the global hydrological model STEAM, where the satellite based E_{SM} was used as the benchmark for improvements (see methods described in Sect. 5.2.2). The improvements for root zone storage capacities with different return periods L 2-60 yrs (i.e., $S_{R,CRU-SM,2yrs}$, $S_{R,CRU-SM,5yrs}$, $S_{R,CRU-SM,10yrs}$, $S_{R,CRU-SM,20yrs}$, $S_{R,CRU-SM,40yrs}$, and $S_{R,CRU-SM,60yrs}$) are shown for the different land-cover types that has >90 % grid cell coverage. The number of represented grid cells are provided in the parenthesis following each land-cover type label along the x-axis.

rather than to extreme drought years. In extreme years, they survive by going dormant. Evergreen broadleaf forests, on the other hand, adapt to 40–60 years of drought return period since they deal with droughts by accessing deeper soil moisture storages and thus invest in root growth (Brunner et al., 2015). The performance increases in deciduous needleleaf forests by using 60 years of drought return period could be explained by their need to cater for dry periods during their most active summer months. Shedding the leaves during the wet season (semi-arid tropics) or the growing season (summer in temperate climates) is not attractive because it prevents reproduction. Interestingly, deciduous broadleaf forests appear to adapt to a 2 years drought return period - i.e., radically different to deciduous needleleaf forests. This is possibly due to their younger age (Poulter, 2012; Hicke et al., 2007) and considerably shorter longevity (Larson, 2001; Loehle, 1988). Longevity could be explained by strong defence mechanisms against

fungi and insects, lack of physical environmental damage, but also low occurrence of environmental stress such as drought (Larson, 2001). Thus, it seems logical that the older and longer living deciduous needleleaf forests have developed their root zone storage capacities to stand against more extreme droughts. Analysing the performance by each land-cover type reveals interesting patterns (such as the contrast between deciduous needleleaf and broadleaf forests), but also leads to small sample sizes (particularly for evergreen needleleaf forests and the deciduous forest types) that should be considered when interpreting the results.

Based on the best performing drought return periods for each land-cover types, we created a Gumbel normalised root zone storage capacity map (Supplementaty Fig. S9, Wang-Erlandsson et al. (2016)).

5.4.5. CLIMATIC INFLUENCE ON ROOT ZONE STORAGE CAPACITY DEPENDING ON LAND-COVER TYPE

We use multiple linear regression to correlate $S_{R,CRU-SM}$ values to climatic indicators, with the aim to investigate how well climate indicators can predict root zone storage capacities in different land-cover types. It appears that climate indicators predict root zone storage capacities much better in evergreen forests than in short vegetation types. Figure 5.12 shows high R^2 in mostly evergreen forests; moderate R^2 in other forest types and croplands; and low R^2 in savannahs, shrublands and grasslands. This is probably because of their different drought survival strategies. While evergreen forests bridge droughts by water uptake from storage in their root zone, deciduous forests shed their leaves, and short vegetation types such as grasslands go dormant and decrease their transpiration to a minimum. The multiple linear regression model for S_R in croplands is moderately explained by climate indicators, potentially due to human management. All climate variables were selected by Akaike Information Criterion (AIC) in the multiple linear regression model (Table 5.2).

5.4.6. LIMITATIONS

Although research indicates that most ecosystem rooting depth are limited by water rather than other resources (Schenk, 2008), other factors may still cause S_R to be larger than what is considered here. A minimum rooting depth of 0.3–0.4 m are for example considered in Schenk and Jackson (2009). Although we are comparing others' rooting depth estimates to $S_{R,CRU-SM}$, they are not directly comparable. Our approach deals with the accessible water volume in the root zone, which is not always related to root zone depth since the root density can vary over the depth. Our S_R estimates implicitly capture the root density that is active in water uptake.

The $S_{R,CHIRPS-CSM}$ and $S_{R,CRU-SM}$ have been derived using evaporation and precipitation data from recent years (i.e., the 2000s), and should be used with caution if applied to past or future model simulations. Land-cover change during the years 2003–2013 have not been taken into account. This has potential impact on the computation of additional evaporation from irrigated areas with fast changing acreages.

Wetlands and groundwater dependent ecosystems produce additional evaporation that cannot be ascribed to local rainfall (van Dijk et al., 2014). Bastiaanssen et al. (2014) recently demonstrated for the Nile basin that in some areas, natural withdrawals

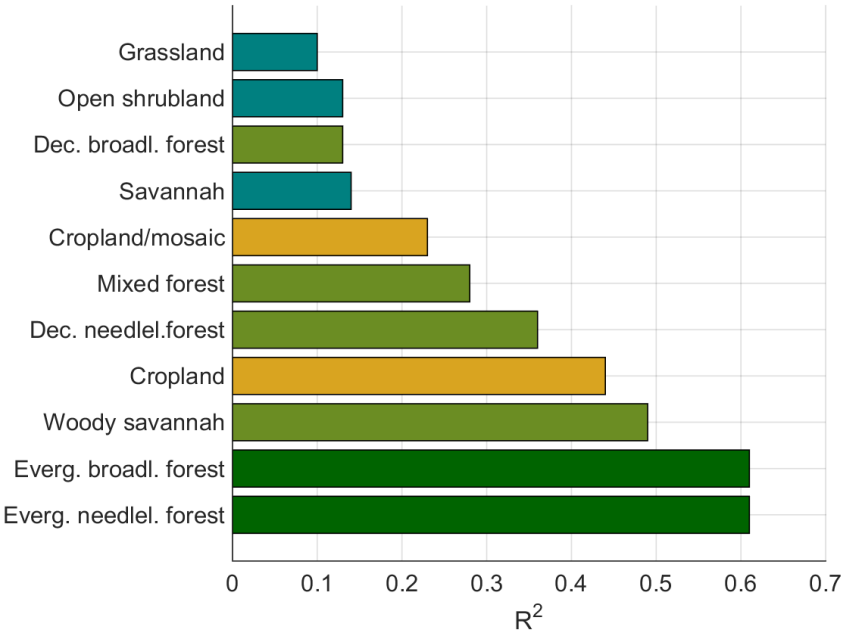

Figure 5.12: Coefficient of determination R^2 of the multiple linear regression model of $S_{R,CRU-SM}$ (based on P_{CRU} and E_{SM}) based on the climate variables interstorm duration I_{isd}, precipitation seasonality I_s, and aridity I_a. The green bars are forests or wooded land, the yellow bars represent croplands, and the teal bars represent short vegetation types.

exceed man-made withdrawals to the irrigation sector. Since satellite evaporation data captures all types of evaporation, and we only corrected for irrigation, natural additional evaporation sources are implicitly included in $S_{R,CHIRPS-CSM}$ and $S_{R,CRU-SM}$. Thus, our S_R estimates may not strictly represent the root zone storage capacities in regions where water uptake from groundwater is significant, see Fig. 5.3.

The choice of remotely sensed evaporation products influenced the resulting S_R more than the choice of precipitation product in this study (Supplementary Fig. S4, Wang-Erlandsson et al. (2016)). In particular, the largest standard deviations in the ensemble evaporation products are located in central South America, the Sahel, India, and northern Australia (see Fig. 5.2e, 5.2f). To reduce uncertainty, the presented method is preferably applied using ensemble products based on reliable evaporation and precipitation datasets identified in comparison and evaluation studies (e.g., Hofste, 2014; Hu et al., 2015; Yilmaz et al., 2014; Trambauer et al., 2014; Bitew and Gebremichael, 2011; Herold et al., 2015; Hessels, 2015; Hu and Jia, 2015; Moazami et al., 2013; Trenberth et al., 2013).

Finally, while the S_R estimates are model independent, the analyses of the best performing drought return periods of different land-cover types will depend on the hydrological model used, given the large variations of evaporation estimates (and in particular transpiration/evaporation ratios) among land surface models (e.g., Wang et al.,

Table 5.2: Predictor variables selected by Akaike Information Criterion (AIC) for the different land-cover types. The predictor variables are interstorm duration (I_{isd}), precipitation seasonality (I_s), and aridity index (I_a).

Land-cover type	Predictor variables
02:evergreen needleleaf forest	$S_R = I_{isd} + I_s + I_a + I_{isd}{:}I_a + I_s{:}I_a$
03:evergreen broadleaf forest	$S_R = I_{isd} + I_s + I_a + I_{isd}{:}I_s + I_s{:}I_a$
04:deciduous needleleaf forest	$S_R = I_{isd} + I_s + I_a + I_s{:}I_a + I_{isd}{:}I_a + I_{isd}{:}I_s + I_{isd}{:}\ I_s{:}I_a$
05:deciduous broadleaf forest	$S_R = I_{isd} + I_s + I_a + I_s{:}I_a + I_{isd}{:}I_s$
06:mixed forests	$S_R = I_{isd} + I_s + I_a + I_{isd}{:}I_a + I_{isd}{:}I_s + I_s{:}I_a + I_{isd}{:}I_s{:}I_a$
08:open shrublands	$S_R = I_{isd} + I_s + I_a + I_{isd}{:}I_a + I_{isd}{:}I_s + I_s{:}I_a + I_{isd}{:}I_s{:}I_a$
09:woody savannas	$S_R = I_{isd} + I_s + I_a + I_{isd}{:}I_a + I_s{:}I_a$
10:savannas	$S_R = I_{isd} + I_s + I_a + I_{isd}{:}I_a + I_s{:}I_a + I_{isd}{:}I_s + I_{isd}{:}I_s{:}I_a$
11:grasslands	$S_R = I_{isd} + I_s + I_a + I_{isd}{:}I_s + I_s{:}I_a$
13:croplands	$S_R = I_{isd} + I_s + I_a + I_{isd}{:}I_a + I_{isd}{:}I_s + I_s{:}I_a + I_{isd}{:}\ I_s{:}I_a$
15:cropland/natural veg. mosaic	$S_R = I_{isd} + I_s + I_a + I_{isd}{:}I_s$
17:barren or sparsely vegetated	$S_R = I_{isd} + I_s + I_a + I_s{:}I_a + I_{isd}{:}\ I_a + I_{isd}{:}I_s$

2012). Thus, although the contrasting return periods for woody land-cover types and annual short vegetation types are supported by current knowledge about ecohydrological response to droughts, the calculated values are subject to assumptions. Uncertainties are probably largest for heterogeneous land-cover types (such as savannahs) because they tend to be challenging to parameterise and simulate. Therefore, implementation of S_R in other hydrological or land surface models would require model-specific analyses of optimal return periods.

5.5. SUMMARY AND CONCLUSION

This study presents a method to estimate root zone storage capacity in principle from remotely sensed evaporation and observation-based precipitation data, by assuming that plants do not invest more in their roots than necessary to bridge a dry period. Two global root zone storage estimates ($S_{R,CRU-SM}$ and $S_{R,CHIRPS-CSM}$) are presented based on different precipitation and evaporation datasets, but show in general similar patterns globally. $S_{R,CRU-SM}$ and $S_{R,CHIRPS-CSM}$ both improve mean annual E simulation in STEAM (Supplementary Fig. S7, Wang-Erlandsson et al. (2016)), and there is not a preferred product.

Different ecosystems have evolved to survive droughts of different return periods with different strategies. Our analyses showed that whereas long drought return period increased performance for many forest types, short drought return period increased performance for many short vegetation types. The best E simulation results were achieved when normalising the S_R estimate using a very short drought return period (~2 years) for deciduous broadleaf forests, grasslands, shrublands, croplands, and barren or sparsely vegetated lands, a medium length drought return period (~10-20 years) for evergreen needleleaf forests, woody savannahs, and savannahs, and a very long drought return

period (~60 years) for evergreeen broadleaf, deciduous needleleaf, and mixed forests. This is probably because grasslands survive extreme droughts by going dormant, whereas forests invest in root growth (Brunner et al., 2015). Thus, the root zone storage capacities of short vegetation types seem to adapt to average years, whereas those of forests adapt to extreme years. Differences among forest types are thought to be related to forest age and drought coping strategy. Normalisation to longer drought return periods should not be done for short-lived annual plants such as two third of the world's croplands (Cox et al., 2006), nor beyond the age of the ecosystem of concern, because vegetation can not be assumed to adapt beyond their age.

The S_R estimates presented here are both globally gridded and observation-based. They have the advantage over the field study based and statistically derived $S_{R,Schenk}$ (Schenk and Jackson, 2009) by being directly based on gridded data and by covering regions where observational studies are limited (e.g., the evergreen broadleaf forests). In comparison to the inverse modelling approaches of Kleidon (2004), the method presented in this study is independent of model simulations and therefore closer to direct observations.

The new S_R estimates can be used in hydrological and land surface modelling to improve simulation results, particularly in the dry season and in seasonal tropical forests where variations of root zone storage capacity are large. Using the new S_R as input to the hydrological model STEAM improved the evaporation simulation considerably in subhumid to humid regions with high seasonality. In particular, the most significant improvements occurred in the months with the least evaporation. Normalisation of S_R to different drought return periods for different land-cover types could further improved evaporation simulation in STEAM, suggesting that Gumbel normalisation is a viable method to optimise the S_R estimates prior to implementation in global hydrological or land surface models.

The presented method is simple to apply and in principle scale-independent. For researchers working at regional or local scales, root zone storage capacities can easily be derived using available evaporation and precipitation data. Moreover, when information on irrigation and groundwater use is available, they can be used to adjust S_R, as was done by for example van Dijk et al. (2014). Satellite-based evaporation datasets are also quickly being developed and improved. New global scale evaporation products such as ALEXI (Atmosphere-Land Exchange Inverse) (Anderson et al., 2011) and ETMonitor (Hu and Jia, 2015) are underway based on 375 and 1000 m pixels. More sophisticated two-layer surface energy balance models also have the capacity to distinguish transpiration from other forms of evaporation. This implies that local root zone storage capacity can be computed, based on transpiration fluxes, which is preferred from a bio-physical point of view (although it would require estimate of interception evaporation to calculate effective precipitation). As new evaporation datasets become available, the S_R estimates can easily be updated. In addition, this method can be used to diagnose and compare different evaporation products, in particular for identifying variations in seasonality. With longer time series of land-cover and climate data, this method can possibly also be used to infer the effect of climate change on root zone storage capacity as a function of the adaptability of vegetation to altered conditions.

6

LAND-USE IMPACTS ON RIVER FLOWS THROUGH MOISTURE RECYCLING

In nature, nothing exists alone.

Rachel Carson (1907-1964)

The effect of land-use change on river flows have traditionally been explained by local changes within a river basin. However, moisture recycling links land-use change in one place to evaporation changes and subsequent modifications of downwind precipitation in another location, with knock-on effects on distant river flows. Here we show that river flow changes are largely determined by the combined modifications of imported and exported moisture. In some of the world's largest basins, precipitation was in fact more influenced by extra-basin, than within-basin, land-use change. Moreover, we found that river flows in several non-transboundary basins were considerably influenced by land-use changes in foreign countries. This study brings a new dimension into the debate on the causes of observed and projected changes in runoff, opens the possibility of both exacerbating and alleviating water scarcity through land management outside the basin, and suggests new transboundary water relationships in international politics.

This chapter is partly based on:

Wang-Erlandsson, L., Fetzer, I., Keys, P., van der Ent, R. J., Savenije, H. H. G. and Gordon, L. J.: *Remote land-use impacts on river flows through atmospheric teleconnections*, Hydrology and Earth System Science Discussions, in review.

6.1. INTRODUCTION

River flows are fundamental for ecosystems, nutrient transport, and human well-being (Oki and Kanae, 2006). Anthropogenic changes to river flow include impact from climate change (precipitation (Gerten et al., 2008) and temperature (Betts et al., 2015)), solar dimming (Gedney et al., 2014), CO_2 fertilisation (Gedney et al., 2006), irrigation withdrawal and dams (Jaramillo and Destouni, 2015), and land-use and land-cover change (LUC) (Sterling et al., 2012). Several studies suggest LUC is the most important driver of past (e.g., Piao et al., 2007; Sterling et al., 2012) and future changes (Betts et al., 2015). However, these studies have either ignored that vegetation change influences precipitation (e.g., Piao et al., 2007; Sterling et al., 2012), or have not distinguished between effects of LUC within and outside the river basin boundary (Betts et al., 2015). About 40 percent of global terrestrial precipitation originates from terrestrial evaporation, which includes transpiration, interception, and soil evaporation (van der Ent et al., 2010, 2014). Evaporation travels on average 500-5000 km in the atmosphere (van der Ent and Savenije, 2011) – a distance likely to exceed the size of most river basins. The process of terrestrial evaporation returning to land as rainfall is called terrestrial moisture recycling (TMR). Although land-atmosphere interactions are complex and besides TMR include thermal layer processes and circulation perturbation (Tuinenburg, 2013), TMR is often the dominating process at the regional to continental scale (e.g., D'Almeida et al., 2007; Lawrence and Vandecar, 2014; Spracklen et al., 2012). Previous research exploring LUC effects on TMR, e.g., LUC impacts on crop yields (Bagley et al., 2012), self-amplifying forest dieback from TMR changes (Zemp et al., 2017), and de-vegetation effects on rainfall (Keys et al., 2016), have not quantified the impact on local and remote river flows.

Here, we analyse the effects of LUC on river flows, accounting for changes in TMR. We also estimate the relative contributions of within- and extra-basin LUC. The hydrological cycle is represented by coupling an Eulerian atmospheric tracking scheme Water Accounting Model-2layers (WAM-2layers) (van der Ent et al., 2014) with STEAM (Chapter 2), forced by potential land cover and current land use (including irrigation) respectively (Sect. 6.2.1). Present day precipitation is represented by the Multi-Source Weighted-Ensemble Precipitation (MSWEP) (Beck et al., 2017), whereas the precipitation under potential land cover is generated by iteratively propagating precipitation and evaporation changes simulated in STEAM and tracked in WAM-2layers (Sect. 6.2.1).

6.2. METHODS

6.2.1. COUPLING OF MOISTURE TRACKING SCHEME AND THE HYDROLOGICAL MODEL

Current land use scenarios do not require iterative model coupling, since present day hydrological flows can be represented by current data and simulation. To obtain evaporation and precipitation under potential land cover, STEAM is coupled with WAM-2layers by (1) simulating present day evaporation in STEAM and forward tracking terrestrial evaporation with WAM-2layers, (2) simulating evaporation in STEAM based on present day precipitation and potential land cover, and forward track the fate of terrestrial evaporation with WAM-2layers, (3) calculating the change in tracked precipitation, (4) updating the present day precipitation with the changes in tracked precipitation, and

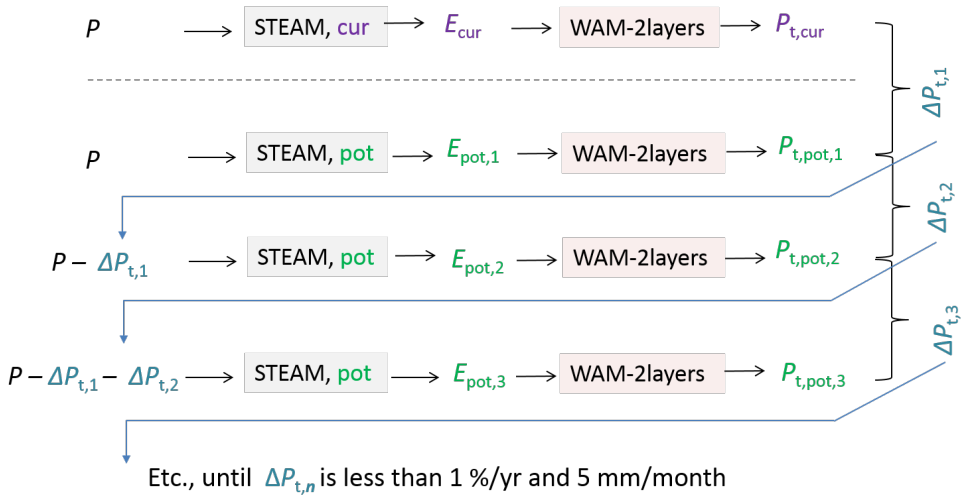

Figure 6.1: Model coupling between STEAM and WAM-2layers based on current land use and potential land cover scenarios. P stands for current precipitation, E stands for evaporation. Subscript $_t$ stands for terrestrial origin, $_{pot}$ denotes simulation with potential land cover, $_{cur}$ denotes simulation with current land use, and n stands for the number of iterations.

(5) simulating evaporation in STEAM based on updated precipitation and potential land cover, and forward tracking the fate of terrestrial evaporation with WAM-2layers, see Fig. 6.1. Steps 3-5 are iterated until the annual precipitation change is below 1 % and the monthly precipitation change is below 5 mm month^{-1} in every grid cell, which ultimately resulted in four iterations in total. This procedure assumes that land-use induced changes in terrestrial evaporation will result in proportional changes in precipitation with terrestrial origin. Previous coupling experiment with complete deforestation (Keys et al., 2016) based on this assumption resulted in rainfall reductions well in range of results from a comprehensive climate model simulations meta-analysis of Amazonian deforestation effects (Spracklen and Garcia-Carreras, 2015).

6.2.2. LITERATURE REVIEW OF ANTHROPOGENIC IMPACTS ON RIVER FLOWS

Our literature review of human induced changes in river flows encompass global studies of potential land cover to current land use, or transient studies of river flow changes over the 20th century. Studies without global coverage are not included in the comparison, (e.g., Gedney et al., 2006; Findell et al., 2007; Alkama et al., 2013; Labat et al., 2004; Dai et al., 2009) are excluded due to smaller land areas than other studies included. The results of Labat et al. (2004) have also been contested by later studies (Alkama et al., 2011; Legates et al., 2005; Milliman et al., 2008). Dai et al. (2009) also only covers river flow changes 1948-2004. We do not assume evaporation change to correspond to river flow change, unless authors explicitly endorse the translation. This excludes for example Gordon et al. (2005) and Boisier et al. (2014) from the inter-comparison.

6.2.3. CHANGES IN HYDROLOGICAL FLOWS

River flow change without TMR ($\Delta Q_{\mathrm{noTMR}}$) is

$$\Delta Q_{\mathrm{noTMR}} = (P_{\mathrm{cur}} - E_{\mathrm{cur}}) - (P_{\mathrm{cur}} - E_{\mathrm{pot},1}) \tag{6.1}$$

where P_{cur} is current day precipitation data from MSWEP, E_{cur} is current day evaporation based on STEAM simulation, and $E_{\mathrm{pot},1}$ results from STEAM simulation in the potential vegetation scenario and forced with current day precipitation (Fig. 6.1). River flow change after accounting for TMR (ΔQ) is

$$\Delta Q = (P_{\mathrm{cur}} - E_{\mathrm{cur}}) - (P_{\mathrm{pot},4} - E_{\mathrm{pot},5}) \tag{6.2}$$

where $P_{\mathrm{pot},4}$ is the converged precipitation (i.e., meeting the convergence requirement of mean annual precipitation change $< 1\,\%$ and monthly precipitation change < 5 mm month^{-1} in every grid cell) achieved at the fourth iterative coupling between STEAM and WAM-2layers, and $E_{\mathrm{pot},5}$ is the evaporation under the potential vegetation scenario simulated in STEAM with precipitation forcing $P_{\mathrm{pot},4}$.

Precipitation change in a basin that originates from extra-basin evaporation ($\Delta P_{\mathrm{import}}$) is defined as the change in tracked basin precipitation ($\Delta P_{\mathrm{tracked,\,basin}}$) occurring outside the river basin boundaries, whereas change in internally recycled precipitation ($\Delta P_{\mathrm{basin,\,recycling}}$) is defined as $\Delta P_{\mathrm{tracked,\,basin}}$ originating from within the basin boundary. Internally recycled evaporation ($\Delta E_{\mathrm{basin,\,recycling}}$) corresponds to $\Delta P_{\mathrm{basin,\,recycling}}$ and all other basin evaporation change is considered exported ($\Delta E_{\mathrm{export}}$).

6.2.4. COUNTRY INFLUENCE ON CHANGES IN RIVER FLOWS

The influence on river flow change in river basin $_{\mathrm{b}}$ from country $_{\mathrm{c}}$ without considering TMR ($I_{\mathrm{b,c,noTMR}}$) is:

$$I_{\mathrm{b,c,noTMR}} = |\Delta E_{\mathrm{b,c}}| \tag{6.3}$$

where $\Delta E_{\mathrm{b,\,c}}$ is evaporation change in the part of river basin $_{\mathrm{b}}$ located in country $_{\mathrm{c}}$. The influence on river flow change in basin $_{\mathrm{b}}$ from country $_{\mathrm{c}}$ with consideration of TMR ($I_{\mathrm{b,c,noTMR}}$) is:

$$I_{\mathrm{b,c,TMR}} = |\Delta E_{\mathrm{b,c,export}}| + |\Delta P_{\mathrm{b,c,import}}| \tag{6.4}$$

where $\Delta E_{\mathrm{b,c,export}}$ is the evaporation change exported from the part of basin $_{\mathrm{b}}$ located in country $_{\mathrm{c}}$, and $\Delta P_{\mathrm{b,c,import}}$ is the precipitation change imported to basin $_{\mathrm{b}}$ from country $_{\mathrm{c}}$.

Influences from countries below 5 % of total influences in a specific basin ($I_{\mathrm{b,c,noTMR}} < 0.05 \times \Sigma I_{\mathrm{b,c,noTMR}}$) are lumped into the category "Other".

6.3. RESULTS AND DISCUSSIONS

6.3.1. CHANGES IN TERRESTRIAL HYDROLOGICAL FLOWS

Our results show anthropogenic LUC (from potential land cover to current land use) (Fig. 6.2a) has led to reductions in evaporation and precipitation, and to increases in river flows, in most regions (Fig. 6.2b-d). Evaporation has decreased primarily in Southwest

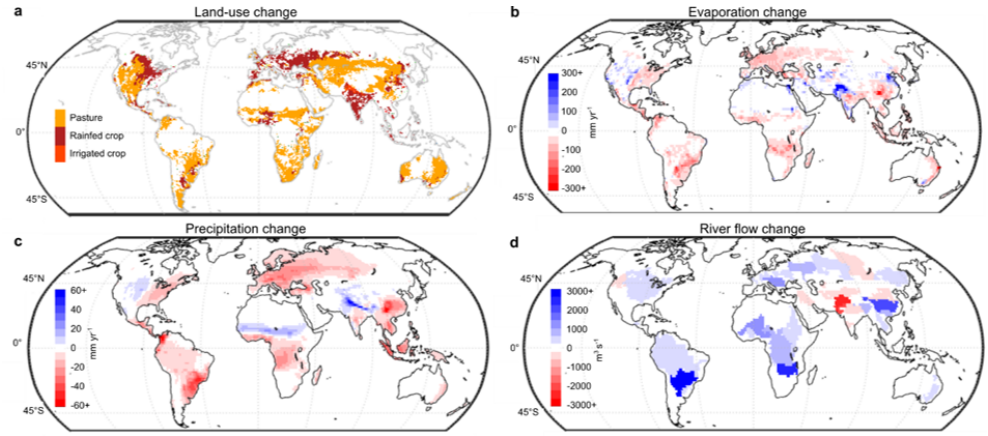

Figure 6.2: Differences between the current land-use and the potential land cover scenario. Changes in **a**, land use (only shifts in grid cell dominant land-use types are shown), **b**, mean annual evaporation (changes < ±20 mm yr^{-1} are in white), **c**, mean annual precipitation (changes < ± 4 mm yr^{-1} are in white), and **d**, mean annual river flow (changes < ±200 m^3 yr^{-1} are in white). Note that changes in river flows are aggregated to river basin level and shown in m^3 s^{-1}.

China, Europe, West Africa, south of Congo, and southeast South America resulting from substantial pasture and agricultural expansion (Ramankutty et al., 2008). Following prevailing wind directions, subsequent precipitation has decreased in all tropical regions, in South Central China, eastern US, and Europe.

Nevertheless, in some areas, evaporation increased due to incremental irrigation – notably in India, the US, Northeast China, and in the Middle East (Fig. 6.2b). Due to the combination of heavy irrigation in India and orography, precipitation has increased substantially along the Himalaya mountain ridge (Fig. 6.2c). Weak increases in precipitation are observed in other downwind regions: the Sahel (i.e., downwind irrigation areas along the Nile) and in the Western US. Changes in river flows are seen in the La Plata basin in South America, the Zambezi in Southern Africa, the Yangtze in China, and the Indus in North India (Fig. 6.2d).

In aggregate (Fig. 6.3), when accounting for TMR, LUC changed global terrestrial evaporation by −1251 km^3 yr^{-1} (−1.8 % from 69,211 km^3 yr^{-1}), precipitation by −586 km^3 yr^{-1} (−0.5 % from 107,800 km^3 yr^{-1}), and river flows by 664 km^3 yr^{-1} (+1.7 % from 38,589 km^3 yr^{-1}). The estimated changes to river runoff fall in the conservative end of previous estimates (Sterling et al., 2012) (Fig. 6.3). River flow change with TMR corresponds to the difference between evaporation and precipitation change including TMR (Fig. 6.3, solid bars), whereas change to river flows without accounting for TMR simply corresponds to evaporation change without TMR (Fig. 6.3, hollow bars).

Including TMR nearly halves the global river flow change estimate. This is because evaporation returns as precipitation over land and thus compensates for the initial water "loss" from the basin. This suggests previous studies without TMR (e.g., Gerten et al., 2008; Piao et al., 2007; Sterling et al., 2012) may have substantially overestimated the net LUC impacts on river flow. The new estimate of LUC impact on river flows is comparable to

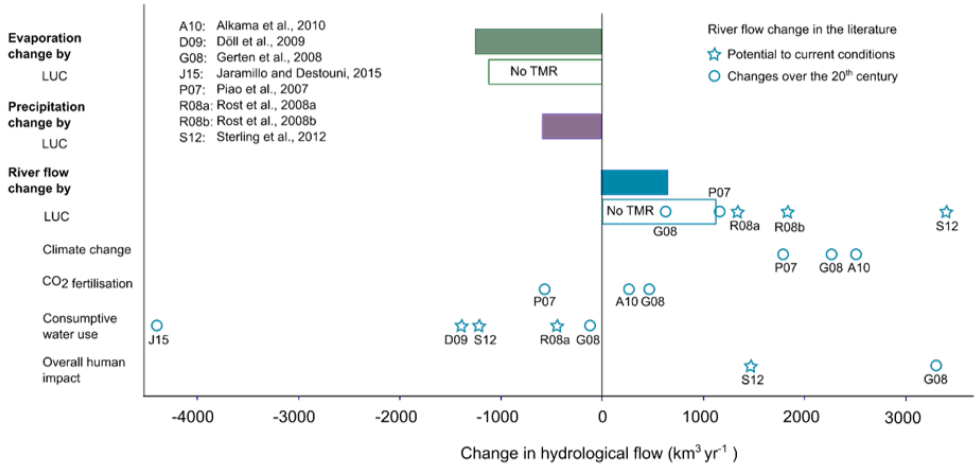

Figure 6.3: Human impact on global hydrological flows. The solid bars show our estimated net change (terrestrial area 131,710,600 km^2 and time period 2000–2013) in evaporation, precipitation and river flows including consideration of terrestrial moisture recycling (TMR). Hollow bars show flow changes without TMR. Circles and stars indicate river flow change estimates from other studies, where land-use change (LUC) implicitly accounts for consumptive water use. Note that while consumptive water use alone always reduces river flows, other human impacts have both positive and negative influences that are concealed by the global aggregate.

6

some of the estimates of CO_2 fertilisation and consumptive water use (i.e., net withdrawal) impacts, but smaller than climate change and overall human impact (Fig. 6.3).

The annual aggregate conceals markedly stronger seasonal responses, as shown for example in the northern hemisphere in July (compare Fig. 6.4 and 6.2). On other regions, such as Sahel and Southeast Africa, the direction of hydrological change reverses with season (Fig. 6.4), and cancel each other out at the annual scale (Fig. 6.2). $\Delta P - E$ in Fig. 6.4 corresponds to the monthly change in both hydrological storage and runoff. For example, Sahel experiences an increased water storage or river flows in January, but storage or river flows declines are larger in July due to anthropogenic land-use change.

6.3.2. RIVER FLOW CHANGES AT BASIN AND NATION SCALE

Our river basin analysis shows that accounting for TMR considerably alters estimates of river flow change. In the Amazon, Congo, Volga, and Ob basins, river flow changes are reduced by more than half by considering TMR (Fig. 6.5a). In the Amazon, river flow change drops from 1630 m^3 s^{-1} to 270 m^3 s^{-1}. In the Yenisei, the sign of river flow change is reversed from an increase (150 m^{-3} s^{-1}) to a decrease (−220 m^3 s^{-1}) by considering TMR.

Furthermore, atmospheric moisture do not respect river basin boundaries (Fig. 6.5a.). In fact, precipitation over the basins has been modified more significantly by external than by internal LUC (change in imported precipitation ΔP_{import} > change in internally recycled precipitation $\Delta P_{\text{basin,recycling}}$) in some of the largest basins (Fig. 6.5a). Likewise,

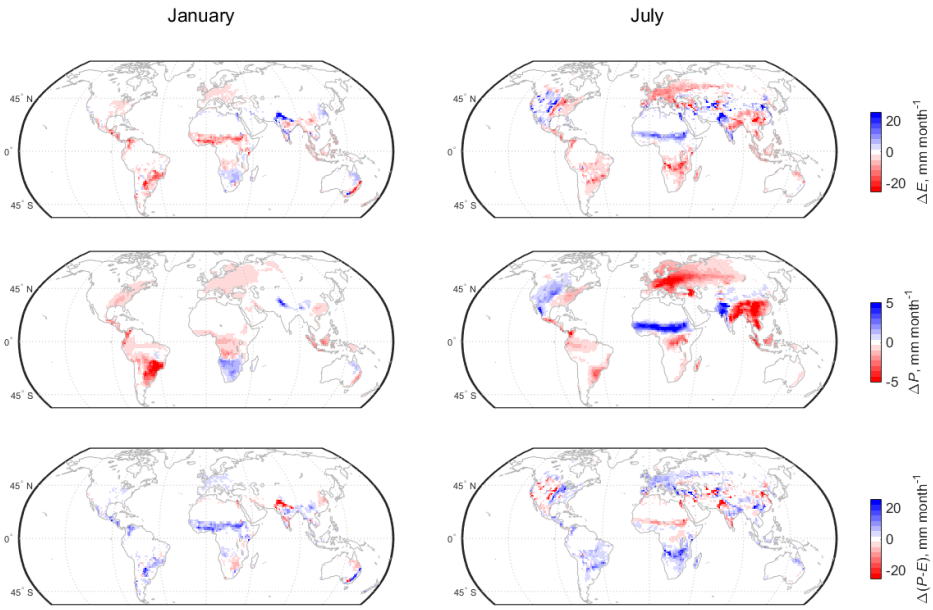

Figure 6.4: Seasonal hydrological flow changes. E denotes evaporation and P precipitation. The scales of ΔE and ΔP are directly comparable to those in Fig. 6.2.

internally recycled evaporation changes (Fig. 6.5b, II) are substantially smaller than evaporation changes affecting precipitation elsewhere (change in internally recycled evaporation $\Delta E_{\text{basin,recycling}}$ < change in exported evaporation ΔE_{export}) for all selected river basins (Fig. 6.5a).

Internal moisture recycling (Fig. 6.5b, II) do not affect river flow change (ΔQ) directly, only indirectly if $\Delta P_{\text{basin,recycling}}$ affects subsequent ΔE_{export} under transient change (Fig. 6.5b and Sect. 6.2). Thus, provided steady-state, ΔQ simply corresponds to the difference between ΔE_{export} and ΔE_{import} (Fig. 6.5a). For example, river flow change in the Amazon is very small because the reduced ΔP_{import} is almost entirely offset by reduced ΔE_{export}. In Congo, about half of the within-basin LUC induced river flow increase is counteracted by extra-basin LUC (i.e., $\Delta P_{\text{import}} \approx 0.5\Delta E_{\text{export}}$). The effect of TMR on river flow change estimate ($\Delta P_{\text{noTMR}} - \Delta Q$, where subscript $_{\text{noTMR}}$ denotes simulation without TMR) corresponds to total precipitation change ($\Delta P_{\text{import}} + \Delta P_{\text{basin,recycling}}$) and any indirect change in evaporation ($\Delta E_{\text{noTMR}} - \Delta E$, not shown). In Yangtze, the river flow change is mitigated mostly by $\Delta P_{\text{basin,recycling}}$. The strong flow reduction in the heavily irrigated Indus, however, is only mildly compensated by TMR (i.e., $\Delta P_{\text{import}} \ll \Delta E_{\text{export}}$).

Consideration of TMR in river basin analyses have governance implications. Typically, a larger number of countries become responsible for LUC-driven river flow changes in specific basins (Fig. 6.6). For example, in the Amazon, river flow change originates from as far away as Africa (Fig. 6.6b-c). Because of the large LUC-induced evaporation

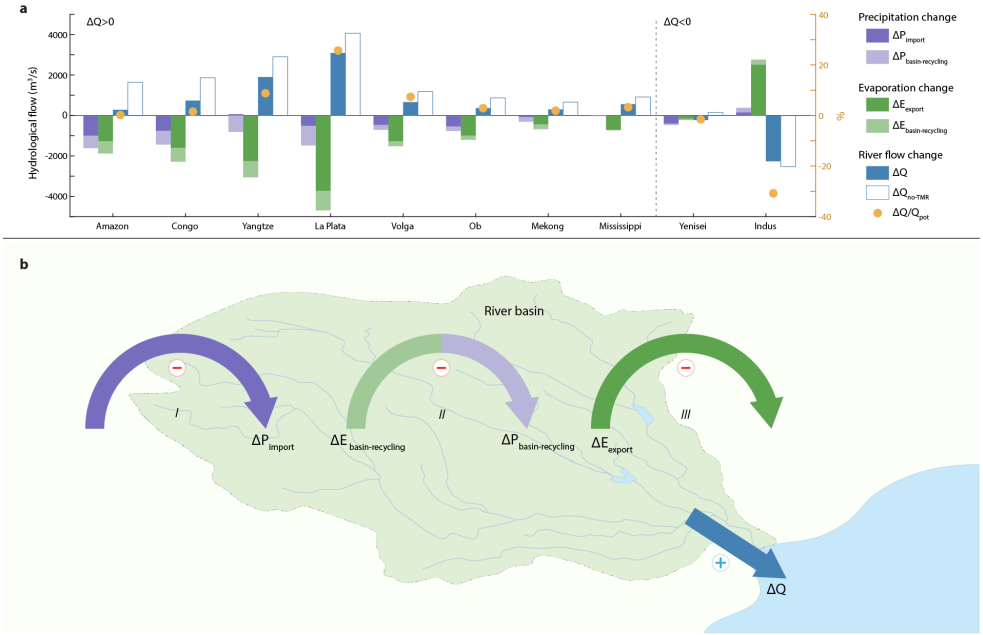

Figure 6.5: Changes in hydrological flows at river basin scale. **a**, Changes in hydrological flows by ten basins with the largest terrestrial moisture recycling (TMR) effect on river flows: eight basins with increased and two with decreased river flows (Q). Basins are ordered by maximum absolute TMR effect on river flows, i.e., the difference between river flows with or without TMR ($\Delta Q - \Delta Q_{\mathrm{noTMR}}$). **b**, Conceptual figure of hydrological flow changes in a basin. The (−) and (+) as displayed here are e.g. seen in Amazon, Congo, Volga. In Indus and Yenisei, the (−) and (+) are reversed.

reductions, the African influence on Amazon river flow change is comparable to within-basin influence (Sect. 6.2). Notably, river basins geographically confined within one nation can be influenced by LUC in other countries, thus becoming transboundary. This is for example the case in Yangtze, where irrigation in India increases the basin's precipitation (Fig. 6.6g).

6.3.3. LIMITATIONS

LUC impacts on precipitation are notoriously challenging to simulate. Our approach only accounts for the TMR influence from LUC (Spracklen et al., 2012), which often is the dominant process at intermediary scales (Tuinenburg, 2013). At smaller scales, local forest clearing has been shown to enhance rainfall due to turbulence changes (Koster et al., 2003), and at continental scales, irrigation in monsoon regions may reduce rainfall by weakening the monsoon onset (Tuinenburg, 2013). Climate models have also simulated surprising LUC impacts on precipitation on other continents through teleconnections (Lawrence and Vandecar, 2014), although results vary widely with models. Biogenic emissions and aerosols may further have uncertain impacts on precipitation (Koren et al., 2012). In addition, there are inherent uncertainties in circulation change in

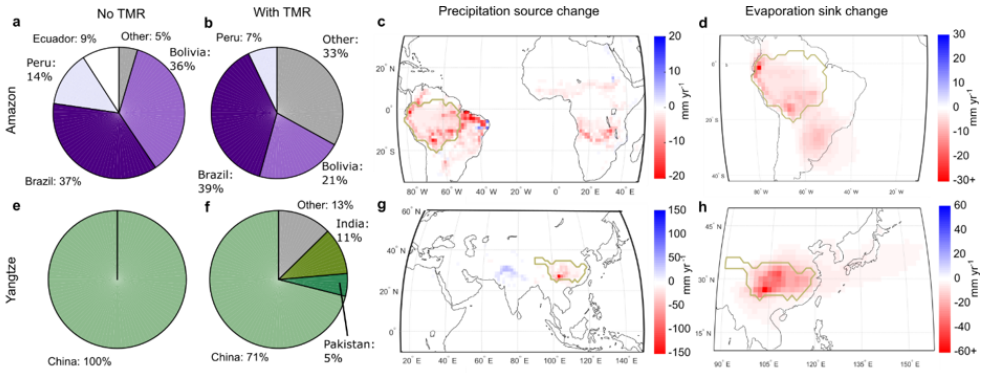

Figure 6.6: Nation influence of river flow change depending on consideration of terrestrial moisture recycling (TMR) in **a**-**b**, Amazon and **e**-**f**, Yangtze. Without TMR, the nation influence on river flow change originates entirely from within-basin country-wise evaporation change (**a**, **e**). By considering TMR, the nation influence (**b**, **f**) is the sum of absolute imported precipitation change (precipitation source outside encircled basin boundaries in **c** and **g**) and of absolute exported evaporation change (evaporation sink outside encircled basin boundaries in **d** and **h**) (Sect. 6.2). Precipitation sources (**c**, **g**) and evaporation sinks (**d**, **h**) within basin boundaries are recycled.

climate simulations (Shepherd, 2014). Our study should be seen as an inquiry to better understand the relative importance of local and remote LUC effects on river flows from a water balance perspective, rather than an exact prediction. Nevertheless, we are confident in our conclusion that upwind extra-basin LUC can be essential for river flows.

6.4. CONCLUSIONS

These findings have substantial implications for water resources management on a human dominated planet. First, despite the river basin being the standard unit in water resources management, we find that river flow changes are ultimately dependent on the modifications in both incoming precipitation and outflowing evaporation. Where extra-basin LUC affects basin precipitation more strongly than within-basin LUC, reforesting a river basin may lead to unexpectedly large reductions in river flows if deforestation simultaneously occurs in precipitation source regions outside the river basin. Therefore, we emphasize the necessity of considering both the origin of basin precipitation as well as the fate of basin evaporation for management of local water resources. Second, beside LUC, other processes such as asynchronous changes in climate conditions, e.g., wetting or drying trends (Greve et al., 2014) in precipitation source regions outside the given river basin, can in similar manner mediate trends in internal river basin hydrology. Finally, we suggest new geo-political relationships of river basins where extra-basin LUC is important for river flows changes. Potential international political negotiations of teleconnnected LUC influence could be needed, even for river basins that are not considered transboundary. We conclude that consideration of TMR is essential for understanding river flow modifications and managing water resources in a rapidly changing world facing increasing pressure on both land and water.

7

CONCLUSIONS AND OUTLOOK

There was a long silence.
Then Snufkin said slowly:
'It would be awful if the earth exploded.
It is so beautiful.'
'And what about us?' said Sniff.

Tove Jansson (1914-2001)
'Comet in Moominland'

This chapter is partly based on:

Wang-Erlandsson, L., van der Ent, R. J., Gordon, L. J., and Savenije, H. H. G.: *Contrasting roles of interception and transpiration in the hydrological cycle — Part 1: Temporal characteristics over land*, Earth System Dynamics, 5, 441–469, 2014.

Wang-Erlandsson, L., Bastiaanssen, W. G. M., Gao, H., Jägermeyr, J., Senay, G. B., van Dijk, A. I. J. M. Guerschman, J. P., Keys, P. W., van der Ent, R. J., Gordon, L. J., and Savenije, H. H. G.: *Global root zone storage capacity from satellite-based evaporation*, Hydrology and Earth System Sciences, 4, 1459–1481, 2016.

Wang-Erlandsson, L., Fetzer, I., Keys, P., van der Ent, R. J., Savenije, H. H. G. and Gordon, L. J.: *Remote land-use impacts on river flows through atmospheric teleconnections*, Hydrology and Earth System Science Discussions, in review.

7.1. CONCLUSIONS

The hydrological cycle over land is strikingly different from that over the ocean due to the complex interaction with vegetation and land-use. Evaporation over land consists of several different fluxes with substantially different temporal scales. Rainfall intercepted on vegetation surfaces returns to the atmosphere as evaporation within hours after a rain event, whereas rainfall that becomes transpiration lingers days and months on land. Thus, in subsequent moisture recycling, interception resumes the role of local rainfall multiplier, whereas transpiration provides rainfall to distant downwind regions. Due to the longer terrestrial residence time, transpiration is also active during dry spells. Potentially, this implies that vegetation with deep roots (such as mature forests) and land management practices that favour transpiration (such as rainwater harvesting) can serve an important function in maintaining rainfall during dry periods.

However, transpiration time scales are sensitive to a highly uncertain parameter in global hydrological and land surface modelling – the root zone storage capacity. Improving root zone storage capacity based on satellite-based evaporation data improved evaporation simulation in STEAM considerably in subhumid to humid regions with high seasonality. In particular, the most significant improvements occurred in the months with the least evaporation. Using observation-based data to estimate root zone storage capacity improves our ability to simulate the terrestrial hydrological cycle, including the terrestrial temporal scale of transpiration.

The importance of evaporation, evaporation partitioning, and evaporation terrestrial residence time in the terrestrial hydrological cycle also means that they are essential for land-use change induced effects on the terrestrial hydrological cycle. However, river flow change has been frequently and solely studied as direct effects of land-use change, without accounting for the changes in evaporation and subsequent rainfall beyond river basin boundaries. In fact, river flow changes are largely determined by the combined modifications of imported and exported moisture to and from the basin. The effect of moisture recycling is so important that accounting for it cuts the estimated global anthropogenic land-use change impact on river flows almost by half. In some of the world's largest basins, precipitation was also found to be more influenced by extra-basin, than within-basin, land-use change, with consequences for river flows in the basin. Moreover, river flows in several non-transboundary basins have been considerably influenced by land-use changes in foreign countries. Thus, water resources management need to transcend the basin boundary to fully account for effects generated along the entire water cycle pathway.

In conclusion, this thesis highlights the cyclic nature of the terrestrial hydrological cycle. To understand the terrestrial water cycle, every water flux and stock requires our examination, whether they flow visibly in rivers, travel invisibly in the air, or hide deep in soil and roots. Water undergoes several cycles on land before departing for the ocean, and there is no scientific basis for generally labelling evaporation as a 'loss'. Because of the terrestrial water cycle's interaction with vegetation and land, and therefore ecosystems and human society, we are in an extraordinary position to shape its path and pace.

7.2. FUTURE RESEARCH OUTLOOK

To better understand how land and water interacts, this thesis advances the understanding of time scales of evaporation partitioning and root zone storage capacity. Many more fundamental aspects of the hydrological cycle, ecosystem responses, and atmospheric processes require research. For example, despite its importance, the terrestrial evaporation partitioning remains controversial (Jasechko et al., 2013; Coenders-Gerrits et al., 2014). New leaf-scale experiments recently suggest that the generally assumed one-sided sensible heat flux exchange in the widely used Penman-Monteith potential evaporation equation leads to considerable bias in flux estimates, which have consequences for modelling of e.g., sensitivities of transpiration to climate change (Schymanski and Or, 2017). Under current climate change, increase in CO_2 has been suggested to decrease transpiration through increased water use efficiency (Keenan et al., 2013), but also to increase total evaporation due to increased biomass and leaf area (Piao et al., 2007). Furthermore, climate modelling results of land-use change impacts on precipitation still vary widely (Pitman et al., 2012; Lawrence and Vandecar, 2014). Other important uncertainties includes the effects of biogenic emissions and aerosols on precipitation (Koren et al., 2012). In addition, the role of vegetation for mediating atmospheric circulation is heatedly debated, and scientists remain divided on the 'biotic pump' theory (Makarieva and Gorshkov, 2007; Makarieva et al., 2014; Meesters et al., 2009). Finally, there are inherent uncertainties in circulation change in climate simulations that may not be possible to resolve (Shepherd, 2014).

A particular type of uncertainty involves the risk of large, abrupt, and persistent changes in the structure and function of a system – i.e., regime shift (e.g., Holling, 1973; Scheffer et al., 2001; Lenton et al., 2008). For example, the risk of tropical rainforest transitioning into savannah below certain rainfall thresholds is a field of active research (e.g., Hirota et al., 2011; Staver et al., 2011; van Nes et al., 2014; Zemp et al., 2017). Other examples of water and land related tipping points are desertification, salinisation, river and groundwater depletion (Rockström et al., 2014). Changes in land and water systems at the regional scale can together aggregate to planetary scale risks (Rockström et al., 2009a; Steffen et al., 2015) and are connected through moisture recycling and perturbation of wind patterns (e.g., Kleidon and Heimann, 2000; Goessling and Reick, 2011), but how and how much regional scale regime shifts potentially interact is in need of further research.

Independent of current challenges in fully understanding land-water interactions, human societies unabated continue to impact land and water. Science, thus, has an important role in supporting policy making given existing uncertainties and knowledge gaps. Current initiatives to integrate the land-water biophysics with policy include e.g., the incorporation of moisture recycling into water accounting and footprint studies (e.g., Karimi et al., 2013; Berger et al., 2014), the introduction of 'precipitationshed' and 'evaporationshed' (Keys et al., 2012; van der Ent and Savenije, 2013) as new water boundaries, and the suggestion to consider moisture recycling as an ecosystem service (Keys et al., 2016; van Noordwijk et al., 2014). These moisture recycling based approaches are attractive for management and policy because of their simplicity, and can directly employ the iterative model coupling method demonstrated in Chapter 6. The next natural steps are to better understand the uncertainties and limitations, and to research how taking account of land-atmosphere interactions could align with existing policy making.

Finally, we live in an increasingly interconnected world. Because of global trade, water scarce nations can now import water-intensive commodities from water rich countries to mitigate their water supply shortage (Allan, 1997). Increasingly, land itself can be acquired by foreign nations, and found to potentially allow foreign actors to affect local water resources (Johansson et al., 2016). In fact, land-use change can now be affected by issues as divergent as trade, migration, and the rise of middle class consumption on another continent because of globalisation (Lambin et al., 2001; Lambin and Meyfroidt, 2011; Meyfroidt et al., 2010, 2013), while fresh water availability can influence conflicts, migration, and economies (Wilhite and Glantz, 1985). Evidently, the interconnections between social, financial, political, and ecological systems need to be investigated, and the moisture recycling mechanism can be useful as a first order estimate of land-water interactions in such complex analyses.

REFERENCES

Alkama, R., Decharme, B., Douville, H., Ribes, A., 2011. Trends in Global and Basin-Scale Runoff over the Late Twentieth Century: Methodological Issues and Sources of Uncertainty. Journal of Climate 24 (12), 3000–3014.

Alkama, R., Marchand, L., Ribes, A., Decharme, B., 2013. Detection of global runoff changes: results from observations and CMIP5 experiments. Hydrology and Earth System Sciences 17 (7), 2967–2979.

Allan, J., 1997. 'Virtual water': a long term solution for water short Middle Eastern economies? In: British Association Festival of Science. pp. 1–21.

Allen, R. G., Pereira, L. S., Raes, D., Smith, M., 1998. Crop evapotranspiration - Guidelines for computing crop water requirements - FAO Irrigation and drainage paper 56. Tech. rep., FAO - Food and Agriculture Organization of the United Nations, Rome.
URL http://www.fao.org/docrep/x0490e/x0490e00.htm{#}Contents

Allen, R. G., Pruitt, W. O., Wright, J. L., Howell, T. a., Ventura, F., Snyder, R., Itenfisu, D., Steduto, P., Berengena, J., Yrisarry, J. B., Smith, M., Pereira, L. S., Raes, D., Perrier, A., Alves, I., Walter, I., Elliott, R., 2006. A recommendation on standardized surface resistance for hourly calculation of reference ETo by the FAO56 Penman-Monteith method. Agricultural Water Management 81 (1-2), 1–22.

Aloysius, N. R., Sheffield, J., Saiers, J. E., Li, H., Wood, E. F., 2016. Evaluation of historical and future simulations of precipitation and temperature in central Africa from CMIP5 climate models. Journal of Geophysical Research: Atmospheres 121 (1), 130–152.

Alton, P., Fisher, R., Los, S., Williams, M., 2009. Simulations of global evapotranspiration using semiempirical and mechanistic schemes of plant hydrology. Global Biogeochemical Cycles 23 (4), GB4032.

Anderson, M. C., Kustas, W. P., Norman, J. M., Hain, C. R., Mecikalski, J. R., Schultz, L., González-Dugo, M. P., Cammalleri, C., D'Urso, G., Pimstein, A., Gao, F., 2011. Mapping daily evapotranspiration at field to continental scales using geostationary and polar orbiting satellite imagery. Hydrology and Earth System Sciences 15 (1), 223–239.

Avissar, R., Werth, D., 2005. Global hydroclimatological teleconnections resulting from tropical deforestation. Journal of Hydrometeorology 6 (1993), 134–145.

Badger, A. M., Dirmeyer, P. A., 2016. Remote tropical and sub-tropical responses to Amazon deforestation. Climate Dynamics 46 (9-10), 3057–3066.

Bagley, J. E., Desai, A. R., Dirmeyer, P. A., Foley, J. A., 2012. Effects of land cover change on moisture availability and potential crop yield in the world's breadbaskets. Environmental Research Letters 7 (1), 014009.

Bagley, J. E., Desai, A. R., West, P. C., Foley, J. A., 2011. A Simple, Minimal Parameter Model for Predicting the Influence of Changing Land Cover on the Land–Atmosphere System? Earth Interactions 15 (29), 1–32.

Barnett, C., 2015. Rain: A Natural and Cultural History. Broadway Books, New York.

Bastiaanssen, W., Allen, R., Droogers, P., D'Urso, G., Steduto, P., 2007. Twenty-five years modeling irrigated and drained soils: State of the art. Agricultural Water Management 92 (3), 111–125.

Bastiaanssen, W. G. M., Cheema, M. J. M., Immerzeel, W. W., Miltenburg, I. J., Pelgrum, H., 2012. The surface energy balance and actual evapotranspiration of the transboundary Indus Basin estimated from satellite measurements and the ETLook model. Water Resources Research 48 (11), W11512.

Bastiaanssen, W. W., Karimi, P., Rebelo, L.-M. L.-M., Duan, Z., Senay, G., Muttuwatte, L., Smakhtin, V., 2014. Earth Observation Based Assessment of the Water Production and Water Consumption of Nile Basin Agro-Ecosystems. Open Access Remote Sensing special issue on Africa 6 (11), 10306–10334.

Beck, H. E., van Dijk, A. I. J. M., Levizzani, V., Schellekens, J., Miralles, D. G., Martens, B., de Roo, A., 2017. MSWEP: 3-hourly 0.25 degree global gridded precipitation (1979-2015) by merging gauge, satellite, and reanalysis data. Hydrology and Earth System Sciences 21 (1), 589–615.

Benton, G. S., 1949. The Role of the Atmosphere in the Hydrologic Cycle. Weatherwise 2 (5), 99–103.

Berger, M., van der Ent, R., Eisner, S., Bach, V., Finkbeiner, M., 2014. Water accounting and vulnerability evaluation (WAVE): considering atmospheric evaporation recycling and the risk of freshwater depletion in water footprinting. Environmental science & technology 48 (8), 4521–8.

Betts, R. A., Golding, N., Gonzalez, P., Gornall, J., Kahana, R., Kay, G., Mitchell, L., Wiltshire, A., 2015. Climate and land use change impacts on global terrestrial ecosystems and river flows in the HadGEM2-ES Earth system model using the representative concentration pathways. Biogeosciences 12 (5), 1317–1338.

Bevan, S. L., Los, S. O., North, P. R. J., 2014. Response of vegetation to the 2003 European drought was mitigated by height. Biogeosciences 11 (11), 2897–2908.

Beven, K., 2006. A manifesto for the equifinality thesis. Journal of Hydrology 320 (1-2), 18–36.

Bitew, M. M., Gebremichael, M., 2011. Evaluation of satellite rainfall products through hydrologic simulation in a fully distributed hydrologic model. Water Resources Research 47 (6), W06526.

Boisier, J. P., De Noblet-Ducoudré, N., Ciais, P., 2014. Historical land-use-induced evapotranspiration changes estimated from present-day observations and reconstructed land-cover maps. Hydrology and Earth System Sciences 11 (9), 2045–2089.

Bosilovich, M. G., Sud, Y., Schubert, S. D., Walker, G. K., 2002. GEWEX CSE sources of precipitation using GCM water vapor tracers. Tech. rep., GEWEX News.

Breuer, L., Eckhardt, K., Frede, H.-G., 2003. Plant parameter values for models in temperate climates. Ecological Modelling 169 (2-3), 237–293.

Brunner, I., Herzog, C., Dawes, M. A., Arend, M., Sperisen, C., 2015. How tree roots respond to drought. Frontiers in plant science 6, 547.

Budyko, M. I., 1974. Climate and Life. Academic Press.

Campos, I., González-Piqueras, J., Carrara, A., Villodre, J., Calera, A., 2016. Estimation of

total available water in the soil layer by integrating actual evapotranspiration data in a remote sensing-driven soil water balance. Journal of Hydrology 534, 427–439.

Canadell, J., Jackson, R. B., Ehleringer, J. B., Mooney, H. a., Sala, O. E., Schulze, E.-D., 1996. Maximum rooting depth of vegetation types at the global scale. Oecologia 108 (4), 583–595.

Chahine, M. T., 1992. The hydrological cycle and its influence on climate. Nature 359 (6394), 373–380.

Chen, B., Coops, N. C., Fu, D., Margolis, H. A., Amiro, B. D., Barr, A. G., Black, T. A., Arain, M. A., Bourque, C. P.-A., Flanagan, L. B., Lafleur, P. M., McCaughey, J. H., Wofsy, S. C., 2011. Assessing eddy-covariance flux tower location bias across the Fluxnet-Canada Research Network based on remote sensing and footprint modelling. Agricultural and Forest Meteorology 151 (1), 87–100.

Chen, L., Frauenfeld, O. W., 2014. A comprehensive evaluation of precipitation simulations over China based on CMIP5 multimodel ensemble projections. Journal of Geophysical Research Atmospheres 119 (10), 5767–5786.

Choudhury, B. J., DiGirolamo, N. E., Susskind, J., Darnell, W. L., Gupta, S. K., Asrar, G., 1998. A biophysical process-based estimate of global land surface evaporation using satellite and ancillary data II. Regional and global patterns of seasonal and annual variations. Journal of Hydrology 205 (3), 186–204.

Coenders-Gerrits, A. M. J., van der Ent, R. J., Bogaard, T. A., Wang-Erlandsson, L., Hrachowitz, M., Savenije, H. H. G., 2014. Uncertainties in transpiration estimates. Nature 506 (7478), E1–E2.

Collins, D. B. G., Bras, R. L., 2007. Plant rooting strategies in water-limited ecosystems. Water Resources Research 43 (6), W06407.

Cox, T. S., Glover, J. D., Van Tassel, D. L., Cox, C. M., DeHaan, L. R., 2006. Prospects for developing perennial grain crops. BioScience 56 (8), 649.

Crutzen, P. J., 2002. Geology of mankind. Nature 415 (6867), 23.

Cuartas, L. A., Tomasella, J., Nobre, A. D., Hodnett, M. G., Waterloo, M. J., Múnera, J. C., 2007. Interception water-partitioning dynamics for a pristine rainforest in Central Amazonia: Marked differences between normal and dry years. Agricultural and Forest Meteorology 145 (1-2), 69–83.

Cui, Y. P., Liu, J. Y., Hu, Y. F., Bing, L. F., Tao, F. L., Wang, J. B., 2012. Estimating and Analyzing the Optimum Temperature for Vegetation Growth in China (In Chinese). Journal of Natural Resources 27 (2), 281–292.

Czikowsky, M. J., Fitzjarrald, D. R., 2009. Detecting rainfall interception in an Amazonian rain forest with eddy flux measurements. Journal of Hydrology 377 (1-2), 92–105.

Dai, A., Qian, T., Trenberth, K. E., Milliman, J. D., may 2009. Changes in continental freshwater discharge from 1948 to 2004. Journal of Climate 22 (10), 2773–2792.

Dai, A., Trenberth, K. E., 2002. Estimates of freshwater discharge from continents: Latitudinal and seasonal variations. Journal of hydrometeorology 3, 660–687.

D'Almeida, C., Vorosmarty, C. J., Hurtt, G. C., Marengo, J. A., Dingman, S. L., Keim, B. D., 2007. The effects of deforestation on the hydrological cycle in Amazonia: a review on scale and resolution. International Journal of Climatology 27 (5), 633–647.

de Boer-Euser, T., Mcmillan, H. H. K., Hrachowitz, M., Winsemius, H. H. C., Savenije,

H. H. H. G., 2016. Influence of soil and climate on root zone storage capacity. Water Resources Research 52 (3), 2009–2024.

de Bruin, H. A. R., Jacobs, C. M., 1989. Forests and regional-scale processes. Biological Sciences 324 (1223), 393–406.

De Groen, M. M., Savenije, H. H. G., 2006. A monthly interception equation based on the statistical characteristics of daily rainfall. Water Resources Research 42 (12), W12417.

de Jong, S. M., Jetten, V. G., 2007. Estimating spatial patterns of rainfall interception from remotely sensed vegetation indices and spectral mixture analysis. International Journal of Geographical Information Science 21 (5), 529–545.

de Vrese, P., Hagemann, S., Claussen, M., 2016. Asian Irrigation, African Rain: Remote Impacts of Irrigation. Geophysical Research Letters 43 (8), 3737–3745.

Dee, D., Uppala, S., Simmons, A. J., Berrisford, P., Poli, P., Kobayashi, S., Andrae, U., Balmaseda, M., Balsamo, G., Bauer, P., Bechtold, P., Beljaars, A. C. M., van de Berg, L., Bidlot, J., Bormann, N., Delsol, C., Dragani, R., Fuentes, M., Geer, A., Haimberger, L., Healy, S., Hersbach, H., Hólm, E., Isaksen, L., Kållberg, P., Köhler, M., Matricardi, M., McNally, A., Monge-Sanz, B., Morcrette, J.-J., Park, B.-K., Peubey, C., de Rosnay, P., Tavolato, C., Thépaut, J.-N., Vitart, F., 2011. The ERA-Interim reanalysis: configuration and performance of the data assimilation system. Quarterly Journal of the Royal Meteorological Society 137, 553–597.

Delworth, T., Manabe, S., 1988. The influence of potential evaporation on the variabilities of simulated soil wetness and climate. Journal of Climate 1, 523–547.

Dirmeyer, P. A., Gao, X., Zhao, M., Guo, Z., Oki, T., Hanasaki, N., 2006. GSWP-2: Multimodel Analysis and Implications for Our Perception of the Land Surface. Bulletin of the American Meteorological Society 87 (10), 1381–1397.

Döll, P., Kaspar, F., Lehner, B., 2003. A global hydrological model for deriving water availability indicators: model tuning and validation. Journal of Hydrology 270 (1-2), 105–134.

Döll, P., Lehner, B., 2002. Validation of a new global 30-min drainage direction map. Journal of Hydrology 258 (1), 214–231.

Döll, P., Siebert, S., 2002. Global modeling of irrigation water requirements. Water Resources Research 38 (4), 8–1–8–10.

Doorenbos, J., Pruitt, W. O., 1977. Guidelines for predicting crop water requirement. In: FAO Irrigation and Drainage Paper (FAO), no. 24. Food and Agriculture Organization of the United Nations, Rome, p. 144.

Dore, M. H. I., 2005. Climate change and changes in global precipitation patterns: what do we know? Environment international 31 (8), 1167–81.

Dunne, K. A., Willmott, C. J., 1996. Global distribution of plant-extractable water capacity of soil. International Journal of Climatology 16 (8), 841–859.

FAO/IIASA/ISRIC/ISSCAS/JRC, 2012. Harmonized World Soil Database (version 1.2).

Farah, H., Bastiaanssen, W., Feddes, R., 2004. Evaluation of the temporal variability of the evaporative fraction in a tropical watershed. International Journal of Applied Earth Observation and Geoinformation 5 (2), 129–140.

Feddes, R., Menenti, M., Kabat, P., Bastiaanssen, W., 1993. Is large-scale inverse modelling of unsaturated flow with areal average evaporation and surface soil moisture as

estimated from remote sensing feasible? Journal of Hydrology 143 (1-2), 125–152.

Feddes, R. A., Hoff, H., Bruen, M., Dawson, T., de Rosnay, P., Dirmeyer, P. A., Jackson, R. B., Kabat, P., Kleidon, A., Lilly, A., Pitman, A. J., 2001. Modeling root water uptake in hydrological and climate models. Bulletin of the American Meteorological Society 82 (12), 2797–2809.

Federer, C., Vörösmarty, C., Fekete, B., 1996. Intercomparison of methods for calculating potential evaporation in regional and global water balance models. Water Resources Research 32 (7), 2315–2321.

Fekete, B., Vörösmarty, C., Roads, J., Willmott, C., 2004. Uncertainties in precipitation and their impacts on runoff estimates. Journal of Climate 17, 294–304.

Fekete, B. M., Vörösmarty, C. J., Grabs, W., 2000. Global Composite Runoff Fields Based on Observed River Discharge and Simulated Water Balances. Tech. rep., Global Runoff Data Centre, Federal Insititute of Hydrology, Koblenz.

Feldman, L. J., 1984. Regulation of root development. Annual review of plant physiology 35, 223–42.

Fenicia, F., McDonnell, J. J., Savenije, H. H. G., 2008. Learning from model improvement: On the contribution of complementary data to process understanding. Water Resources Research 44 (6), W06419.

Findell, K. L., Shevliakova, E., Milly, P. C. D., Stouffer, R. J., Findell, K. L., Shevliakova, E., Milly, P. C. D., Stouffer, R. J., 2007. Modeled Impact of Anthropogenic Land Cover Change on Climate. Journal of Climate 20 (14), 3621–3634.

Foley, J. A., 2005. Global Consequences of Land Use. Science 309 (5734), 570–574.

Franken, W., Leopoldo, P. R., Matsui, E., Ribeiro, M. D. N. G., 1992. Estudo da interceptação da água de chuva na coberta florestal Amazônica do tipo terra firme. Acta Amazonica 12 (2), 327–331.

Friedl, M. a., Sulla-Menashe, D., Tan, B., Schneider, A., Ramankutty, N., Sibley, A., Huang, X., 2010. MODIS Collection 5 global land cover: Algorithm refinements and characterization of new datasets. Remote Sensing of Environment 114 (1), 168–182.

Funk, C. C., Peterson, P. J., Landsfeld, M. F., Pedreros, D. H., Verdin, J. P., Rowland, J. D., Romero, B. E., Husak, G. J., Michaelsen, J. C., Verdin, A. P., 2014. A quasi-global precipitation time series for drought monitoring: U.S. Geological Survey data series 832. Tech. rep., U.S. Geological Survey.

Gao, H., Hrachowitz, M., Fenicia, F., Gharari, S., Savenije, H. H. G., 2013. Testing the realism of a topography driven model (FLEX-Topo) in the nested catchments of the Upper Heihe, China. Hydrology and Earth System Sciences Discussions 10 (10), 12663–12716.

Gao, H., Hrachowitz, M., Schymanski, S., Fenicia, F., Sriwongsitanon, N., Savenije, H., 2014. Climate controls how ecosystems size the root zone storage capacity at catchment scale. Geophysical Research Letters 41 (22), 7916–7923.

Gedney, N., Cox, P. M., Betts, R. A., Boucher, O., Huntingford, C., Stott, P. A., 2006. Detection of a direct carbon dioxide effect in continental river runoff records. Nature 439 (7078), 835–838.

Gedney, N., Huntingford, C., Weedon, G. P., Bellouin, N., Boucher, O., Cox, P. M., 2014. Detection of solar dimming and brightening effects on Northern Hemisphere river flow.

Nature Geosci 7 (11), 796–800.

Gentine, P., D'Odorico, P., Lintner, B. R., Sivandran, G., Salvucci, G., 2012. Interdependence of climate, soil, and vegetation as constrained by the Budyko curve. Geophysical Research Letters 39 (19), L19404.

Gerrits, a. M. J., Pfister, L., Savenije, H. H. G., 2010. Spatial and temporal variability of canopy and forest floor interception in a beech forest. Hydrological Processes 24 (21), 3011–3025.

Gerrits, a. M. J., Savenije, H. H. G., Veling, E. J. M., Pfister, L., 2009. Analytical derivation of the Budyko curve based on rainfall characteristics and a simple evaporation model. Water Resources Research 45 (4), 1–15.

Gerten, D., Hoff, H., Bondeau, A., Lucht, W., Smith, P., Zaehle, S., 2005. Contemporary "green" water flows: Simulations with a dynamic global vegetation and water balance model. Physics and Chemistry of the Earth, Parts A/B/C 30 (6-7), 334–338.

Gerten, D., Rost, S., von Bloh, W., Lucht, W., 2008. Causes of change in 20th century global river discharge. Geophysical Research Letters 35 (20), L20405.

Gharari, S., Hrachowitz, M., Fenicia, F., Gao, H., Savenije, H. H. G., 2014. Using expert knowledge to increase realism in environmental system models can dramatically reduce the need for calibration. Hydrology and Earth System Sciences 18 (12), 4839–4859.

Givnish, T. e., 1986. On the Economy of Plant Form and Function. Cambridge University Press.

Glarner, H., 2006. Length of Day and Twilight.
URL http://herbert.gandraxa.com/length{_}of{_}day.xml

Goessling, H. F., Reick, C. H., 2011. What do moisture recycling estimates tell us? Exploring the extreme case of non-evaporating continents. Hydrology and Earth System Sciences 15 (10), 3217–3235.

Goldewijk, K. K., 2001. Estimating global land use change over the past 300 years: The HYDE database. Global Biogeochemical Cycles 15 (2), 417–433.

Gordon, L. J., Steffen, W., Jönsson, B. F., Folke, C., Falkenmark, M., Johannessen, A., Johannessen, Å., 2005. Human modification of global water vapor flows from the land surface. Proceedings of the National Academy of Sciences of the United States of America 102 (21), 7612–7617.

Greve, P., Orlowsky, B., Mueller, B., Sheffield, J., Reichstein, M., Seneviratne, S. I., 2014. Global assessment of trends in wetting and drying over land. Nature Geoscience 4, 716–721.

Guerschman, J. P., Van Dijk, A. I., Mattersdorf, G., Beringer, J., Hutley, L. B., Leuning, R., Pipunic, R. C., Sherman, B. S., 2009. Scaling of potential evapotranspiration with MODIS data reproduces flux observations and catchment water balance observations across Australia. Journal of Hydrology 369 (1-2), 107–119.

Guillod, B. P., Orlowsky, B., Miralles, D. G., Teuling, A. J., Seneviratne, S. I., 2015. Reconciling spatial and temporal soil moisture effects on afternoon rainfall. Nature communications 6, 6443.

Gumbel, E. J., 1935. Les valeurs extrêmes des distributions statistiques. Annales de l'institut Henri Poincaré 5 (2), 115–158.

Güntner, A., 2008. Improvement of global hydrological models using GRACE data. Surveys in Geophysics 29 (4-5), 375–397.

Haddeland, I., Clark, D. B., Franssen, W., Ludwig, F., Voß, F., Arnell, N. W., Bertrand, N., Best, M., Folwell, S., Gerten, D., Gomes, S., Gosling, S. N., Hagemann, S., Hanasaki, N., Harding, R., Heinke, J., Kabat, P., Koirala, S., Oki, T., Polcher, J., Stacke, T., Viterbo, P., Weedon, G. P., Yeh, P., 2011. Multimodel Estimate of the Global Terrestrial Water Balance: Setup and First Results. Journal of Hydrometeorology 12 (5), 869–884.

Hagemann, S., Kleidon, A., 1999. The influence of rooting depth on the simulated hydrological cycle of a GCM. Physics and Chemistry of the Earth, Part B: Hydrology, Oceans and Atmosphere 24 (7), 775–779.

Hallgren, W. S., Pitman, A. J., 2000. The uncertainty in simulations by a Global Biome Model (BIOME3) to alternative parameter values. Global Change Biology 6 (5), 483–495.

Harris, I., Jones, P., Osborn, T., Lister, D., 2014. Updated high-resolution grids of monthly climatic observations - the CRU TS3.10 dataset. International Journal of Climatology 34 (3), 623–642.

Herold, N., Alexander, L., Donat, M., Contractor, S., Becker, A., 2015. How much does it rain over land? Geophysical Research Letters 43 (1), 341–348.

Herwitz, S. R., 1985. Interception storage capacities of tropical rainforest canopy trees. Journal of Hydrology 77 (1-4), 237–252.

Hessels, T. M., 2015. Comparison and Validation of Several Open Access Remotely Sensed Rainfall Products for the Nile Basin. Ph.D. thesis, Delft University of Technology.

Hicke, J. A., Jenkins, J. C., Ojima, D. S., Ducey, M., 2007. Spatial patterns of forest characteristics in the Western United States derived from inventories. Ecological Applications 17 (8), 2387–2402.

Hildebrandt, A., Eltahir, E. A. B., 2007. Ecohydrology of a seasonal cloud forest in Dhofar: 2. Role of clouds, soil type, and rooting depth in tree-grass competition. Water Resources Research 43 (11), W11411.

Hirota, M., Holmgren, M., Van Nes, E. H., Scheffer, M., 2011. Global resilience of tropical forest and savanna to critical transitions. Science 334 (6053), 232–235.

Hofste, R., 2014. Comparative analysis of near-operational evapotranspiration products for the Nile basin based on Earth Observations; First steps towards an ensemble ET product. Master thesis, Delft University of Technology.

Holling, C. S., 1973. Resilience and Stability of Ecological Systems. Annual Review of Ecology and Systematics 4, 1–23.

Hoogeveen, J., Faurès, J.-M., Peiser, L., Burke, J., van de Giesen, N., 2015. GlobWat – a global water balance model to assess water use in irrigated agriculture. Hydrology and Earth System Sciences 19 (9), 3829–3844.

Hu, G., Jia, L., 2015. Monitoring of evapotranspiration in a semi-arid inland river basin by combining microwave and optical remote sensing observations. Remote Sensing 7 (3), 3056–3087.

Hu, G., Jia, L., Menenti, M., 2015. Comparison of MOD16 and LSA-SAF MSG evapotranspiration products over Europe for 2011. Remote Sensing of Environment 156, 510–526.

Hunger, M., Döll, P., 2008. Value of river discharge data for global-scale hydrological

modeling. Hydrology and Earth System Sciences 12 (3), 841–861.

Hurtt, G. C., Chini, L. P., Frolking, S., Betts, R. A., Feddema, J., Fischer, G., Fisk, J. P., Hibbard, K., Houghton, R. A., Janetos, A., Jones, C. D., Kindermann, G., Kinoshita, T., Klein Goldewijk, K., Riahi, K., Shevliakova, E., Smith, S., Stehfest, E., Thomson, A., Thornton, P., van Vuuren, D. P., Wang, Y. P., 2011. Harmonization of land-use scenarios for the period 1500-2100: 600 years of global gridded annual land-use transitions, wood harvest, and resulting secondary lands. Climatic Change 109 (1), 117–161.

Ichii, K., Hashimoto, H., White, M. a., Potter, C., Hutyra, L. R., Huete, A. R., Myneni, R. B., Nemani, R. R., 2007. Constraining rooting depths in tropical rainforests using satellite data and ecosystem modeling for accurate simulation of gross primary production seasonality. Global Change Biology 13 (1), 67–77.

Ichii, K., Wang, W., Hashimoto, H., Yang, F., Votava, P., Michaelis, A. R., Nemani, R. R., 2009. Refinement of rooting depths using satellite-based evapotranspiration seasonality for ecosystem modeling in California. Agricultural and Forest ... 149 (11), 1907–1918.

Jackson, R. B., Canadell, J., Ehleringer, J. R., Mooney, H. A., Sala, O. E., Schulze, E. D., 1996. A global analysis of root distributions for terrestrial biomes. Oecologia 108 (3), 389–411.

Jägermeyr, J., Gerten, D., Heinke, J., Schaphoff, S., Kummu, M., Lucht, W., 2015. Water savings potentials of irrigation systems: global simulation of processes and linkages. Hydrology and Earth System Sciences 19 (7), 3073–3091.

Jaramillo, F., Destouni, G., 2015. Local flow regulation and irrigation raise global human water consumption and footprint. Science 350 (6265), 1248–1251.

Jarvis, P., 1976. The interpretation of the variations in leaf water potential and stomatal conductance found in canopies in the field. Philosophical Transactions of the Royal Society of London 273 (927), 593–610.

Jasechko, S., Sharp, Z. D., Gibson, J. J., Birks, S. J., Yi, Y., Fawcett, P. J., 2013. Terrestrial water fluxes dominated by transpiration. Nature 496 (7445), 347–50.

Jasechko, S., Sharp, Z. D., Gibson, J. J., Birks, S. J., Yi, Y., Fawcett, P. J., 2014. Jasechko et al. reply. Nature 506 (7487), E2–3.

Jennings, C. M. H., 1974. The hydrology of Botswana. Ph.D. thesis, University of Natal.

Jhorar, R., van Dam, J., Bastiaanssen, W., Feddes, R., 2004. Calibration of effective soil hydraulic parameters of heterogeneous soil profiles. Journal of Hydrology 285 (1-4), 233–247.

Jiménez, C., Prigent, C., Mueller, B., Seneviratne, S. I., McCabe, M. F., Wood, E. F., Rossow, W. B., Balsamo, G., Betts, A. K., Dirmeyer, P. A., Fisher, J. B., Jung, M., Kanamitsu, M., Reichle, R. H., Reichstein, M., Rodell, M., Sheffield, J., Tu, K., Wang, K., 2011. Global intercomparison of 12 land surface heat flux estimates. Journal of Geophysical Research 116 (D2), 1–27.

Johansson, E. L., Fader, M., Seaquist, J. W., Nicholas, K. A., 2016. Green and blue water demand from large-scale land acquisitions in Africa. Proceedings of the National Academy of Sciences, 201524741.

Jolly, W. M., Nemani, R., Running, S. W., 2005. A generalized, bioclimatic index to predict foliar phenology in response to climate. Global Change Biology 11 (4), 619–632.

Jung, M., Reichstein, M., Ciais, P., Seneviratne, S. I., Sheffield, J., Goulden, M. L., Bonan, G. B., Cescatti, A., Chen, J., de Jeu, R., Dolman, A. J., Eugster, W., Gerten, D., Gianelle,

D., Gobron, N., Heinke, J., Kimball, J., Law, B. E., Montagnani, L., Mu, Q., Mueller, B., Oleson, K., Papale, D., Richardson, A. D., Roupsard, O., Running, S., Tomelleri, E., Viovy, N., Weber, U., Williams, C., Wood, E., Zaehle, S., Zhang, K., 2010. Recent decline in the global land evapotranspiration trend due to limited moisture supply. Nature advance on (7318), 951–4.

Karimi, P., Bastiaanssen, W. G. M., Molden, D., 2013. Water Accounting Plus (WA+) - A water accounting procedure for complex river basins based on satellite measurements. Hydrology and Earth System Sciences 17 (7), 2459–2472.

Keenan, T. F., Hollinger, D. Y., Bohrer, G., Dragoni, D., Munger, J. W., Schmid, H. P., Richardson, A. D., 2013. Increase in forest water-use efficiency as atmospheric carbon dioxide concentrations rise. Nature 499 (7458), 0–4.

Keys, P. W., Barnes, E. A., van der Ent, R. J., Gordon, L. J., 2014. Variability of moisture recycling using a precipitationshed framework. Hydrology and Earth System Sciences 18 (10), 3937–3950.

Keys, P. W., van der Ent, R. J., Gordon, L. J., Hoff, H., Nikoli, R., Savenije, H. H. G., 2012. Analyzing precipitationsheds to understand the vulnerability of rainfall dependent regions. Biogeosciences 9 (2), 733–746.

Keys, P. W., Wang-Erlandsson, L., Gordon, L. J., 2016. Revealing Invisible Water: Moisture Recycling as an Ecosystem Service. PloS one 11 (3), e0151993.

Kleidon, A., 2004. Global datasets of rooting zone depth inferred from inverse methods. Journal of Climate 17 (13), 2714–2722.

Kleidon, A., Heimann, M., 1998a. A method of determining rooting depth from a terrestrial biosphere model and its impacts on the global water and carbon cycle. Global Change Biology 4 (3), 275–286.

Kleidon, A., Heimann, M., 1998b. Optimised rooting depth and its impacts on the simulated climate of an atmospheric general circulation model. Geophysical Research Letters 25 (3), 345–348.

Kleidon, A., Heimann, M., 2000. Assessing the role of deep rooted vegetation in the climate system with model simulations: mechanism, comparison to observations and implications for Amazonian deforestation. Climate Dynamics 16 (2-3), 183–199.

Koren, I., Altaratz, O., Remer, L. A., Feingold, G., Martins, J. V., Heiblum, R. H., 2012. Aerosol-induced intensification of rain from the tropics to the mid-latitudes. Nature Geoscience 5 (2), 118–122.

Koster, R., Milly, P., 1997. The interplay between transpiration and runoff formulations in land surface schemes used with atmospheric models. Journal of Climate 10, 1578–1591.

Koster, R. D., Dirmeyer, P. A., Guo, Z., Bonan, G. B., Chan, E., Cox, P., Gordon, C. T., Kanae, S., Kowalczyk, E., Lawrence, D. M., Liu, P., Lu, C.-H., Malyshev, S., McAvaney, B., Mitchell, K., Mocko, D., Oki, T., Oleson, K., Pitman, A. J., Sud, Y. C., Taylor, C. M., Verseghy, D., Vasic, R., Xue, Y., Yamada, T., 2004. Regions of strong coupling between soil moisture and precipitation. Science (New York, N.Y.) 305 (5687), 1138–40.

Koster, R. D., P. Mahanama, S. P., 2012. Land Surface Controls on Hydroclimatic Means and Variability. Journal of Hydrometeorology 13 (5), 1604–1620.

Koster, R. D., Suarez, M. J., 1996. The influence of land surface moisture retention on precipitation statistics. Journal of Climate 9 (10), 2551–2567.

Koster, R. D., Suarez, M. J., Higgins, R. W., Van den Dool, H. M., 2003. Observational evidence that soil moisture variations affect precipitation. Geophysical Research Letters 30 (5), 1–4.

Kottek, M., Grieser, J., Beck, C., Rudolf, B., Rubel, F., 2006. World Map of the Köppen-Geiger climate classification updated. Meteorologische Zeitschrift 15 (3), 259–263.

Labat, D., Goddéris, Y., Probst, J. L., Guyot, J. L., 2004. Evidence for global runoff increase related to climate warming. Advances in Water Resources 27 (6), 631–642.

Laio, F., D'Odorico, P., Ridolfi, L., 2006. An analytical model to relate the vertical root distribution to climate and soil properties. Geophysical Research Letters 33 (18), L18401.

Lambin, E. F., Meyfroidt, P., 2011. Global land use change, economic globalization, and the looming land scarcity. Proceedings of the National Academy of Sciences 108 (9), 3465–3472.

Lambin, E. F., Turner, B., Geist, H. J., Agbola, S. B., Angelsen, A., Bruce, J. W., Coomes, O. T., Dirzo, R., Fischer, G., Folke, C., George, P., Homewood, K., Imbernon, J., Leemans, R., Li, X., Moran, E. F., Mortimore, M., Ramakrishnan, P., Richards, J. F., Skånes, H., Steffen, W., Stone, G. D., Svedin, U., Veldkamp, T. A., Vogel, C., Xu, J., 2001. The causes of land-use and land-cover change: moving beyond the myths. Global Environmental Change 11 (4), 261–269.

Larson, D., 2001. The paradox of great longevity in a short-lived tree species. Experimental Gerontology 36 (4-6), 651–673.

Lawrence, D., Vandecar, K., 2014. Effects of tropical deforestation on climate and agriculture. Nature Climate Change 5 (1), 27–36.

Lawrence, D. M., Thornton, P. E., Oleson, K. W., Bonan, G. B., 2007. The Partitioning of Evapotranspiration into Transpiration, Soil Evaporation, and Canopy Evaporation in a GCM: Impacts on Land–Atmosphere Interaction. Journal of Hydrometeorology 8 (4), 862–880.

Lee, J.-E., Oliveira, R. S., Dawson, T. E., Fung, I., 2005. Root functioning modifies seasonal climate. Proceedings of the National Academy of Sciences of the United States of America 102 (49), 17576–81.

Legates, D. R., Lins, H. F., McCabe, G. J., 2005. Comments on "Evidence for global runoff increase related to climate warming" by Labat et al. Advances in Water Resources 28 (12), 1310–1315.

Lenton, T. M., Held, H., Kriegler, E., Hall, J. W., Lucht, W., Rahmstorf, S., Schellnhuber, H. J., 2008. Tipping elements in the Earth's climate system. Proceedings of the National Academy of Sciences 105 (6), 1786–1793.

Liu, Y., Hiyama, T., Yasunari, T., Tanaka, H., 2012. A nonparametric approach to estimating terrestrial evaporation: Validation in eddy covariance sites. Agricultural and Forest Meteorology 157 (null), 49–59.

Lo, M.-h., Famiglietti, J. S., 2013. Irrigation in California ' s Central Valley strengthens the southwestern U . S . water cycle. Geophysical Research Letters 40 (October 2012).

Loehle, C., 1988. Tree life history strategies: the role of defenses. Canadian Journal of Forest Research 18 (2), 209–222.

Lohmann, D., Wood, E. F., 2003. Timescales of land surface evapotranspiration response

in the PILPS phase 2(c). Global and Planetary Change 38 (1-2), 81–91.

Makarieva, A. M., Gorshkov, V. G., 2007. Biotic pump of atmospheric moisture as driver of the hydrological cycle on land. Hydrology and Earth System Sciences 11 (2), 1013–1033.

Makarieva, A. M., Gorshkov, V. G., Sheil, D., Nobre, A. D., Bunyard, P., Li, B.-L., 2014. Why Does Air Passage over Forest Yield More Rain? Examining the Coupling between Rainfall, Pressure, and Atmospheric Moisture Content. Journal of Hydrometeorology 15 (1), 411–426.

Materia, S., Dirmeyer, P. A., Guo, Z., Alessandri, A., Navarra, A., 2010. The Sensitivity of Simulated River Discharge to Land Surface Representation and Meteorological Forcings. Journal of Hydrometeorology 11 (2), 334–351.

Matsumoto, K., Ohta, T., Nakai, T., Kuwada, T., Daikoku, K., Iida, S., Yabuki, H., Kononov, A. V., van der Molen, M. K., Kodama, Y., Maximov, T. C., Dolman, A. J., Hattori, S., 2008. Responses of surface conductance to forest environments in the Far East. Agricultural and Forest Meteorology 148 (12), 1926–1940.

McDonald, J. E., 1962. The evaporation precipitation fallacy. Weather 17 (5), 168–177.

McNaughton, K., Jarvis, P., 1983. Predicting effects of vegetation changes on transpiration and evaporation. In: Kozlowski, T. (Ed.), Water deficits and plant growth, vol. 7 Edition. Academic Press, New York, pp. 1–47.

Meesters, A. G. C. A., Dolman, A. J., Bruijnzeel, L. A., 2009. Comment on "Biotic pump of atmospheric moisture as driver of the hydrological cycle on land" by A. M. Makarieva and V. G. Gorshkov, Hydrol. Earth Syst. Sci., 11, 1013–1033, 2007. Hydrology and Earth System Sciences Discussions 6 (1), 401–416.

Mekonnen, M. M., Hoekstra, A. Y., 2016. Four billion people facing severe water scarcity. Science Advances 2 (2), e1500323.

Meyfroidt, P., Lambin, E. F., Erb, K.-H., Hertel, T. W., 2013. Globalization of land use: distant drivers of land change and geographic displacement of land use. Current Opinion in Environmental Sustainability 5 (5), 438–444.

Meyfroidt, P., Rudel, T. K., Lambin, E. F., 2010. Forest transitions, trade, and the global displacement of land use. Proceedings of the National Academy of Sciences of the United States of America 107 (49), 20917–22.

Miguez-Macho, G., Fan, Y., 2012. The role of groundwater in the Amazon water cycle: 2. Influence on seasonal soil moisture and evapotranspiration. Journal of Geophysical Research 117 (D15), D15114.

Milliman, J., Farnsworth, K., Jones, P., Xu, K., Smith, L., 2008. Climatic and anthropogenic factors affecting river discharge to the global ocean, 1951–2000. Global and Planetary Change 62 (3), 187–194.

Milly, P. C. D., 1994. Climate, soil water storage, and the average annual water balance. Water Resources Research 30 (7), 2143–2156.

Milly, P. C. D., Dunne, K. A., 1994. Sensitivity of the global water cycle to the water-holding capacity of land. Journal of Climate 7 (4), 506–526.

Miralles, D. G., De Jeu, R. a. M., Gash, J. H., Holmes, T. R. H., Dolman, a. J., 2011. Magnitude and variability of land evaporation and its components at the global scale. Hydrology and Earth System Sciences 15 (3), 967–981.

Miralles, D. G., Gash, J. H., Holmes, T. R. H., de Jeu, R. a. M., Dolman, A., 2010. Global

canopy interception from satellite observations. Journal of Geophysical Research 115 (D16), 1–8.

Miralles, D. G., Nieto, R., McDowell, N. G., Dorigo, W. A., Verhoest, N. E., Liu, Y. Y., Teuling, A. J., Dolman, A. J., Good, S. P., Gimeno, L., 2016. Contribution of water-limited ecoregions to their own supply of rainfall. Environmental Research Letters 11 (12), 124007.

Miralles, D. G., van den Berg, M. J., Gash, J. H., Parinussa, R. M., de Jeu, R. A. M., Beck, H. E., Holmes, T. R. H., Jiménez, C., Verhoest, N. E. C., Dorigo, W. A., Teuling, A. J., Johannes Dolman, A., 2013. El Niño–La Niña cycle and recent trends in continental evaporation. Nature Climate Change 4 (2), 122–126.

Moazami, S., Golian, S., Kavianpour, M. R., Hong, Y., 2013. Comparison of PERSIANN and V7 TRMM Multi-satellite Precipitation Analysis (TMPA) products with rain gauge data over Iran. International Journal of Remote Sensing 34 (22), 8156–8171.

Monteith, J. L., 1965. Evaporation and environment. In: Symp Soc Exp Biol. Vol. 19. Cambridge University Press, Swansea, Ch. The State, pp. 205–234.

Mu, Q., Zhao, M., Running, S. W., 2011. Improvements to a MODIS global terrestrial evapotranspiration algorithm. Remote Sensing of Environment 115 (8), 1781–1800.

Mueller, B., Hirschi, M., Jimenez, C., Ciais, P., Dirmeyer, P. A., Dolman, A. J., Fisher, J. B., Jung, M., Ludwig, F., Maignan, F., Miralles, D. G., McCabe, M. F., Reichstein, M., Sheffield, J., Wang, K., Wood, E. F., Zhang, Y., Seneviratne, S. I., 2013. Benchmark products for land evapotranspiration: LandFlux-EVAL multi-data set synthesis. Hydrology and Earth System Sciences 17 (10), 3707–3720.

Müller Schmied, H., Eisner, S., Franz, D., Wattenbach, M., Portmann, F. T., Flörke, M., Döll, P., 2014. Sensitivity of simulated global-scale freshwater fluxes and storages to input data, hydrological model structure, human water use and calibration. Hydrology and Earth System Sciences 18 (9), 3511–3538.

Nepstad, D. C., de Carvalho, C. R., Davidson, E. A., Jipp, P. H., Lefebvre, P. A., Negreiros, G. H., da Silva, E. D., Stone, T. A., Trumbore, S. E., Vieira, S., 1994. The role of deep roots in the hydrological and carbon cycles of Amazonian forests and pastures. Nature 372 (6507), 666–669.

Newbold, T., Hudson, L. N., Hill, S. L., Contu, S., Lysenko, I., Senior, R. a., Börger, L., Bennett, D. J., Choimes, A., Collen, B., Day, J., De Palma, A., Dıáz, S., Echeverria-Londoño, S., Edgar, M. J., Feldman, A., Garon, M., Harrison, M. L. K., Alhusseini, T., Ingram, D. J., Itescu, Y., Kattge, J., Kemp, V., Kirkpatrick, L., Kleyer, M., Laginha Pinto Correia, D., Martin, C. D., Meiri, S., Novosolov, M., Pan, Y., Phillips, H. R. P., Purves, D. W., Robinson, A., Simpson, J., Tuck, S. L., Weiher, E., White, H. J., Ewers, R. M., Mace, G. M., Scharlemann, J. P., Purvis, A., 2015. Global effects of land use on local terrestrial biodiversity. Nature 520 (7545), 45–.

Nijssen, B., O'Donnell, G. M., Lettenmaier, D. P., Lohmann, D., Wood, E. F., 2001. Predicting the discharge of global rivers. Journal of Climate 14 (15), 3307–3323.

Oki, T., Kanae, S., 2006. Global hydrological cycles and world water resources. Science 313 (5790), 1068–1072.

Orth, R., Staudinger, M., Seneviratne, S. I., Seibert, J., Zappa, M., 2015. Does model performance improve with complexity? A case study with three hydrological models.

Journal of Hydrology 523, 147–159.

Ostberg, S., Schaphoff, S., Lucht, W., Gerten, D., 2015. Three centuries of dual pressure from land use and climate change on the biosphere. Environmental Research Letters 10 (4), 044011.

Pellarin, T., Louvet, S., Gruhier, C., Quantin, G., Legout, C., 2013. A simple and effective method for correcting soil moisture and precipitation estimates using AMSR-E measurements. Remote Sensing of Environment 136 (null), 28–36.

Phillips, W. S., 1963. Depth of roots in Soil. Ecology 44 (2), 424.

Piao, S., Friedlingstein, P., Ciais, P., de Noblet-Ducoudré, N., Labat, D., Zaehle, S., 2007. Changes in climate and land use have a larger direct impact than rising CO2 on global river runoff trends. Proceedings of the National Academy of Sciences of the United States of America 104 (39), 15242–15247.

Pimm, S. L., Jenkins, C. N., Abell, R., Brooks, T. M., Gittleman, J. L., Joppa, L. N., Raven, P. H., Roberts, C. M., Sexton, J. O., 2014. The biodiversity of species and their rates of extinction, distribution, and protection. Science (New York, N.Y.) 344 (6187), 1246752.

Pitman, a. J., de Noblet-Ducoudré, N., Avila, F. B., Alexander, L. V., Boisier, J.-P., Brovkin, V., Delire, C., Cruz, F., Donat, M. G., Gayler, V., van den Hurk, B., Reick, C., Voldoire, A., 2012. Effects of land cover change on temperature and rainfall extremes in multi-model ensemble simulations. Earth System Dynamics 3 (2), 213–231.

Portmann, F. T., Siebert, S., Döll, P., 2010. MIRCA2000—Global monthly irrigated and rainfed crop areas around the year 2000: A new high-resolution data set for agricultural and hydrological modeling. Global Biogeochemical Cycles 24 (1), 1–24.

Poulter, B., 2012. Forest age datasets. In: American Geophysical Union, Fall Meeting. p. 12.

Putuhena, W., Cordery, I., 1996. Estimation of interception capacity of the forest floor. Journal of Hydrology 180 (June 1995), 283–299.

Ramankutty, N., Evan, A. T., Monfreda, C., Foley, J. A., 2008. Farming the planet: 1. Geographic distribution of global agricultural lands in the year 2000. Global Biogeochemical Cycles 22 (1), 1–19.

Ramankutty, N., Foley, J. A., 1999. Estimating historical changes in global land cover: Croplands historical have converted areas. Global Biogeochemical Cycles 13 (4), 997–1027.

Rockström, J., Falkenmark, M., Folke, C., Lannerstad, M., Barro, J., Enfors, E., Gordon, L., Heinke, J., Hoff, H., Pahl-Wostl, C., 2014. Water resilience for human prosperity. Cambridge University Press, New York.

Rockström, J., Falkenmark, M., Karlberg, L., Hoff, H., Rost, S., Gerten, D., 2009a. Future water availability for global food production: The potential of green water for increasing resilience to global change. Water Resources Research 45 (7), W00A12.

Rockström, J., Gordon, L. J., Folke, C., Falkenmark, M., Engwall, M., 1999. Linkages among water vapor flows, food production, and terrestrial ecosystem services. Conservation Ecology 3 (2), 5.

Rockström, J., Steffen, W., Noone, K., Persson, A., Chapin Iii, F. S., Lambin, E. F., Lenton, T. M., Scheffer, M., Folke, C., Schellnhuber, H. J., Nykvist, B., de Wit, C. A., Hughes, T., van der Leeuw, S., Rodhe, H., Sörlin, S., Snyder, P. K., Costanza, R., Svedin, U., Falkenmark, M., Karlberg, L., Corell, R. W., Fabry, V. J., Hansen, J., Walker, B., Liverman,

D., Richardson, K., Crutzen, P., Foley, J. A., 2009b. Planetary boundaries: Exploring the safe operating space for humanity. Ecology and Society 14 (2).

Rohwer, J., Gerten, D., Lucht, W., 2007. Development of functional irrigation types for improved global crop modelling. Tech. Rep. 104, Potsdam Institute for Climate Impact Research, Potsdam.

Rost, S., Gerten, D., Heyder, U., 2008. Human alterations of the terrestrial water cycle through land management. Advances in Geosciences 18 (18), 43–50.

Savenije, H. H. G., 2004. The importance of interception and why we should delete the term evapotranspiration from our vocabulary. Hydrological Processes 18 (8), 1507–1511.

Saxton, K. E., Rawls, W. J., 2006. Soil water characteristic estimates by texture and organic matter for hydrologic solutions. Soil Science Society of America Journal 70 (5), 1569.

Scheffer, M., Carpenter, S., Foley, J. A., Folke, C., Walker, B., 2001. Catastrophic shifts in ecosystems. Nature 413 (6856), 591–6.

Schenk, H., Jackson, R., 2002. The global biogeography of roots. Ecological monographs 72 (3), 311–328.

Schenk, H. J., 2008. The shallowest possible water extraction profile: a null model for global root distributions. Vadose Zone Journal 7 (3), 1119.

Schenk, H. J., Jackson, R. B., 2009. ISLSCP II Ecosystem rooting depths. In: G., F., Collatz, G., Meeson, B., Los, S., de Colstoun, E. B., Landis, D. (Eds.), ISLSCP Initiative II Collection. Oak Ridge National Laboratory Distributed Active Archive Center, Oak Ridge, Tennessee, U.S.A.

Schlaepfer, D. R., Ewers, B. E., Shuman, B. N., Williams, D. G., Frank, J. M., Massman, W. J., Lauenroth, W. K., 2014. Terrestrial water fluxes dominated by transpiration: Comment. Ecosphere 5 (5), art61.

Schlesinger, W. H., Jasechko, S., 2014. Transpiration in the global water cycle. Agricultural and Forest Meteorology 189-190, 115–117.

Schneider, U., Becker, A., Finger, P., Meyer-Christoffer, Anja Rudolf, B., Ziese, M., 2011. GPCC full data reanalysis version 6.0 at 0.5: Monthly land-surface precipitation from rain-gauges built on GTS-based and historic data.

Schwinning, S., Ehleringer, J. R., 2001. Water use trade-offs and optimal adaptations to pulse-driven arid ecosystems. Journal of Ecology 89 (3), 464–480.

Schymanski, S. J., Or, D., 2017. Leaf-scale experiments reveal an important omission in the Penman–Monteith equation. Hydrology and Earth System Sciences 21 (2), 685–706.

Scott, R., Entekhabi, D., Koster, R., Suarez, M., 1997. Timescales of land surface evapotranspiration response. Journal of climate 10, 559–566.

Scott, R., Koster, R. D., Entekhabi, D., Suarez, M. J., 1995. Effect of a canopy interception reservoir on hydrological persistence in a general circulation model. Journal of Climate 8 (7), 1917–1922.

Scurlock, J. M. O., Asner, G. P., Gower, S. T., 2001. Worldwide Historical Estimates and Bibliography of Leaf Area Index , 1932-2000. Tech. rep., Oak Ridge National Laboratory, Oak Ridge, Tennessee.

Seckler, D., Amarasinghe, U., Molden, D., de Silva, R., Barker, R., 1998. World Water Demand and Supply, 1990 to 2025: Scenarios and Issues. Tech. rep., International Water

Management Institute (IWMI), Colombo, Sri Lanka.

Senay, G. B., Bohms, S., Singh, R. K., Gowda, P. H., Velpuri, N. M., Alemu, H., Verdin, J. P., 2013. Operational evapotranspiration mapping using remote sensing and weather datasets: A new parameterization for the SSEB approach. JAWRA Journal of the American Water Resources Association 49 (3), 577–591.

Serafini, V. V., Sud, Y. C., 1987. The time scale of the soil hydrology using a simple water budget model. Journal of Climatology 7 (6), 585–591.

Shepherd, T. G., 2014. Atmospheric circulation as a source of uncertainty in climate change projections. Nature Geoscience 7 (10), 703–708.

Shukla, J., Mintz, Y., 1982. Iinfluence of land-surface evapotranspiration on the Earth's climate. Science 215 (4539), 1498–1501.

Shuttleworth, W. J., 2012. Terrestrial Hydrometeorology, 1st Edition. Wiley-Blackwell, West Sussex.

Sivandran, G., Bras, R. L., 2013. Dynamic root distributions in ecohydrological modeling: A case study at Walnut Gulch Experimental Watershed. Water Resources Research 49 (6), 3292–3305.

Smithwick, E. A., Lucash, M. S., McCormack, M. L., Sivandran, G., 2014. Improving the representation of roots in terrestrial models. Ecological Modelling 291, 193–204.

Spracklen, D., Arnold, S. R., Taylor, C. M., 2012. Observations of increased tropical rainfall preceded by air passage over forests. Nature 489 (7415), 282–285.

Spracklen, D. V., Garcia-Carreras, L., 2015. The impact of Amazonian deforestation on Amazon basin rainfall. Geophysical Research Letters 42, 9546–9552.

Staver, A. C., Archibald, S., Levin, S. A., 2011. The Global Extent and Determinants of Savanna and Forest as Alternative Biome States. Science 334 (6053), 230–232.

Steffen, W., Richardson, K., Rockstrom, J., Cornell, S. E., Fetzer, I., Bennett, E. M., Biggs, R., Carpenter, S. R., de Vries, W., de Wit, C. A., Folke, C., Gerten, D., Heinke, J., Mace, G. M., Persson, L. M., Ramanathan, V., Reyers, B., Sorlin, S., 2015. Planetary boundaries: Guiding human development on a changing planet. Science 347, 1259855.

Sterling, S. M., Ducharne, A., Polcher, J., 2012. The impact of global land-cover change on the terrestrial water cycle. Nature Climate Change 3 (4), 385–390.

Stewart, J., 1988. Modelling surface conductance of pine forest. Agricultural and Forest Meteorology 43 (1), 19–35.

Stickler, C. M., Coe, M. T., Costa, M. H., Nepstad, D. C., McGrath, D. G., Dias, L. C. P., Rodrigues, H. O., Soares-Filho, B. S., 2013. Dependence of hydropower energy generation on forests in the Amazon Basin at local and regional scales. Proceedings of the National Academy of Sciences of the United States of America 110 (23), 9601–6.

Stone, E., Kalisz, P., 1991. On the maximum extent of tree roots. Forest Ecology and Management 46 (1-2), 59–102.

Sutanto, S. J., van den Hurk, B., Hoffmann, G., Wenninger, J., Dirmeyer, P. a., Seneviratne, S. I., Röckmann, T., Trenberth, K. E., Blyth, E. M., 2014. HESS Opinions: A perspective on different approaches to determine the contribution of transpiration to the surface moisture fluxes. Hydrology and Earth System Sciences Discussions 11 (3), 2583–2612.

Swann, A. L., Longo, M., Knox, R. G., Lee, E., Moorcroft, P. R., 2015. Future deforestation in the Amazon and consequences for South American climate. Agricultural and Forest

Meteorology 214-215, 12–24.

Syed, T. H., Famiglietti, J. S., Chambers, D. P., Willis, J. K., Hilburn, K., 2010. Satellite-based global-ocean mass balance estimates of interannual variability and emerging trends in continental freshwater discharge. Proceedings of the National Academy of Sciences of the United States of America 107 (42), 17916–21.

Taylor, C. M., de Jeu, R. a. M., Guichard, F., Harris, P. P., Dorigo, W. a., 2012. Afternoon rain more likely over drier soils. Nature 489 (7416), 423–6.

Teuling, A. J., Seneviratne, S. I., Stöckli, R., Reichstein, M., Moors, E., Ciais, P., Luyssaert, S., van den Hurk, B. J. J. M., Ammann, C., Bernhofer, C., Dellwik, E., Gianelle, D., Gielen, B., Grünwald, T., Klumpp, K., Montagnani, L., Moureaux, C., Sottocornola, M., Wohlfahrt, G., 2010. Contrasting response of European forest and grassland energy exchange to heatwaves. Nature Geoscience 3 (10), 722–727.

Teuling, A. J., Seneviratne, S. I., Williams, C., Troch, P. A., 2006. Observed timescales of evapotranspiration response to soil moisture. Geophysical Research Letters 33 (23), L23403.

Tobón Marin, C., Bouten, W., Sevink, J., 2000. Gross rainfall and its partitioning into throughfall, stemflow and evaporation of intercepted water in four forest ecosystems in western Amazonia. Journal of Hydrology 237 (1-2), 40–57.

Tourula, T., Heikinheimo, M., jun 1998. Modelling evapotranspiration from a barley field over the growing season. Agricultural and Forest Meteorology 91 (3-4), 237–250.

Trambauer, P., Dutra, E., Maskey, S., Werner, M., Pappenberger, F., van Beek, L. P. H., Uhlenbrook, S., 2014. Comparison of different evaporation estimates over the African continent. Hydrology and Earth System Sciences 18 (1), 193–212.

Trenberth, K. E., 1998. Atmospheric moisture residence times and cycling: Implications for rainfall rates and climate change. Climatic Change 39 (4), 667–694.

Trenberth, K. E., Dai, A., van der Schrier, G., Jones, P. D., Barichivich, J., Briffa, K. R., Sheffield, J., 2013. Global warming and changes in drought. Nature Climate Change 4 (1), 17–22.

Trenberth, K. E., Fasullo, J., Mackaro, J., 2011. Atmospheric moisture transports from ocean to land and global energy flows in reanalyses. Journal of Climate 24 (18), 4907–4924.

Trenberth, K. E., Smith, L., Qian, T., Dai, A., Fasullo, J. T., 2007. Estimates of the Global Water Budget and Its Annual Cycle Using Observational and Model Data. Journal of Hydrometeorology 8 (4), 758–769.

Tuinenburg, O. A., 2013. Atmospheric Effects of Irrigation in Moonsoon Climate: The Indian Subcontinent. Ph.D. thesis, Wageningen University.

Tuinenburg, O. A., Hutjes, R. W. A., Kabat, P., 2012. The fate of evaporated water from the Ganges basin. J. Geophys. Res. 117 (D1), D01107.
URL http://dx.doi.org/10.1029/2011JD016221

Twine, T. E., Kustas, W. P., Norman, J. M., Cook, D. R., Houser, P. R., Meyers, T. P., Prueger, J. H., Starks, P. J., Wesley, M. L., 2000. Correcting eddy-covariance flux underestimates over a grassland. Agricultural and Forest Meteorology 103, 279–300.

van den Hoof, C., Vidale, P. L., Verhoef, A., Vincke, C., 2013. Improved evaporative flux partitioning and carbon flux in the land surface model JULES: Impact on the simulation

of land surface processes in temperate Europe. Agricultural and Forest Meteorology 181, 108–124.

van den Hurk, B. J. J. M., 2003. Impact of leaf area index seasonality on the annual land surface evaporation in a global circulation model. Journal of Geophysical Research 108 (D6), 4191.

van den Hurk, B. J. J. M., Viterbo, P., Beljaars, A. C. M., Betts, A. K., 2000. Offline validation of the ERA40 surface scheme. Tech. rep., European Centre for Medium-Range Weather Forecasts (ECMWF).
URL http://www.knmi.nl/publications/fulltexts/tm295.pdf

van der Ent, R. J., Savenije, H. H. G., 2011. Length and time scales of atmospheric moisture recycling. Atmospheric Chemistry and Physics 11 (5), 1853–1863.

van der Ent, R. J., Savenije, H. H. G., 2013. Oceanic sources of continental precipitation and the correlation with sea surface temperature. Water Resources Research 49 (7), n/a–n/a.

van der Ent, R. J., Savenije, H. H. G., Schaefli, B., Steele-Dunne, S. C., 2010. Origin and fate of atmospheric moisture over continents. Water Resources Research 46 (9), 1–12.

van der Ent, R. J., Wang-Erlandsson, L., Keys, P. W., Savenije, H. H. G., 2014. Contrasting roles of interception and transpiration in the hydrological cycle – Part 2: Moisture recycling. Earth System Dynamics 5 (2), 471–489.

van Dijk, A., Warren, G., Van Niel, T., Byrne, G., Pollock, D., Doody, T., 2014. Derivation of data layers from medium resolution remote sensing to support mapping of groundwater dependent ecosystems. Tech. rep., A report for the National Water Commission.

van Genuchten, M. T., 1980. A Closed-form Equation for Predicting the Hydraulic Conductivity of Unsaturated Soils. Soil Science Society of America Journal 44, 892–898.

van Nes, E. H., Hirota, M., Holmgren, M., Scheffer, M., 2014. Tipping points in tropical tree cover: linking theory to data. Global change biology 20 (3), 1016–21.

van Noordwijk, M., Namirembe, S., Catacutan, D., Williamson, D., Gebrekirstos, A., 2014. Pricing rainbow, green, blue and grey water: tree cover and geopolitics of climatic teleconnections. Current Opinion in Environmental Sustainability 6, 41–47.

van Wijk, M. T., Bouten, W., 2001. Towards understanding tree root profiles: simulating hydrologically optimal strategies for root distribution. Hydrology and Earth System Sciences 5 (4), 629–644.

Vinukollu, R. K., Meynadier, R., Sheffield, J., Wood, E. F., 2011. Multi-model, multi-sensor estimates of global evapotranspiration: climatology, uncertainties and trends. Hydrological Processes 25 (26), 3993–4010.

Wada, Y., Bierkens, M. F. P., 2014. Sustainability of global water use: past reconstruction and future projections. Environmental Research Letters 9 (10), 104003.

Wang, A., Zeng, X., Shen, S. S., Zeng, Q.-C., Dickinson, R. E., 2006. Time Scales of Land Surface Hydrology. Journal of Hydrometeorology 7, 868–879.

Wang, D., Wang, G., Anagnostou, E. N., 2007. Evaluation of canopy interception schemes in land surface models. Journal of Hydrology 347 (3-4), 308–318.

Wang, K., Dickinson, R. E., 2012. A Review of Global Terrestrial Evapotranspiration:

Observation, Modeling, Climatology, and Climatic Variability. Review of Geophysics 50.

Wang, P., Song, X., Han, D., Zhang, Y., Zhang, B., 2012. Determination of evaporation, transpiration and deep percolation of summer corn and winter wheat after irrigation. Agricultural Water Management 105, 32–37.

Wang-Erlandsson, L., Bastiaanssen, W. G. M., Gao, H., Jägermeyr, J., Senay, G. B., van Dijk, A. I. J. M., Guerschman, J. P., Keys, P. W., Gordon, L. J., Savenije, H. H. G., 2016. Global root zone storage capacity from satellite-based evaporation. Hydrology and Earth System Sciences 20 (4), 1459–1481.

Wang-Erlandsson, L., Fetzer, I., Keys, P. W., van der Ent, R. J., Savenije, H. H. G., Gordon, L. J., 2017. Remote land use impacts on river flows through atmospheric teleconnections. Hydrology and Earth System Sciences Discussions, 1–17.

Wang-Erlandsson, L., van der Ent, R. J., Gordon, L. J., Savenije, H. H. G., 2014. Contrasting roles of interception and transpiration in the hydrological cycle – Part 1: Temporal characteristics over land. Earth System Dynamics 5 (2), 441–469.

Wei, J., Dirmeyer, P. A., Wisser, D., Bosilovich, M. G., Mocko, D. M., oct 2012. Where Does the Irrigation Water Go? An Estimate of the Contribution of Irrigation to Precipitation Using MERRA. Journal of Hydrometeorology 14 (1), 275–289.
URL http://journals.ametsoc.org/doi/abs/10.1175/JHM-D-12-079.1

Wei, Z., Yoshimura, K., Wang, L., Miralles, D. G., Jasechko, S., Lee, X., mar 2017. Revisiting the contribution of transpiration to global terrestrial evapotranspiration. Geophysical Research Letters 44 (6), 2792–2801.
URL http://doi.wiley.com/10.1002/2016GL072235

Widén-Nilsson, E., Halldin, S., Xu, C.-Y., 2007. Global water-balance modelling with WASMOD-M: Parameter estimation and regionalisation. Journal of Hydrology 340 (1-2), 105–118.

Wilhite, D. A., Glantz, M. H., 1985. Understanding: the Drought Phenomenon: The Role of Definitions. Water International 10 (3), 111–120.

Wilson, K., Goldstein, A., Falge, E., Aubinet, M., Baldocchi, D., Berbigier, P., Bernhofer, C., Ceulemans, R., Dolman, H., Field, C., Grelle, A., Ibrom, A., Law, B., Kowalski, A., Meyers, T., Moncrieff, J., Monson, R., Oechel, W., Tenhunen, J., Valentini, R., Verma, S., 2002. Energy balance closure at FLUXNET sites. Agricultural and Forest Meteorology 113 (1-4), 223–243.

Winsemius, H. C., Schaefli, B., Montanari, A., Savenije, H. H. G., 2009. On the calibration of hydrological models in ungauged basins: A framework for integrating hard and soft hydrological information. Water Resources Research 45 (12), W12422.

Xiao, J., Chen, J., Davis, K. J., Reichstein, M., 2012. Advances in upscaling of eddy covariance measurements of carbon and water fluxes. Journal of Geophysical Research 117, G00J01.

Yang, Y., Donohue, R. J., McVicar, T. R., 2016. Global estimation of effective plant rooting depth: Implications for hydrological modeling. Water Resources Research 52 (10), 8260–8276.

Yilmaz, M. T., Anderson, M. C., Zaitchik, B., Hain, C. R., Crow, W. T., Ozdogan, M., Chun, J. A., Evans, J., 2014. Comparison of prognostic and diagnostic surface flux modeling approaches over the Nile River basin. Water Resources Research 50 (1), 386–408.

Zemp, D. C., Schleussner, C.-F., Barbosa, H. M. J., Hirota, M., Montade, V., Sampaio, G., Staal, A., Wang-Erlandsson, L., Rammig, A., 2017. Self-amplified Amazon forest loss due to vegetation-atmosphere feedbacks. Nature Communications 8, 14681.

Zeng, X., 2001. Global vegetation root distribution for land modeling. Journal of Hydrometeorology 2 (5), 525–530.

Zeng, X., Dai, Y.-J., Dickinson, R. E., Shaikh, M., 1998. The role of root distribution for climate simulation over land. Geophysical Research Letters 25 (24), 4533–4536.

Zhou, M., Ishidaira, H., Hapuarachchi, H., Magome, J., Kiem, A., Takeuchi, K., 2006. Estimating potential evapotranspiration using Shuttleworth–Wallace model and NOAA-AVHRR NDVI data to feed a distributed hydrological model over the Mekong River basin. Journal of Hydrology 327 (1-2), 151–173.

Zon, R., 1927. Forests and water in the light of scientific investigation. Tech. rep., US Government Printing Office, Washington DC.

CURRICULUM VITAE

Lan WANG-ERLANDSSON

2 May 1985 Born in Guiyang, China.

EDUCATION

2012-2017 PhD in global hydrology
Delft University of Technology, Delft, the Netherlands
Thesis: Root for rain. Towards understanding land-use change impacts on the water cycle
Promotor: Prof. dr. ir. H. H. G. Savenije
Promotor: Prof. dr. J. Rockström
Copromotor: Dr. L. J. Gordon

2004-2009 MSc in civil engineering
KTH Royal Institute of Technology, Stockholm, Sweden
Track: Natural Resources
Thesis: Review of the Strategic Environmental Assessment of the Dali City Urban Master Plan revision 2007-2025
Exchange studies: École Nationale des Ponts et Chaussées, Paris, France
National University of Singapore, Singapore

EXPERIENCE

2010-2012 Environmental consultant
Golder Associates, Stockholm, Sweden

2009-2010 Intern and project research assistant
Stockholm Environment Institute (SEI), Stockholm, Sweden

AWARDS AND SCHOLARSHIPS

2017	Postdoctoral Fellowship for Overseas Researchers (standard) Japan Society for the Promotion of Science (JSPS)
2016	Best Oral Presentation award Global Land Programme 3rd Open Science Meeting
2009	Student scholarship based on academic performance KTH Royal Institute of Technology general student scholarships
2008	Minor Field Studies (MFS) stipend Swedish Council for Higher Education
2008	Student scholarship based on academic performance KTH Royal Institute of Technology general student scholarships
2007	Scholarship for sustainability studies abroad Erik och Göran Ennerfeldts stiftelse
2007	Student scholarship based on academic performance KTH Royal Institute of Technology general student scholarships
2007	Student scholarship based on academic performance Henrik Göransson's Sandviken Scholarship Foundation

LIST OF PUBLICATIONS

Wang-Erlandsson L., Fetzer, I., Keys P. W., van der Ent R. J., Savenije H. H. G., and Gordon L. J., *Remote land-use change effects on river flows through atmospheric teleconnections*, Hydrology and Earth System Science Discussions, in review.

Keys, P.W., **Wang-Erlandsson, L.**, and Gordon, L. J., *Megacity Precipitationsheds Reveal Reliance on Regional Evaporation for Water Supply*, PLoS ONE, in review.

Zemp. C., Schleussner, C-F., Barbosa, H. M. J., Hirota, M., Montade, V., Sampaio, G., Staal. A., **Wang-Erlandsson, L.**, and Rammig A., *Self-amplified Amazon forest loss due to vegetation-atmosphere feedbacks*, Nature Communications 8, 14681, 2017.

Keys, P.W., **Wang-Erlandsson, L.**, Galaz, V., Ebbesson, E., and Gordon, L. J., *Approaching Moisture Recycling Governance*, Global Environmental Change 45: 15-23, 2017.

Wang-Erlandsson L., Bastiaanssen, W. G. M., Gao, H., Jägermeyr, J., Senay, G. B., van Dijk, A. I. J. M., Guerschman, J. P., Keys, P. W., Gordon, L. J., and Savenije, H. H. G., *Global root zone storage capacity from satellite-based evaporation*, Hydrology and Earth System Science 20(4):1459–1481, 2016.

Keys P. W., **Wang-Erlandsson L.**, Gordon L. J., *Revealing Invisible Water: Moisture Recycling as an Ecosystem Service*, PLoS ONE 11(3):e0151993, 2016.

Coenders-Gerrits, A. M. J., Van der Ent, R. J., Bogaard, T. A., **Wang-Erlandsson, L.**, Hrachowitz, M., and Savenije, H. H. G., *Uncertainties in transpiration estimates*, Nature, 506, E1-E2, 2014.

Van Der Ent R. J., **Wang-Erlandsson L.**, Keys P. W., and Savenije H. H. G., *Contrasting roles of interception and transpiration in the hydrological cycle – Part 2: Moisture recycling*, Earth System Dynamics 5(2):471–489, 2014.

Wang-Erlandsson L., van der Ent R. J., Gordon L. J. and Savenije H. H. G., *Contrasting roles of interception and transpiration in the hydrological cycle – Part 1: Temporal characteristics over land*, Earth System Dynamics 5(2):441–469, 2014.